DISSERTATION

Titel der Dissertation
"Next Generation High–k Dielectrics for DRAM Produced by Atomic Layer Deposition Studied by Transmission Electron Microscopy"

Verfasser
Mag. Peter Schindler

angestrebter akademischer Grad
Doktor der Naturwissenschaften (Dr. rer. nat.)
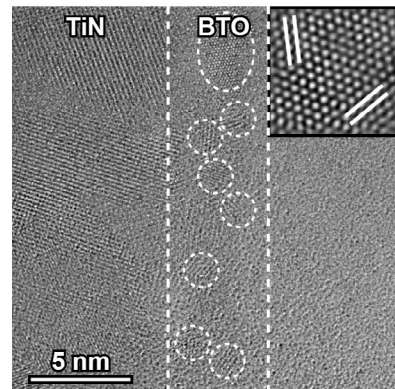
Wien, 2015

DISSERTATION

Next Generation High-*k* Dielectrics for DRAM Produced by Atomic Layer Deposition Studied by Transmission Electron Microscopy

Peter Schindler
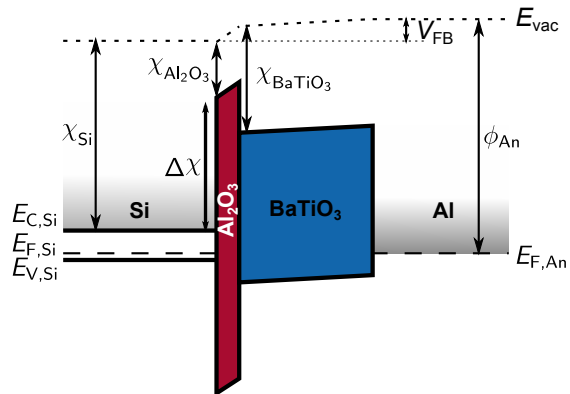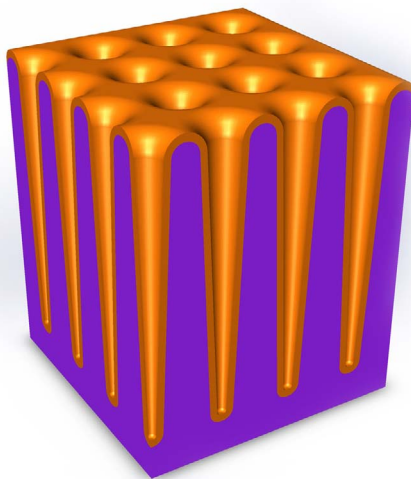
$$J_{\mathrm{FN}}(V_{\mathrm{app}}) = \frac{4\pi \cdot m_{\mathrm{eff,Si}} \cdot e}{h^3} \int_{E_{\mathrm{C,Si}}}^{E_{\mathrm{C,Diel}}(0)} TC(E, V_{\mathrm{app}}) \cdot N(E, V_{\mathrm{app}})\, \mathrm{d}E$$

Supervisors

Prof. F. B. Prinz **Prof. H. P. Karnthaler**

Stanford University

2015

universität wien

Typesetting for this dissertation was done with $\text{\LaTeX\,} 2_\varepsilon$ via MiKTeX and TeXnicCenter
Literature was organized with Mendeley and implemented by $\textsc{Bib}\text{\TeX}$
Vector graphics were created with Inkscape v0.48
Origin Pro 8 and Matlab R2015a were used for data plots

Gewidmet meinen Eltern Fredi und Sonja und meiner Großmutter Edith

" The most beautiful thing we can experience is the mysterious.
It is the source of all true art and science. "
Albert Einstein

Abstract

Key pieces of modern day technology such as the metal–oxide–semiconductor field-effect transistor and the dynamic random-access memory (DRAM) keep following the trend of down-scaling. This requires the dielectric layer that is a crucial component in these structures to reduce its thickness. As down-scaling continues rapidly, device features approach the fundamental physical limits: For the most commonly used gate dielectric SiO_2 direct tunneling starts to occur at a thickness below 3 nm. There are two main strategies to increase the capacitance without further decreasing the thickness of the dielectric layer. One is to facilitate high aspect-ratio (AR) surfaces to increase the effective surface area. The other one is to use high–k materials instead of SiO_2.

The key enabling technique to deposit ultra-thin, high–k dielectric layers conformally and pin-hole free on high AR substrates is atomic layer deposition (ALD). ALD is a type of chemical vapor deposition technique in which the chemical reaction is split up into two sequential, self-limiting reactions with the surface that ensures high quality films with great uniformity. Furthermore, ALD gives precise thickness control down to the Ångstrom level while staying at low processing temperatures (below 500° C).

Plasma-enhanced ALD (PEALD) is a rather new enhancement in which plasma species (radicals, ions) are utilized as an oxidizer instead of water vapor. This facilitates deposition at lower temperatures because the process depends less on the thermal energy available at the surface. Since the plasma species are more reactive, fewer ligands are left unreacted in the deposited film resulting in lower impurity concentrations and improved material properties. However, conformal coverage of high AR substrates is more problematic for PEALD due to the unstable nature of the excited plasma species.

In this thesis, work on PEALD of TiO_2 on high AR trenches will be presented and studied by transmission electron microscopy (TEM) as well as grazing incidence X-ray diffraction. TEM reveals that the coverage of PEALD TiO_2 on these substrates can be improved by increasing the plasma exposure time during each deposition cycle. Also, the effect of plasma during PEALD on the crystallization of TiO_2 will be investigated showing that plasma can be applied to crystallize the film. Then PEALD of the high–k perovskite material $BaTiO_3$ (BTO) will be explored where PEALD thereof has not been reported in literature up to this date, showing potential for future DRAM applications. Additionally, TEM shows that plasma (like in the case of TiO_2) can be used to crystallize the as-deposited BTO film partially which increases the dielectric constant of the film. Lastly, we will report the best electrical performance achieved up to this date (at a processing temperature as low as 250 °C) for Al-doped BTO deposited on a Zr-doped TiN electrode. These results, we believe, may be the stepping stone for next generation high–k dielectric films for DRAM and novel energy storage applications.

Zusammenfassung

Schlüsselelemente der heutigen Technologie wie der Metall–Oxid–Halbleiter Feldeffekt Transistor und der dynamische random-access memory (DRAM) folgen dem Trend der Miniaturisierung. Das verlangt, dass die dielektrische Schicht, die eine wichtige Komponente in diesen Strukturen ist, dünner wird. Da die Miniaturisierung schnell voranschreitet, nähern sich die Gerätekomponenten den fundamentalen physikalischen Limitierungen: Für das meist verwendete Gate Dielektrikum SiO_2 fängt direktes Tunneln bei Dicken weniger als 3 nm an. Es gibt zwei Hauptstrategien um die Kapazität zu erhöhen, ohne die Dicke der dielektrischen Schicht weiter zu verringern. Eine ist es, Oberflächen zu nutzen die ein hohes Aspektverhältnis (AV) aufweisen, um die effektive Oberfläche zu vergrößern. Die andere ist es, high–k Materialien anstatt SiO_2 zu verwenden.

Die Schlüsseltechnologie um ultra-dünne, high–k dielektrische Schichten gleichmäßig und ohne jeglicher Löcher auf Substrate mit hohem AV aufzutragen ist atomic layer deposition (ALD, wtl. Atomlagenabscheidung). ALD ist eine Art von chemischer Gasphasenabscheidung, in der die chemische Reaktion in zwei sequenzielle, selbst-limitierende Reaktionen mit der Oberfläche aufgeteilt wird, was Filme mit hoher Qualität und guter Uniformität gewährleistet. Außerdem kann ALD die Dicke kontrollieren auf dem Ångstrom Level, während die Prozesstemperaturen trotzdem niedrig bleiben (unter 500 °C).

Plasma-erweitertes ALD (PEALD) ist eine eher neue Erweiterung in der Plasma Teilchen (Radikale, Ionen) anstatt Wasserdampf zur Oxidierung verwendet werden. Das ermöglicht die Abscheidung bei niedrigeren Temperaturen, weil der Prozess weniger von der thermischen Energie auf der Oberfläche abhängt. Da die Plasma Teilchen reaktiver sind, bleiben weniger un-reagierte Liganden im abgeschiedenen Film, was zu niedrigeren Unreinheitskonzentrationen und besseren Materialeigenschaften führt. Allerdings die gleichmäßige Überdeckung von Substraten mit hohem AV ist problematischer für PEALD wegen der Instabilität der angeregten Plasma Teilchen.

In dieser Dissertation wird Arbeit zu PEALD von TiO_2 auf Graben mit hohem AV präsentiert und mit Transmissionselektronenmikroskopie (TEM) und auch Röntgendiffraktometrie mit streifendem Einfall studiert. TEM zeigt, dass die Überdeckung von PEALD TiO_2 auf diesen Substraten verbessert werden kann indem man die Plasma Einwirkungszeit während jedes ALD Zyklus' verlängert. Auch wird der Effekt von Plasma während PEALD auf die Kristallisation von TiO_2 untersucht und zeigt, dass Plasma verwendet werden kann, um den Film zu kristallisieren. Dann wird PEALD von dem high–k Perowskit $BaTiO_3$ (BTO) untersucht, wo PEALD davon aktuell noch nicht in der Literatur erwähnt wurde, welches Potenzial für zukünftige DRAM Anwendungen zeigt. Zusätzlich zeigt TEM, dass Plasma (wie auch im Fall von TiO_2) verwendet werden kann, um den Film teilweise zu kristallisieren und dadurch die dielektrische Konstante des

Films zu erhöhen. Zuletzt berichten wir die besten elektrischen Betriebseigenschaften erreicht bis zum heutigen Tag (bei einer Prozesstemperatur so niedrig wie 250 °C) für Al-dotiertes BTO aufgetragen auf einer Zr-dotierten TiN Elektrode. Wir glauben, dass diese Resultate das Sprungbrett für die nächsten Generationen von high–k dielektrischen Filmen für DRAM und neuartigen Energiespeicherungsanwendungen sein könnte.

Acknowledgment

To start off, it was a big step and great opportunity for me to do a large part of my research at Stanford University in Prof. Fritz Prinz' group *Nano Prototyping Laboratory*. Thanks to my supervisor Prof. Hans-Peter Karnthaler here in Vienna I had this opportunity of conducting research abroad. My career has been influenced by him in many ways and he always motivated me to achieve and pursue more. I have learned from him scientifically and personally. Prof. Karnthaler always supported and believed in me and for that, I will always be thankful.

While I was quite nervous but also excited to do research at Prof. Fritz Prinz' group NPL — this turned out to be the best decision I could have made personally and academically. Living abroad gives you the opportunity to define yourself new and challenge old patterns that were formed in the past. I am very thankful that I have had this option and I am even more grateful that Prof. Fritz Prinz took me as part of his amazing group at Stanford, mentored me, taught me and supported me. Being part of this inspiring environment full of highly qualified, smart and driven people made me learn and grow beyond what I imagined possible. For all of the support, help, discussions and encouraging words during my time at Stanford University, I would like to deeply thank Prof. Fritz Prinz.

Thank you to Prof. Peter Schattschneider and Prof. Robert Pond for agreeing to review my thesis on such a short notice making it possible for me to graduate in a timely manner.

Also, I would like to extend my thanks to my previous mentors Prof. Thomas Waitz and Prof. Christian Rentenberger, who supported me ever since I joined the group in Vienna *Physics of Nanostructured Materials* and were always there for me with good advice and always made me feel home and welcomed when I returned to Vienna. I feel very lucky to have had such incredible and supportive mentors and advisors over the course of my lifetime and career, although it is hard to find words to describe how thankful I am for that. As part of these mentors, I would like to thank all professors that have taught me physics over the course of my education and I would like to mention my high school teacher Mag. Johann Ganzberger, who was the first person sparking my interest for physics and motivating me to learn more. Also, I would like to thank Prof. Wolfgang Püschl for giving me the advice to start studying Physics at the University of Vienna.

It was a pleasure working together with my colleagues at NPL: A big thank you to Manca Logar, who taught me so much in the field of electron microscopy and always supported me. She was not only a smart and hard-working colleague but also a close friend during my time at Stanford. Thank you! I am lucky to be able to say that I worked closely together with Yongmin Kim, who is a brilliant mind with a good heart.

List of Acronyms

ALD	Atomic layer deposition
AR	Aspect-ratio
ARXPS	Angle-resolved X-ray photo-electron spectroscopy
BF	Bright field
BTO	Barium titanate, $BaTiO_3$
BST	Barium strontium titanate, $Ba_xSr_{1-x}TiO_3$
CCD	Charge-coupled device
CVD	Chemical vapor deposition
CTF	Contrast transfer function
DF	Dark field
DRAM	Dynamic random-access memory
EDX	Energy dispersive X-ray spectroscopy
EELS	Electron energy loss spectroscopy
EOT	Equivalent oxide thickness
FFT	Fast Fourier transformation
FIB	Focused ion beam
FN	Fowler-Nordheim (tunneling)
GPC	Growth per cycle
GIXRD	Grazing incidence X-ray diffraction
HRTEM	High resolution transmission electron microscopy
ICP	Inductively coupled plasma
IFFT	Inverse (filtered) fast Fourier transformation
MIS	Metal–insulator–semiconductor
MIM	Metal–insulator–metal
MOSFET	Metal–oxide–semiconductor field-effect transistor
PE	Plasma exposure
PEALD	Plasma-enhanced atomic layer deposition
PECVD	Plasma-enhanced chemical vapor deposition
PF	Poole-Frenkel (emission)
PSF	Point spread function
PVD	Physical vapor deposition
RMS	Root mean square
RTA	Rapid thermal annealing
SAD	Selected area (electron) diffraction
SC	Super-cycle
STO	Strontium titanate, $SrTiO_3$

STEM	Scanning transmission electron microscopy
STM	Scanning tunneling microscopy
TAT	Trap-assisted tunneling
TDMA	Tetrakis–dimethylamido, $Ti[N(CH_3)_2]_4$
TEM	Transmission electron microscopy
TTIP	Titanium–tetraisopropoxide, $Ti[OCH(CH_3)_2]_4$
UPS	Ultraviolet photo-electron spectroscopy
WF	Work function
WKB	Wentzel-Kramers-Brillouin (approximation)
WPOA	Weak phase-object approximation
XPS	X-ray photo-electron spectroscopy
XRD	X-ray diffraction
XRR	X-ray reflectivity

List of Symbols

ϵ_0	Vacuum permittivity $[8.854 \cdot 10^{-12} \text{ F/m}]$
μ_0	Vacuum permeability $[1.257 \cdot 10^{-6} \text{ V} \cdot \text{s}/(\text{A} \cdot \text{m})]$
e	Elementary charge $[1.602 \cdot 10^{-19} \text{ C}]$
k_{B}	Boltzmann constant $[1.381 \cdot 10^{-23} \text{ J/K}]$
h	Planck constant $[6.626 \cdot 10^{-34} \text{ J} \cdot \text{s}]$
$\hbar$	Reduced Planck constant $\hbar = h/(2\pi)$
m_0	Free electron mass $[9.109 \cdot 10^{-31} \text{ kg}]$
ϵ or ϵ_{r}	(Relative) permittivity, dielectric constant (also k or κ)
λ	Wavelength
d	Thickness
C	Capacitance
A	Area of capacitor
a	Area enhancement factor
$E_{\text{BD}} = \lvert\vec{E}_{\text{BD}}\rvert$	Breakdown field strength
m_{eff}	Effective electron mass
J	Tunneling current
V	Bias
V_{FB}	Flat-band voltage
E	Energy
$E_{\text{C}}, E_{\text{V}}, E_{\text{vac}}$	Energy levels of the conduction band, valence band and vacuum
E_{F}	Fermi-level
E_g	Band gap
T	Temperature
χ	Electron affinity
ϕ, Φ	Work function (WF)
ϕ_B	Schottky barrier height
ϕ_T	Trap energy level
n_T	Spatial trap concentration
N_A	Doping level
n_i	Intrinsic carrier concentration
$\Psi(x,t), \psi(x)$	Time-dependent and time-independent wave function
$V(x)$	Potential energy
m	Mass
$\vec{E}$	Electric field
$\vec{D}$	Electric displacement field

$\vec{B}, \vec{H}$ Magnetic fields

$\chi(\omega)$ Dielectric susceptibility

$\vec{P}$ Polarization

$\vec{M}$ Magnetization

ρ Charge density

$\vec{j}$ Current density

Γ Damping constant harmonic oscillator

ω_0 Natural frequency harmonic oscillator

ω_p Plasma frequency

d_{hkl} Crystalline plane spacings of orientation (hkl)

Table of Contents

CHAPTER 1

Introduction

Contents

Key pieces of modern day technology such as the metal–oxide–semiconductor field-effect transistor (MOSFET) and the dynamic random-access memory (DRAM) keep following the trend of down-sizing. This requires the dielectric layer that is a crucial component in these structures to reduce its thickness. In the past 100 years device dimensions have reduced by a factor of 10^6 and as down-scaling continues device features approach the physical limit of 0.3 nm (distance between Si atoms). Figure 1.1 illustrates how the junction depth and gate oxide thickness of the MOSFET decreased in the past 40 years.
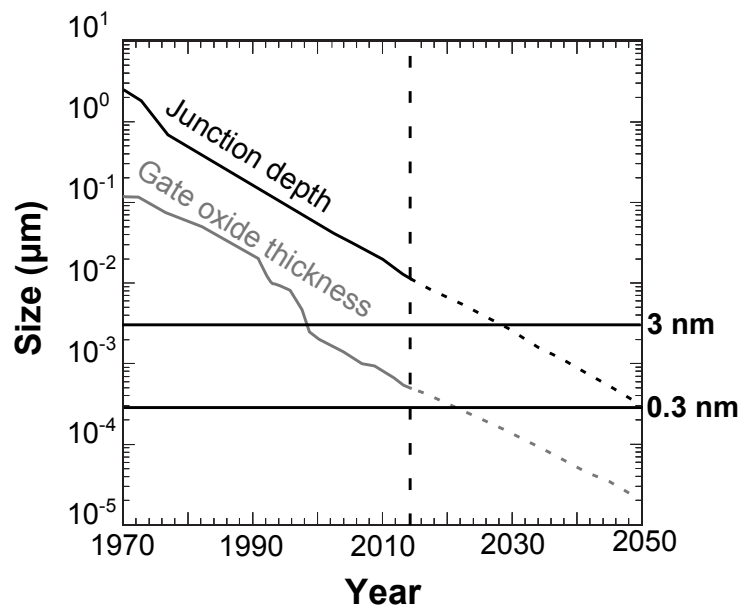
Figure 1.1.
Down-scaling of the junction depth and gate oxide thickness in a MOSFET device in the past 40 years.[1]

Long before the ultimate physical limit is reached, very thin dielectric layers show leaking current when voltage is applied. For the most commonly used gate dielectric SiO_2 a thickness of 3 nm is the ultimate lower limit due to direct tunneling of electrons through the layer.[2] In the past, up to the 65 nm node, SiO_2 was a suitable gate dielectric. But even for thicker layers other mechanisms can cause the dielectric to break down. Therefore, to tailor a dielectric structure that has high dielectric breakdown strength (that is the electric field strength at which the dielectric layer is breaking down, i.e. is permanently damaged and leaks currents) and thin physical thickness at the same time it is crucial to understand the mechanisms and the underlying physics that can cause dielectric breakdown.

The DRAM consists of a MOSFET that acts as an on/off switch and a capacitance C that stores either a '1' (charged) or a '0' (discharged). An array of these two components makes up the DRAM. Using the select line one can select one specific capacitor and read/write a '1' or a '0' via the data line (cf. Figure 1.2). The ability of a dielectric material to store charges at a given bias is given by the capacitance

$$C = \epsilon_0 \cdot \epsilon_r \cdot \frac{A}{d} \qquad \textbf{[1.1]}$$

where ϵ_r is the dielectric constant of the material, ϵ_0 is the permittivity of vacuum, A is the area of the capacitor and d is the distance between the plates. As described above the use of high–k ($\equiv$ high ϵ) dielectric materials is necessary as the thickness of the dielectric layer approaches fundamental limitations. Hence, the term equivalent oxide thickness (EOT) is defined making it easier to compare different dielectric materials and its capacitance. The EOT of a layer of a high–k material ($\epsilon_k > \epsilon_{\mathrm{SiO_2}}$) is equal to the physical thickness it would have if the layer was $\mathrm{SiO_2}$:

$$\mathrm{EOT} = d \cdot \frac{\epsilon_{\mathrm{SiO_2}}}{\epsilon_k} \qquad \textbf{[1.2]}$$

Inserting this into Equation 1.1 shows that the EOT is inverse proportional to the capacitance

$$C = \epsilon_0 \cdot \epsilon_{\mathrm{SiO_2}} \cdot \frac{A}{\mathrm{EOT}} \qquad \textbf{[1.3]}$$
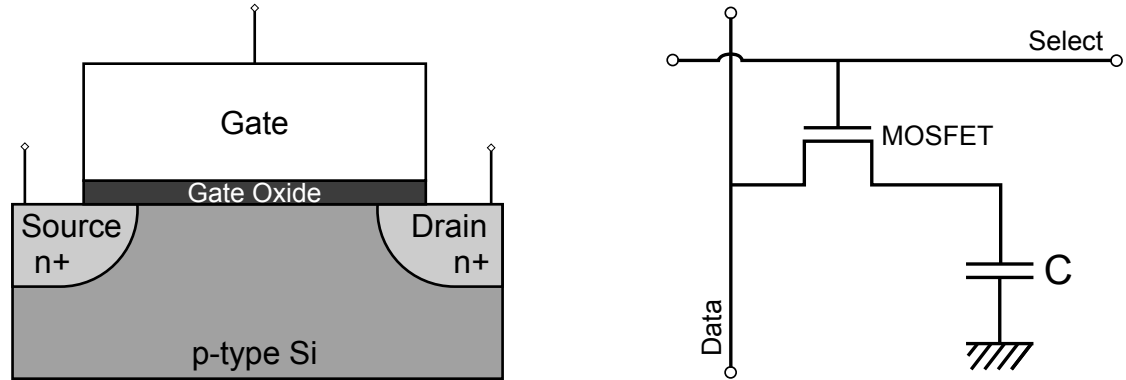
Figure 1.2.

Illustration of MOSFET and DRAM device structures.

The down-scaling of the DRAM requires the storage node size (i.e. the area of one capacitor) to decrease rapidly while the physical thickness of the dielectric has reached a limit and has not decreased below 5 nm over the last decades. In order to sustain the capacitance needed for the operation of a DRAM ($\sim$25 fF, almost constant over the past 10 years[3]) the dielectric constant has to go up and hence the EOT has to decrease accordingly, as seen in Figure 1.3.
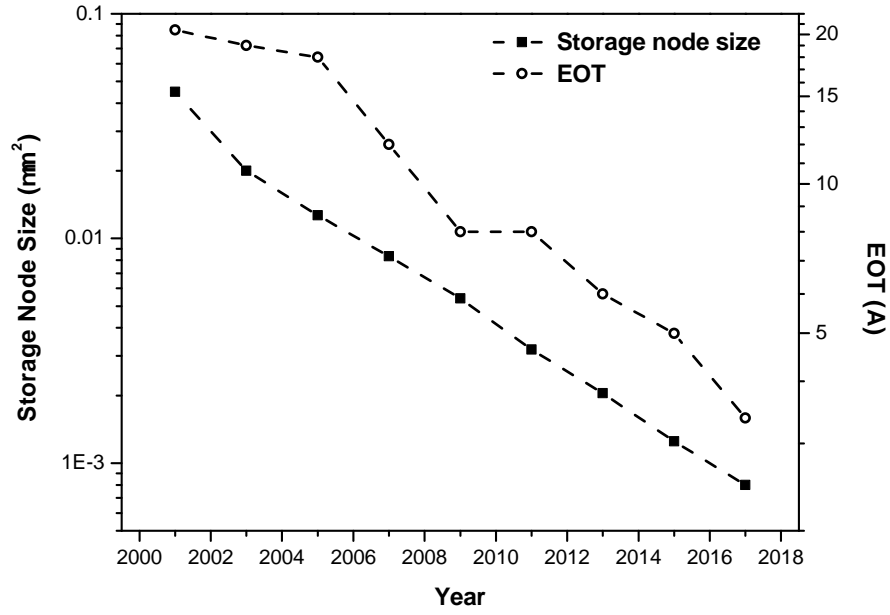
Figure 1.3.

Storage node size and EOT are plotted logarithmically between year 2000 and 2017. Values are projected past 2013.[3–6]

Furthermore, the energy u stored in a polarized material is given by ($\vec{E}$ is the electric field)

$$u = \frac{1}{2} \cdot \epsilon_0 \cdot \epsilon_r \cdot \left|\vec{E}\right|^2 \tag{1.4}$$

This shows that there are two parameters that can be tuned in order to maximize the stored energy in a dielectric layer: 1) Its dielectric constant ϵ_r and 2) The highest electric field that can be applied without the layer breaking down, the so-called electric breakdown field E_{BD}. Figure 1.4 plots different promising materials in terms of dielectric constant and breakdown field. According to this, in the next section, the selection of a suitable material will be discussed.
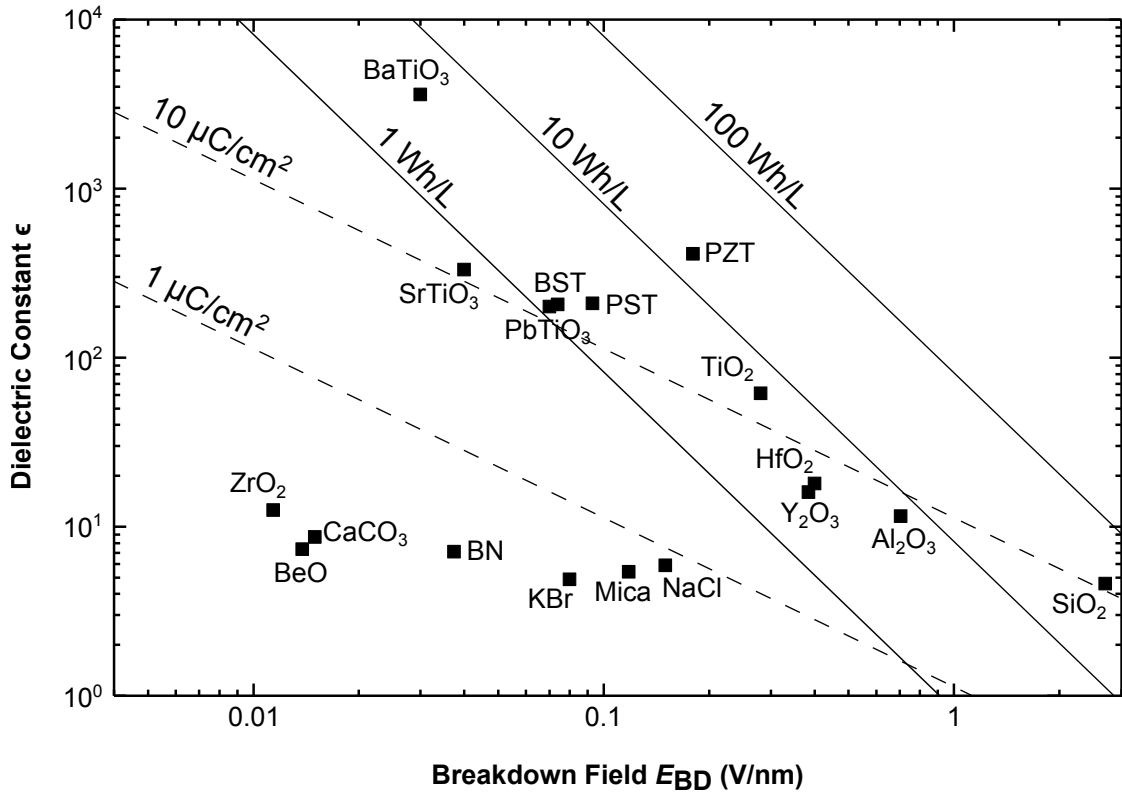
Figure 1.4.

Material overview of breakdown strength versus dielectric constant.[7–10] Solid lines are lines of constant energy density (Watt–hour per liter). Dashed lines represent lines of constant charge densities (micro–Coulomb per square–centimeter).

1.1

Thin Film Deposition on High Aspect-Ratio (AR) Surfaces

Independent of the dielectric materials selected, one way of increasing the capacitance in a DRAM device is to increase the effective surface area of the capacitor. This is done mostly by etching deep trenches into a thermally grown amorphous SiO_2 substrate. These trenches have a very high aspect ratio (AR) and hence increase the surface area. The increased capacitance is given by

$$C_i = \epsilon_0 \cdot \epsilon_r \cdot \frac{A_{\text{eff}}}{d} = \epsilon_0 \cdot \epsilon_r \cdot \frac{A_{\text{proj}}}{d} \cdot a \qquad \textbf{[1.5]}$$

where A_{eff} is the increased effective surface area of the high AR substrate, A_{proj} is the projected area of the planar substrate and $a = A_{\text{eff}}/A_{\text{proj}}$ is the so-called area enhancement factor.

1.1.1 Atomic Layer Deposition (ALD)

The key enabling technique to deposit ultra-thin, high–k layers conformally and pin-hole free on high AR substrates is atomic layer deposition (ALD). ALD is a type of chemical vapor deposition (CVD) technique in which the chemical reaction is split up into two sequential, self-limiting reactions with the surface.[11] In contrast to CVD, the self-limiting nature of ALD ensures high quality and great uniformity of thin layers. Furthermore, ALD gives precise thickness control on the Ångstrom level while staying at low temperatures (below 500° C).

For the deposited dielectric layer onto the high AR trench substrate we define a step coverage in order to quantify the uniformity and quality of the deposited film as follows:

$$\text{Step coverage} = \frac{d_{\text{bottom}}}{d_{\text{top}}} \cdot 100 \text{ \%}. \qquad \textbf{[1.6]}$$

The thicknesses d_{bottom} and d_{top} are indicated in Figure 1.5.
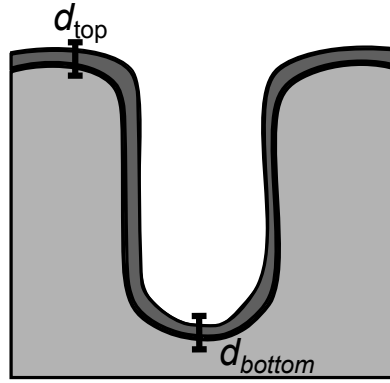
Figure 1.5.

Illustration of a high AR trench surface is shown indicating the measured thicknesses. Light gray is the SiO_2 substrate whereas dark gray is the high–k dielectric layer deposited by ALD.

1.1.2 Plasma-Enhanced Atomic Layer Deposition (PEALD)

ALD is a deposition technique that is a well studied and known process whereas plasma enhanced ALD (PEALD) is a rather new enhancement. PEALD is a variant of ALD which utilizes plasma species (predominantly radicals) as an oxidizer instead of water vapor. With PEALD the creation of radical species takes place in the gas phase. This facilitates deposition at lower temperatures because the process depends less on the thermal energy available at the surface. Since the plasma species are more reactive with precursor ligands, fewer ligands are left unreacted in the product material. Such lower impurity concentration may result in improved material properties compared to conventional ALD. Plasma species can also react with precursors not sufficiently reactive

with water, enabling the use of a larger variety of materials. Lastly, the throughput can be greatly improved because oxygen can be pumped out faster than water vapor.

Up till now a disadvantage of PEALD compared to thermal ALD is the inferior step coverage of 3–D surfaces which are crucial for DRAM devices as discussed before. The oxidant species in PEALD, such as O radicals in the singlet state, are in excited states, and therefore not stable. Plasma species can recombine at the sidewalls of 3–D structures with a high AR when diffusing down into these features. In this thesis, a way to tackle this drawback is presented.

> **2** — **Selecting High–k Materials: Facing the Dilemmas**

When selecting a promising candidate for a next generation high–k dielectric material one has to be aware of the following three dilemmas arising from the trade-off between high capacitance and low leakage currents:

- **Geometric dilemma:**
  Thin vs. thick dielectric layer: A thin layer has a high capacitance (low EOT) but large leakage currents, whereas a thick layer shows a lower capacitance (high EOT) but with reduced leakage currents.

- **Structural/Morphological dilemma:**
  For dielectric materials, in general, its crystalline phase/structure tends to have much higher dielectric constants (resulting in a lower EOT), but in turn crystalline grain boundaries act as leakage pathways that increase the currents through the film. Amorphous structures on the other hand tend to show lower leakage currents but have lower dielectric constants (high EOT).

- **Material dilemma:**
  As seen in Figure 1.2, materials that tend to have a high breakdown strength have a low dielectric constant (resulting in a higher EOT) and vice versa. This trend is also predicted by a thermochemical model of breakdown that arrives at an approximate relationship $E_{\mathrm{BD}} \propto 1/\sqrt{k}$ that holds over a wide range of dielectric materials.[12]

While the first dilemma is a fundamental property of a capacitor with a dielectric film (hence cannot be overcome) there are certain strategies to tackle the two latter trade-offs. The strategies used to face these dilemmas in this thesis are illustrated in Figure 1.6. For the structural/morphological dilemma the approach is to either make a bilayer structure of an amorphous thin film and a crystallized film on top of that of the same material or to intermix small crystallites into the amorphous phase of the dielectric film. In both cases, the crystallized area increases the overall dielectric constant (lower EOT) while the amorphous part blocks off the leakage current. Note, that in the mixed crystallites case, there is a sweet-spot of crystalline fraction inside the amorphous film because if the crystalline fraction is too low the dielectric constant stays low as well, whereas if the crystalline fraction is too high the crystallites will start touching and forming grain boundaries that will act as leakage pathways. For both strategies PEALD will prove to be useful in selectively generating crystallites by plasma. For overcoming the material dilemma the strategy is to use a very thin blocking layer of a material that has a very high breakdown strength with a low dielectric constant (still higher than SiO_2 though) and a thicker layer on top of a material that has a very high dielectric constant but a fairly low breakdown strength.
Another way to overcome these dilemmas, not depicted in the Figure, is doping of high–k materials in order to achieve a low free carrier concentration in as-deposited ALD

films and to compensate crystal defect states. The doping process can be incorporated directly into ALD runs by using recipes with super–cycles that consist of a single dopant pulse followed by a specified number of base material pulses.
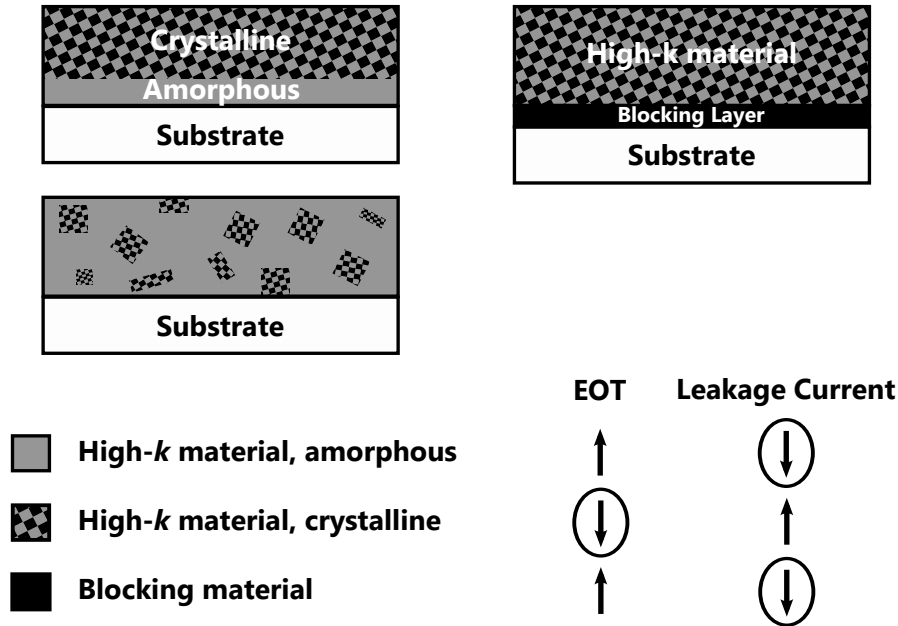
Figure 1.6.

Approaches to overcome the material and structural/morphological trade-offs: A bi-layer of amorphous and crystalline phase of the same material, an intermixed film of crystallites inside the amorphous matrix and a thin blocking layer of a low leakage material combined with a thicker layer with a very high dielectric constant on top. Legend qualitatively states which properties each material form has (EOT, leakage current).

2.1

High–k Perovskites: The Titanates

As seen in Figure 1.4 the titantates $BaTiO_3$ (BTO), $SrTiO_3$ (STO) and $(Ba,Sr)TiO_3$ (BST) are promising candidates for high–k dielectric materials. These perovskite structures exhibit very high dielectric constants of up to 10^3.[13–15] The dielectric constant strongly depends on the structure (e.g. each phase of TiO_2, anatase, rutile, brookite have different dielectric constants) as well as the quantum confinement effect that changes the band gap of the deposited layer also leading to a lower dielectric constant than in the bulk.[16, 17] Details about reduced dielectric constants in thin films will be discussed in the next chapter.

One of the practical challenges of ALD of Ba and Sr compounds is known to be the repeatability issue. Because the size of metal ions is large, Ba/Sr atoms tend to have a large coordination number. Therefore, the precursors can conglomerate and change

its properties easily. Additionally, Ba precursors are known to have a low volatility, therefore they need relatively high evaporation temperatures. While BTO, BST have been reported to be successfully used by CVD,[13] ALD seems to be more challenging. Deposition was successfully reported by ALD,[15, 18] whereas PEALD of these materials is mostly unexplored and there is a lot of room for improvement.

There are several literature reports available on dielectric properties of BTO, STO and BST. Table 1.1 lists relevant publications along with the material, deposition method, highest processing temperature and dielectric properties. While good electrical performance has been reported in these publications, all of them require processing steps with a high temperature (> 500 °C) such as a thermal anneal to crystallize the amorphous film into the perovskite phase to achieve low EOTs. In this thesis, plasma will be facilitated to achieve crystallization in the film without the need of a high temperature anneal.

Ref.	1st Author	Method	Material	Thickness (nm)	k	EOT (Å)	Leakage (A/cm^2) at 1 V	Temp. (°C)
[15]	Vehkamäki	ALD	STO	400	180	87 *	$5.0 \cdot 10^{-4}$	500
			BTO	–	165	–	–	500
[19]	Wang	ALD	STO,BTO	90	400	8.0	–	620
[13]	Tohma	CVD	BTO	520	96	211 *	$1.0 \cdot 10^{-5}$ **	700
[20]	Chen	PLD	BST	150	1370	6.9 *	$1.0 \cdot 10^{-6}$ **	780
[14]	Vehkamäki	ALD	BTO	32	73	18	$1.0 \cdot 10^{-7}$	600
[21]	Lee	ALD	STO	20	108	7.2	$3.0 \cdot 10^{-7}$ **	700
[22]	Lee	ALD	STO	21 *	146	5.7	$6.0 \cdot 10^{-8}$ **	650
[23]	Popovici	ALD	STO	10	181	5.6	$2.0 \cdot 10^{-6}$ **	600
[24]	Liu	PLD	BST	580	700	32 *	$4.4 \cdot 10^{-9}$	500
[25]	Aslam	PEALD	STO	30	78 *	15 **	$1.0 \cdot 10^{-5}$ **	650
[26]	Lee	ALD	STO	14.2	129 *	4.3	$1.0 \cdot 10^{-7}$ **	650

Table 1.1.

List of relevant publications on dielectric properties of titanates reported in literature. The references are listed in chronological order. Unmarked values were directly stated by the original authors of the respective publication, whereas values marked with * were calculated using other available parameters and values marked with ** were extracted from graphs.

2.2

Low Leakage Current Oxides

Al$_2$O$_3$ and HfO$_2$ are very suitable blocking layers for improving the breakdown strength as shown in previous work.[27] Furthermore, unlike the more complex titantate films these films have been very well established in terms of deposition by ALD and PEALD with commercial precursors.

┌─ 3 ───┐
│ # Structure of this Thesis   │
└──┘

This thesis is divided into five chapters. In the introduction — the *first chapter* — the need for novel high–k materials was motivated and the promising candidates as well as the deposition techniques were discussed.

Chapter two explains the basic theoretical framework needed for understanding the physics behind high–k dielectrics as well as tunneling mechanisms through them.

The *third chapter* covers the experimental methods used for depositing and investigating thin high–k layers. Talking more in depth about the deposition techniques ALD and PEALD. Then explaining the X-ray techniques used for characterizing structure and chemistry. Also, optical techniques (UV, visible) will be briefly discussed. Lastly, transmission electron microscopy (TEM) will be discussed in detail and how the sample preparation works.

In *chapter four* I will thoroughly explain all the experimental results and discuss them. Mostly, this chapter will comprise of manuscripts that either have been published, submitted or are going to be submitted for publication. First, the high AR coverage of PEALD TiO_2 will be presented. Then the effect of plasma on the crystallization of PEALD TiO_2 will be explained. In the next section PEALD of high–k $BaTiO_3$ will be shown and in the following chapter its crystallization by plasma will be studied by TEM. Then, the metal TiN electrode will be investigated and how doping can affect its work function (WF) and in turn is able to reduce leakage currents of a device. Lastly, Al-doping of PEALD $BaTiO_3$ is studied and how this can both keep the dielectric constant high but reduce leakage currents significantly and achieve electric performances not equaled up to this date in literature.

Chapter five then finishes with a short summary and conclusion of this thesis' work with an outlook for future research.

<div style="border:1px solid">

4

Individual and Group Research Statement

</div>

The work presented in this thesis is based on my participation in group research efforts in Prof. Fritz Prinz group at Stanford University. His group consists of a large number of graduate and undergraduate students, postdoctoral scholars and professors working in teams on various projects. Within a project, members have specific roles and responsibilities, but all of the research performed is highly collaborative and interdisciplinary. Specific contributions of the collaborators are listed below. All work except for what is explicitly listed below was carried out by the author.

In chapter 1, Figure 1.3 and Table 1.1 were adapted from Takane Usui.
In chapter 2, the original FN-tunneling simulation code was written by Christine Donnelly and refined by myself.
In chapter 4, section 1 PEALD of TiO_2 was carried out by J Provine. TEM was carried out working together with Manca Logar. GIXRD synchrotron measurements were done together with Takane Usui.
In chapter 4, section 2 XRD measurements were carried out by Takane Usui. TEM work was done by Manca Logar and myself.
In chapter 4, section 3 PEALD of $BaTiO_3$ and its characterization was done working together with Yongmin Kim and Jihwan An. XPS was carried out by Yongmin Kim. AFM was done by Dickson Thian.
In chapter 4, section 4 AFM was carried out by Dickson Thian. XPS was done by Yongmin Kim. XRR was conducted by Takane Usui.
In chapter 4, section 5 PEALD of TiN and ZrO_2 was carried out by J Provine.
In chapter 4, section 6 PEALD of Al-doped $BaTiO_3$ and its electrical characterization as well as XPS were carried out by Yongmin Kim. Band gaps were measured by Anup Dadlani.

Quarter 4 largely contains the following papers and proceedings that were published, submitted or are still in preparation:

- *Enhanced Step Coverage of TiO_2 Deposited on High Aspect Ratio Surfaces by Plasma-Enhanced Atomic Layer Deposition*, P. Schindler, M. Logar, J Provine and F. B. Prinz, **ACS Langmuir, 2015, 31 (18) 5057–5062**
  In which I am the first author, because I mainly wrote the manuscript, did the majority of TEM preparation and characterization and did the literature research.

- *Plasma-Enhanced Atomic Layer Deposition of $BaTiO_3$*, P. Schindler*, Y. Kim*, D. Thian, J. An and F. B. Prinz, **submitted**
  In which I am first author together with Yongmin Kim, as we both did the majority of the experiments and the writing as well as planning.

13

- *Atomic Layer Deposition of Barium Oxide and High-k Barium Titanate Thin Films Using Novel Pyrrole Based Precursor*, S. Acharya*, J. Torgersen*, S. Walch, Y. Kim, P. Schindler, S. Xu, T. Usui, C. Schildknecht and F. B. Prinz, **submitted**
  In which I am fifth author, because I contributed in doing cross-sectional HRTEM for their samples.

- *Plasma-Enhanced Atomic Layer Deposition of Al-Doped Barium Titanate*, Y. Kim*, P. Schindler*, S. Acharya, A. L. Dadlani, J Provine, J. An and F. B. Prinz, **in preparation**
  Again, here I am together with Yongmin Kim equally contributed first author: Both of us conducted the majority of the experimental planning and characterization.

- *Molecular Oxygen Reactions with Tetrakisdimethylamido-metal Precursors for Atomic Layer Deposition*, P. Schindler, J Provine, J. Torgersen, K. Kim, H. P. Karnthaler and F. B. Prinz, **in preparation**
  I will be first author on this manuscript as I did most of the planning together with J Provine and doing a big part of the characterization work. The manuscript will be written mainly by him and myself.

- *TEM Studies of High Aspect Ratio Surfaces Coated with Thin Dielectric Films by Atomic Layer Deposition*, P. Schindler, M. Logar, T. Usui, J Provine, H. P. Karnthaler and F. B. Prinz, **Conference Proceedings for IMC 2014, Prague**
  I presented a poster at the IMC 2014 in Prague and wrote this abstract.

- *Molecular Oxygen Reactions with Tetrakisdimethylamido-metal Precursors for Atomic Layer Deposition*, J. Provine, P. Schindler and F.B. Prinz, **Conference Proceedings for ALD 2015, Portland**
  This is an abstract of our above mentioned paper in preparation that J Provine will present at the ALD 2015 in Portland.

CHAPTER ▐▐

Theoretical Framework

Contents

<div style="border:1px solid black; padding:10px;">

1 ─────────────────────────────────────

Physics of Dielectrics

</div>

In this section, the fundamentals of dielectric properties of materials will be reviewed starting from Maxwell's equations. Then arrive at the Maxwell's equations in matter and define the quantities dielectric displacement field, dielectric susceptibility, polarization and dielectric constant. After that, the Lorentz model for the frequency dependence of the dielectric constant will be discussed. In the last part, we will talk about dielectric constants of thin films and why they often are lower than its bulk counterpart.

1.1 ─────────────────────────────────────

Maxwell's Equations in Matter

To start with, we will assume the Maxwell's equations as given and refer to any standard textbook about electro-dynamics. In Equation 2.1 Maxwell's equations are stated in differential formulation (in SI units) being 4 differential equations for the electric field $\vec{E}$ and magnetic field $\vec{B}$ caused by the charge density ρ and the current density $\vec{j}$. The permittivity of free space is denoted as ϵ_0 and the permeability of free space as μ_0.

$$\vec{\nabla} \cdot \vec{E} = \frac{\rho}{\epsilon_0} \qquad \vec{\nabla} \cdot \vec{B} = 0$$

$$\vec{\nabla} \times \vec{E} = -\frac{\partial \vec{B}}{\partial t} \qquad \vec{\nabla} \times \vec{B} = \mu_0 \left(\vec{j} + \epsilon_0 \frac{\partial \vec{E}}{\partial t} \right) \qquad \text{[2.1]}$$

Now in a material with polarization $\vec{P}$ and magnetization $\vec{M}$ bound charges and bound currents emerge. The charge density ρ and the current density $\vec{j}$ can be split up in the following contributions:

$$\rho = \rho_f + \rho_b = \rho_f - \vec{\nabla} \cdot \vec{P} \qquad \text{[2.2]}$$

$$\vec{j} = \vec{j}_f + \vec{j}_b + \vec{j}_p = \vec{j}_f + \vec{\nabla} \times \vec{M} + \frac{\partial \vec{P}}{\partial t} \qquad \text{[2.3]}$$

where ρ_b are the bound charges, $\vec{j}_b$ the bound currents (static case) and $\vec{j}_p$ the polarization current. Index f stands for free contributions. Inserting these equations into Maxwell's equations and defining the electric displacement field $\vec{D}$ and the magnetic field $\vec{H}$ as

$$\vec{D} = \epsilon_0 \vec{E} + \vec{P} \qquad \text{[2.4]}$$

$$\vec{H} = \frac{1}{\mu_0} \vec{B} - \vec{M} \qquad \text{[2.5]}$$

one arrives at Maxwell's equations in matter:

$$\vec{\nabla} \cdot \vec{D} = \rho_f \qquad\qquad \vec{\nabla} \cdot \vec{B} = 0$$

$$\vec{\nabla} \times \vec{E} = -\frac{\partial \vec{B}}{\partial t} \qquad \vec{\nabla} \times \vec{H} = \vec{j}_f + \frac{\partial \vec{D}}{\partial t} \qquad\qquad \textbf{[2.6]}$$

1.2

Electric Displacement Field and the Dielectric Susceptibility

The simplest approach for Equation 2.4 is assuming a linear response between $\vec{D}$ and $\vec{E}$:

$$\vec{D} = \epsilon_0 \vec{E} + \vec{P} = \epsilon_0 \epsilon \vec{E}$$

$$\Rightarrow \vec{P} = \epsilon_0 (\epsilon - 1) \vec{E} = \epsilon_0 \chi \vec{E} \qquad\qquad \textbf{[2.7]}$$

Where $\chi = \epsilon - 1$ is the so-called dielectric susceptibility and ϵ (sometimes ϵ_r) is the (relative) dielectric permittivity.

This linear, isotropic, local, instantaneous simplification of ϵ is a good model to start with but the following generalizations may be necessary to model more complex cases:

- **Nonlinear:**
  The electric displacement field might depend on higher orders of the electric field. This is the case for non-linear optical materials.

  $$\vec{D} = \epsilon_0 (\epsilon \vec{E} + \chi^{(2)} \vec{E}^2 + \chi^{(3)} \vec{E}^3 + \ldots) \qquad\qquad \textbf{[2.8]}$$

- **Anisotropic:**
  The electric displacement field might not be parallel to the electric field. This occurs for materials with birefringence. In this case ϵ is not a scalar, but a tensor.

  $$(\vec{D})_i = \sum_j \epsilon_0 \epsilon_{ij} (\vec{E})_j \qquad\qquad \textbf{[2.9]}$$

- **Non-local:**
  The dielectric constant ϵ may depend on the location as well.

  $$\vec{E}(x) = \int \epsilon^{-1}(x, x') \vec{E}_{\text{ext}}(x') \, \mathrm{d}x' \qquad\qquad \textbf{[2.10]}$$

- **Time-delay:**
  Also there may be a time dependence of the response of the dielectric constant on the electric field.

  $$\vec{E}(t) = \int \epsilon^{-1}(t - t') \vec{E}_{\text{ext}}(t') \, \mathrm{d}t' \qquad\qquad \textbf{[2.11]}$$

1.3

Frequency Dependence of the Dielectric Constant

In addition to this generalizations listed above, the dielectric constant is actually a function depending on the frequency of an applied periodic field (or a light wave propagating through matter). For this purpose the Lorentz model will be reviewed that assumes matter to consist of electrons and ions forming a system of harmonic oscillators that are exited to forced oscillations. It is assumed that the ions and electrons are located at a equilibrium position within a solid. An external electric field displaces the charged particles from their equilibrium position whereas the surrounding atoms result in forces that drive the particles back into their equilibrium position. This force is assumed to be proportional to the displacement x resulting in harmonic oscillations with frequency ω_0 around the equilibrium position. The motion of the surrounding oscillators result in a dampening (with damping constant Γ) of these oscillations. For this model, it is assumed that the oscillators are isotropic (oscillations do not depend on direction of displacement) which in general is not correct due to preferred symmetries in crystalline solids.

The differential equation for the displacement x of an harmonic oscillator displaced by an external electric field is given by

$$\ddot{\vec{x}} + \Gamma\dot{\vec{x}} + \omega_0^2\vec{x} = -\frac{e}{m}\vec{E} \qquad \textbf{[2.12]}$$

which can be solved by a Fourier approach giving

$$\vec{x}(\omega) = -\frac{e}{m}\frac{1}{\omega_0^2 - \omega^2 - i\omega\Gamma}\vec{E}(\omega) \qquad \textbf{[2.13]}$$

The dipole moment $\vec{\mu}$ is given by that distance x times the elementary charge e. The polarization $\vec{P}$ then further is given by N, the number of atoms per unit volume times the dipole moment. Hence

$$\vec{P}(\omega) = N\vec{\mu}(\omega) = Ne\vec{x}(\omega) = \epsilon_0\chi(\omega)\vec{E}(\omega) \qquad \textbf{[2.14]}$$

gives the following dielectric susceptibility

$$\chi(\omega) = \frac{Ne^2}{\epsilon_0 m}\frac{1}{\omega_0^2 - \omega^2 - i\omega\Gamma} =: \omega_p^2\frac{1}{\omega_0^2 - \omega^2 - i\omega\Gamma} \qquad \textbf{[2.15]}$$

where ω_p is defined as the plasma frequency. Inserting this into Equation 2.7 gives

$$\epsilon(\omega) = 1 + \omega_p^2\frac{1}{\omega_0^2 - \omega^2 - i\omega\Gamma} = \epsilon'(\omega) + i\epsilon''(\omega) \qquad \textbf{[2.16]}$$

with the real and imaginary part being

$$\epsilon'(\omega) = 1 + \omega_p^2 \frac{\omega_0^2 - \omega^2}{(\omega_0^2 - \omega^2)^2 + \omega^2 \Gamma^2} \qquad \textbf{[2.17]}$$

$$\epsilon''(\omega) = \omega_p^2 \frac{\omega \Gamma}{(\omega_0^2 - \omega^2)^2 + \omega^2 \Gamma^2} \qquad \textbf{[2.18]}$$

Figure 2.1 plots the real and imaginary part of the dielectric function $\epsilon(\omega)$ as a function of frequency showing a resonance at $\omega = \omega_0$. Note that the width of the peak of $\epsilon''(\omega)$ gets broader with increasing damping constant Γ.
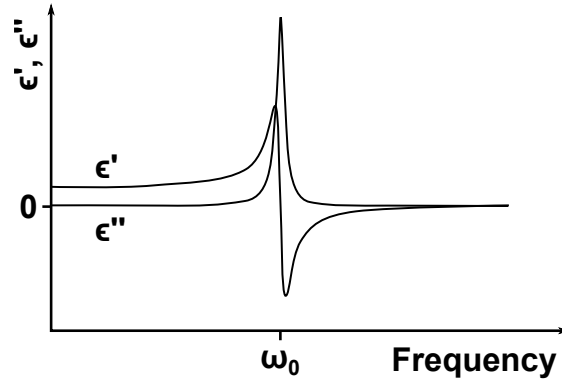
Figure 2.1.

$\epsilon'(\omega)$ and $\epsilon'(\omega)$ as a function of frequency ω is plotted for the Lorentz model. Resonance is observed at $\omega = \omega_0$.

For bulk dielectric materials usually the dielectric constant (often denoted ϵ or ϵ_r) that is given in literature is the real component of the dielectric function at the low frequency limit: $\epsilon'(\omega \to 0)$. At very low frequencies a lot of different mechanisms contribute to the dielectric behavior of the material but become blocked at higher frequencies (higher than the resonance frequency of each specific contribution). The following contributions are illustrated in Figure 2.2:

- Up to $\sim$ 1–10 Hz:
  Domain wall motion contributes to the dielectric constant.

- Up to $\sim 10^6$ Hz:
  Up to radio/ultra high frequencies (UHF) permanent dipoles contribute.

- Up to $\sim 10^{12}$ Hz:
  Ionic polarization shows a resonance in the infrared (IR) and/or visible spectrum.

- Up to $\sim 10^{15}$–10^{16} Hz:
  Up to UV frequencies there is a contribution of the electronic polarization.
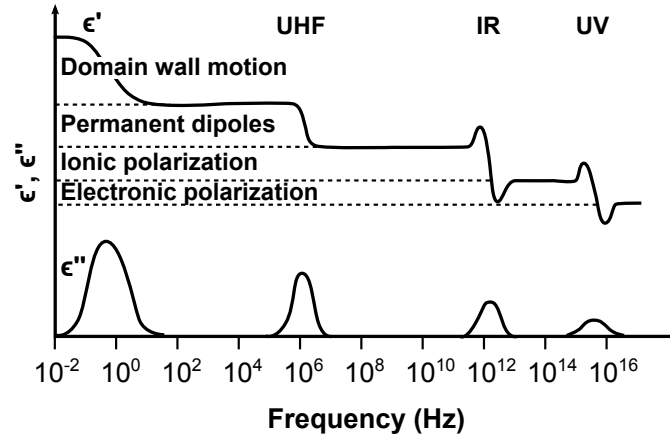
Figure 2.2.

Schematic plot of $\epsilon'(\omega)$ and $\epsilon''(\omega)$ as a function of frequency (over orders of magnitude) ω is shown for dielectric materials.

1.4

Dielectric Constants of Ultra-Thin Films

Materials with a very high bulk dielectric constant ($10^2 \sim 10^3$) such as the perovskites (BTO, STO, BST) often have much lower reported values for ultra thin films.[28] The reason for this phenomenon can either be ascribed to degradation in film quality or to the formation of interface layers between dielectric and the metal electrodes that have a lower dielectric constant. This low–k interface layer is also called dead layer and is formed because the dielectric polarization is locked at the interface adjacent to the metal electrode. These interfacial layers with a lower dielectric constant (ϵ_i) cause capacitances in series:

$$\frac{1}{C} = \frac{1}{C_i} + \frac{1}{C_b} + \frac{1}{C_i} \qquad \textbf{[2.19]}$$

where i stands for interface, and b for bulk. This capacitances in series of dead layers and bulk-like dielectric is illustrated in Figure 2.3.
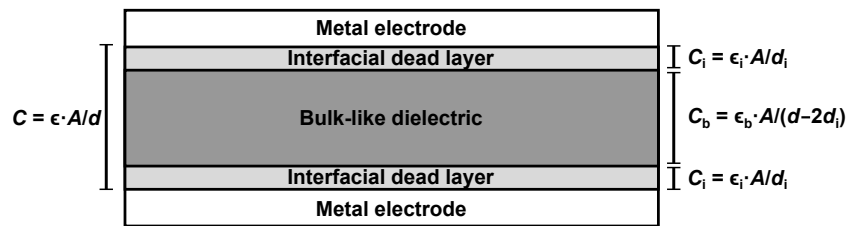
Figure 2.3.

Illustration of interfacial dead layers forming capacitors in series. Dielectric constants of the interface and the bulk-like region are denoted by i and b indices, respectively.

Hence, this can further be written as

$$\frac{d}{\epsilon} = \frac{2d_i}{\epsilon_i} + \frac{d - 2d_i}{\epsilon_b}$$

[2.20]

Where d is the total thickness of the layer and d_i is the thickness of one interfacial layer. ϵ is the dielectric constant of the whole structure, whereas ϵ_i and ϵ_b are the dielectric constants of the interface layer and bulk, respectively.

Equation 2.20 can be used for estimating how much the total dielectric constant is reduced by interfacial layers with a lower dielectric constant. For this purpose plots of ϵ/ϵ_b (in percent) are shown in Figure 2.4 at three different ratios between interfacial and bulk dielectric constants ($\epsilon_i/\epsilon_b = 1/2$, 1/5 and 1/10) for the case of a dead layer thickness d_i of (a) 0.5 nm and (b) 1 nm.

This shows that with increasing thickness d_i of the dead layer and/or decreasing interfacial dielectric constant ϵ_i the resulting dielectric constant reduces much more rapidly with decreasing film thickness.
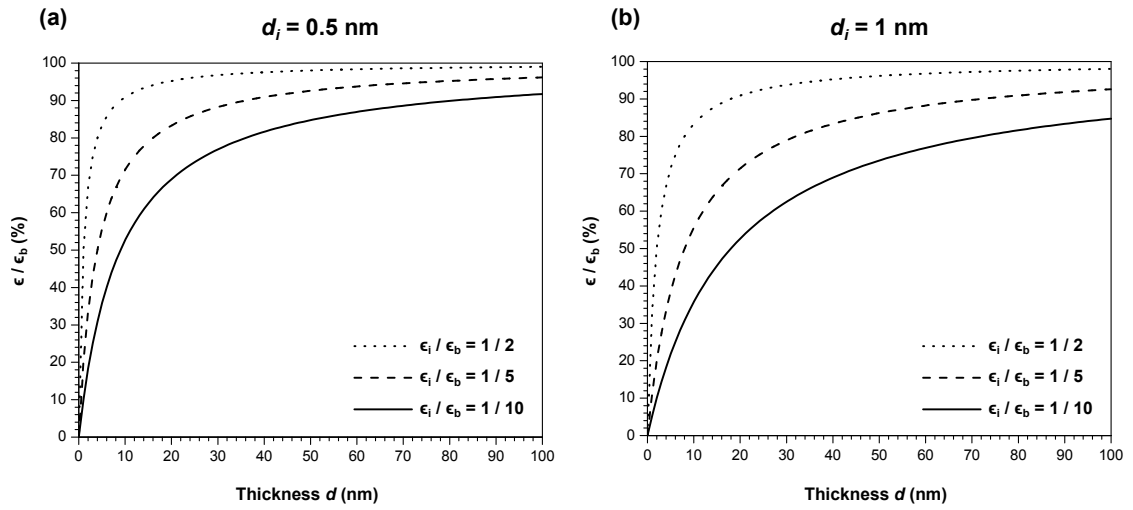
Figure 2.4.

Ratio between overall dielectric constant and bulk dielectric constant (ϵ/ϵ_b in percent) plotted at three different ratios between interfacial and bulk dielectric constants ($\epsilon_i/\epsilon_b = 1/2$, 1/5 and 1/10) for the case of a dead layer thickness d_i of (a) 0.5 nm and (b) 1 nm.

While film degradation can be an additional effect causing a reduced dielectric constant, ab-initio calculations for perfect (defect free, no impurities, no strain) thin film STO capacitors have shown that the effect of the dead layer on the resulting dielectric constant is intrinsic.[29] It was also shown by a Lorentz local field theory that this effect is a intrinsic geometric effect due to the different dipole moments in the surrounding at the surface compared to inside the bulk.[30] They have also shown that this effect is more pronounced in materials with a very high dielectric constant: A bulk value of $\epsilon_b = 10$ was reduced to $\epsilon_{n=10} = 9.602$ for the case of 10 layers of dipoles in thickness, whereas a bulk value of $\epsilon_b = 1000$ was reduced to $\epsilon_{n=10} = 164.2$ for the same case.[30]

This also agrees with the observations from Figure 2.4 because ϵ_b tends to be much larger compared to ϵ_i for materials with a high bulk dielectric constant. Conversely, the interface layer tends to have a similar dielectric constant to the bulk if the bulk value is already low to begin with.

Hence, for achieving higher dielectric constants in an ultra-thin film one has to pick a material with a high bulk dielectric constant and a thin interfacial dead layer at the metal electrode interface.

2 ────
| **Quantum Mechanical Tunneling through Dielectrics** |

In this section, first the basic quantum mechanical tunneling through a potential barrier will be reviewed. Then, a Fowler-Nordheim (FN) tunneling model will be presented and used to calculate tunneling currents through a dielectric stack of Al_2O_3 and $BaTiO_3$. Then Schottky and thermionic-field emission will briefly be explained. Lastly, mechanisms caused by defects in the dielectric such as trap-assisted tunneling (TAT), Poole-Frenkel (PF) mechanism, hopping conduction and grain boundary diffusion based tunneling will be discussed.

2.1 ────

Direct Tunneling Through a Potential Barrier

Tunneling through a one-dimensional potential barrier is discussed in many standard textbooks about quantum mechanics and is briefly summarized here. For a time-independent potential we can factorize the wave function

$$\Psi(x,t) = e^{-iEt/\hbar}\psi(x) \tag{2.21}$$

The time-independent (stationary) Schrödinger equation is

$$\left[-\frac{\hbar}{2m}\frac{\partial^2}{\partial x^2} + V(x) \right]\psi(x) = E\psi(x) \tag{2.22}$$

where E is the energy of the particle and $V(x)$ is the potential (a barrier with thickness a and height V_0) given by

$$V(x) = \begin{cases} 0 & \text{for } x < 0 \text{ or } x > a \\ V_0 & \text{for } 0 < x < a \end{cases} \tag{2.23}$$

The wave function of the particle left, inside and right to barrier has the form

$$\begin{aligned} \psi_{\text{left}} &= e^{ik_1 x} + re^{-ik_1 x} \\ \psi_{\text{inside}} &= Ae^{ik_2 x} + Be^{-ik_2 x} \\ \psi_{\text{right}} &= te^{ik_1 x} \end{aligned} \tag{2.24}$$

where

$$\begin{aligned} k_1 &= \sqrt{\frac{2mE}{\hbar^2}} \\ k_2 &= \sqrt{\frac{2m(E-V_0)}{\hbar^2}} \end{aligned} \tag{2.25}$$

24

Hence, the form of the wave function left and right to the barrier is the same but differ in the amplitudes, where r is the reflected amplitude and t is the transmitted amplitude. Using the continuity requirement of ψ and $\partial \psi / \partial x$ at the points $x = 0$ and $x = a$ gives four equations that determine r, t, A and B. In specific, for the transmissivity $T = |t|^2$ one obtains

$$T = |t|^2 = \frac{1}{1 + \frac{1}{4} \left(\frac{k_1}{k_2} - \frac{k_2}{k_1} \right)^2 \sin^2(k_2 a)} \qquad \textbf{[2.26]}$$

In the case of $E > V_0 > 0$ the transmission coefficient T shows oscillatory behavior where the case of $k_2 a$ being multiples of π leads to perfect transmission (caused by interference).

For the case of $0 < V_0 > E$ tunneling occurs through the barrier (classically not possible) leading to a non-zero T. Here $k_2 = i\kappa$ is purely imaginary leading to a decay of the wave function of the form

$$T = \frac{1}{1 + \frac{1}{4} \left(\frac{k_1}{\kappa_2} - \frac{\kappa_2}{k_1} \right)^2 \sinh^2(\kappa_2 a)} \qquad \textbf{[2.27]}$$

For $\kappa_2 a \ll 1$ this gives the simple form of

$$T \propto e^{-2\kappa_2 a} \qquad \textbf{[2.28]}$$

showing that the transmissivity decreases exponentially with increasing barrier width. An illustration of the potential of a one-dimensional barrier with a schematic plot of the probability $|\psi|^2$ is shown in Figure 2.5.
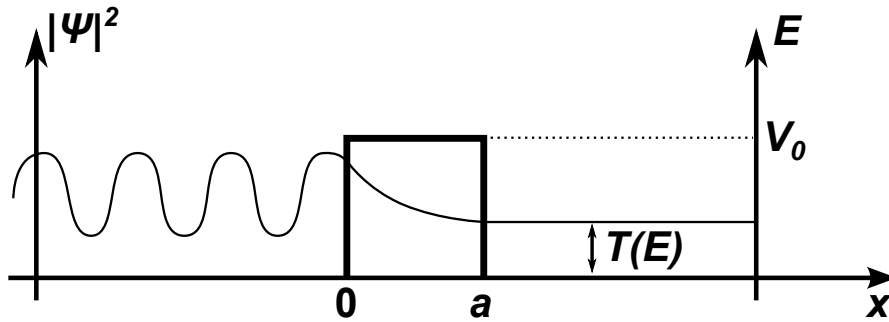
Figure 2.5.

Schematic illustration of $V(x)$ and $|\psi|^2$ for the one-dimensional potential barrier.

2.2

Schottky and Thermionic-Field Emission

In Schottky emission (or thermionic emission) electrons gain enough thermal energy to overcome the energy barrier between the metal Fermi level and the conduction band of the dielectric. The difference in energy is the Schottky barrier height $e\phi_{\mathrm{B}}$. At high temperatures this conduction mechanism is quite common. The following expression describes the Schottky current

$$J_{\mathrm{S}}(T, E) = A^* T^2 \exp\left[\frac{-e(\phi_{\mathrm{B}} - \sqrt{eE/(4\pi\epsilon_r\epsilon_0)})}{k_{\mathrm{B}}T}\right] \qquad \textbf{[2.29]}$$

where $A^* = 120 \cdot m_{\mathrm{eff}}/m_0$ is the effective Richardson constant, m_0 is the free electron mass, E is the electric field across the dielectric and T is the absolute temperature. It should be noted, that the Schottky barrier height may be lowered caused by image forces at the metal–oxide interface. Figure 2.6 illustrates an MIM structure and how electrons emit through the Schottky mechanism.

Thermionic field emission is a conduction mechanism between Schottky emission and field emission (i.e. tunneling). Through thermionic excitation electrons that are excited to half the height of the Schottky barrier can then tunnel more easily through the barrier that is triangular shaped (cf. next subsection). This is illustrated in comparison with Schottky emission in Figure 2.6
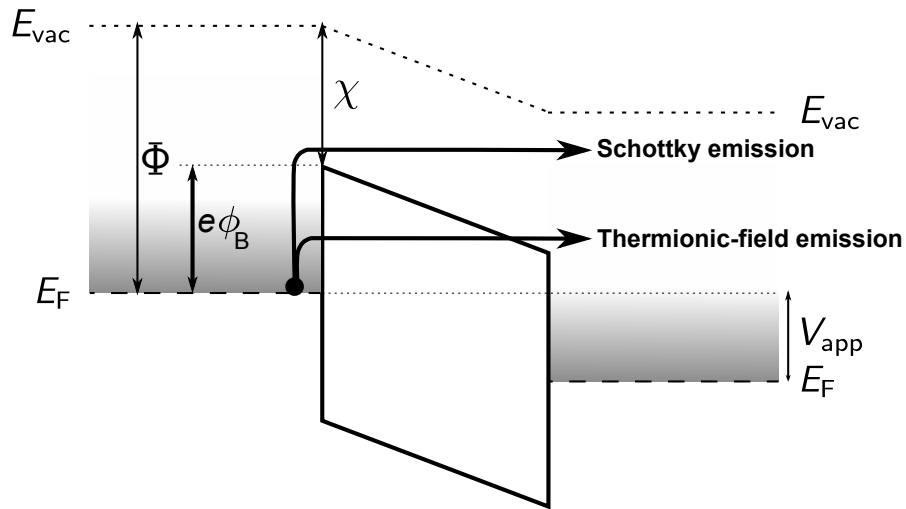
Figure 2.6.

Band diagram illustrating Schottky emission and thermionic-field emission.

2.3

Fowler-Nordheim (FN) Tunneling

In this section, Fowler-Nordheim (FN) tunneling will be discussed in detail. For a thin, defect-free dielectric layer direct tunneling and FN tunneling are the dominant mechanisms that cause leakage currents through the layer. When a voltage is applied to a dielectric layer its band structure is bent resulting in a triangular shaped barrier. Tunneling through this shorter triangular shaped barrier is called FN-tunneling and causes a tunneling current that is orders of magnitude larger than the current resulting from direct tunneling. Figure 2.7 illustrates how electrons tunnel via the FN mechanism.
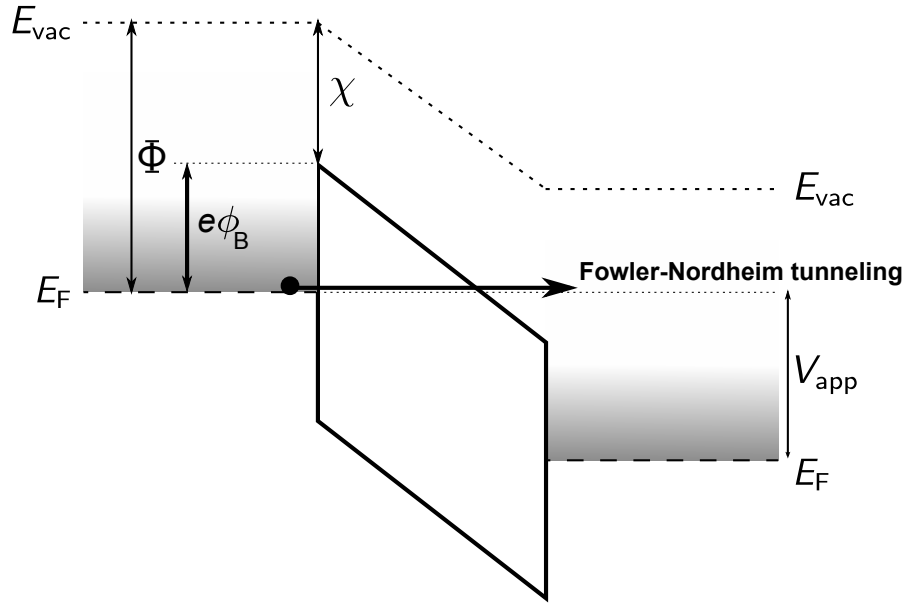
Figure 2.7.

Band diagram illustrating Fowler-Nordheim (FN) tunneling.

The FN tunneling current J_{FN} at an applied voltage V_{app} can be calculated by the Tsu-Esaki model[31, 32]:

$$J_{\mathrm{FN}}(V_{\mathrm{app}}) = \frac{4\pi \cdot m_{\mathrm{eff,Si}} \cdot e}{h^3} \int_{E_{\mathrm{C,Si}}}^{E_{\mathrm{C,Diel}}(0)} TC(E, V_{\mathrm{app}}) \cdot N(E, V_{\mathrm{app}}) \, \mathrm{d}E \qquad \textbf{[2.30]}$$

Where $m_{\mathrm{eff,Si}}$ is the electron effective mass in Silicon, $TC(E, V_{\mathrm{app}})$ is the transmission coefficient and $N(E, V_{\mathrm{app}})$ is the electron supply function.

For studying FN tunneling we will consider the following metal–insulator–semiconductor (MIS) architecture: The bottom electrode is highly p-doped Silicon on top of which there

is an ALD deposited dielectric layer/stack of layers. The top electrode is chosen to be a metallic material. From now on the index 'Si' will be used to denote the Silicon substrate, 'Diel' to refer to the dielectric layer(s) and 'Top' to label the top electrode. Furthermore, the index 'C' refers to the conduction band, 'F' to the Fermi-level and 'g' to the band gap. k_B is Boltzmann's constant, e is the elementary electric charge, h is Planck's constant, $\hbar = h/(2\pi)$ and T corresponds to the temperature ($= 300$ K).

The electron supply function $N(E, V_\mathrm{app})$ can be modeled by the ratio of Fermi-Dirac distributions on both sides of the dielectric and is a measure of how many electrons are available for tunneling:

$$N(E, V_\mathrm{app}) = k_\mathrm{B} \cdot T \cdot \ln \frac{1 + \exp\left(-\frac{E - E_\mathrm{F,Si}}{k_\mathrm{B} \cdot T}\right)}{1 + \exp\left(-\frac{E - E_\mathrm{F,Top} - e \cdot V_\mathrm{app}}{k_\mathrm{B} \cdot T}\right)} \qquad \textbf{[2.31]}$$

The transmission coefficient $TC(E, V_\mathrm{app})$ gives the probability for an electron to be transmitted through a barrier rather than reflected. This probability is a function of the energy E of the electron as well as the barrier height that is determined by the dielectric material and the applied voltage V_app. TC can be modeled by the Wentzel-Kramers-Brillouin (WKB) approximation:

$$TC(E, V_\mathrm{app}) = \exp\left(-\frac{2}{\hbar} \int_0^{x_\mathrm{C,Diel}(E, V_\mathrm{app})} \sqrt{2\, m_\mathrm{eff,Diel}\left(E_\mathrm{C,Diel}(x, V_\mathrm{app}) - E\right)}\; \mathrm{d}x\right) \quad \textbf{[2.32]}$$

where $m_\mathrm{eff,Diel}$ is the electron effective mass in the dielectric and $x_\mathrm{C,Diel}(E, V_\mathrm{app})$ is the distance (measured from the Silicon–dielectric interface) at which the conduction band edge of the dielectric is equal to E, the energy of the electrons. As $x_\mathrm{C,Diel}(E, V_\mathrm{app})$ has to be positive and not larger than the total thickness of the dielectric layer(s) it is given by the following formula:

$$x_\mathrm{C,Diel}(E, V_\mathrm{app}) = \begin{cases} 0 & \text{if } E > \chi_\mathrm{Si} - \chi_\mathrm{Diel} + (E_\mathrm{C,Si} - E_\mathrm{F,Si}) \\[2pt] d_\mathrm{Diel} & \begin{aligned}&\text{if } E < \chi_\mathrm{Si} - \chi_\mathrm{Diel} + (E_\mathrm{C,Si} - E_\mathrm{F,Si}) \\ &\qquad\qquad\qquad\quad - \Delta E_\mathrm{Diel}(V_\mathrm{app})\end{aligned} \\[10pt] \begin{aligned}&\frac{d_\mathrm{Diel}}{\Delta E_\mathrm{Diel}(V_\mathrm{app})}\Big(\chi_\mathrm{Si} - \chi_\mathrm{Diel} \\ &\quad + (E_\mathrm{C,Si} - E_\mathrm{F,Si}) - E\Big)\end{aligned} & \text{else} \end{cases}$$

$$\textbf{[2.33]}$$

$E_\mathrm{C,Diel}(x, V_\mathrm{app})$ is the conduction band position of the dielectric for an applied voltage V_app and for a fixed distance x away from the Silicon–dielectric interface, given by:

$$E_\mathrm{C,Diel}(x, V_\mathrm{app}) = \chi_\mathrm{Si} - \chi_\mathrm{Diel} - \frac{\Delta E_\mathrm{Diel}(V_\mathrm{app})}{d_\mathrm{Diel}}\, x + (E_\mathrm{C,Si} - E_\mathrm{F,Si}) \qquad \textbf{[2.34]}$$

In Equation 2.33 and 2.34, χ_{Si} and χ_{Diel} are the electron affinities of Silicon and the dielectric, respectively. d_{Diel} is the total thickness of the dielectric layer(s) and

$$\Delta E_{\text{Diel}}(V_{\text{app}}) = e \cdot V_{\text{app}} - e \cdot V_{\text{FB}} - 2k_{\text{B}} \cdot T \cdot \ln\left(\frac{N_A}{n_i}\right) \qquad \textbf{[2.35]}$$

The flat-band voltage V_{FB} is given by

$$e \cdot V_{\text{FB}} = \phi_{\text{Top}} - \chi_{\text{Si}} - (E_{\text{C,Si}} - E_{\text{F,Si}}) = \phi_{\text{Top}} - \chi_{\text{Si}} - \left(\frac{1}{2}E_{\text{g,Si}} + k_{\text{B}} \cdot T \cdot \ln\left(\frac{N_A}{n_i}\right)\right) \qquad \textbf{[2.36]}$$

where ϕ_{Top} is the work function of the top electrode, N_A is the Silicon doping level and n_i is the intrinsic carrier concentration of Silicon.

2.3.1 FN Simulations of Al$_2$O$_3$–BaTiO$_3$ Bilayers

The just discussed FN model is used to simulate the leakage currents of BaTiO$_3$ in the following architecture: p–doped Silicon substrate is used as bottom electrode. The dielectric layers are a thin layer of Al$_2$O$_3$ and a high–k layer of BaTiO$_3$ on top of one another. The top electrode is Aluminum. The band structure is illustrated in Figure 2.8. The left diagram shows the band structure when no voltage is applied having a flatband-voltage (indicated with a red circle) due to the fact that the top electrode has a different work function than the Silicon bottom electrode. The right diagram shows the same structure at an applied external bias.
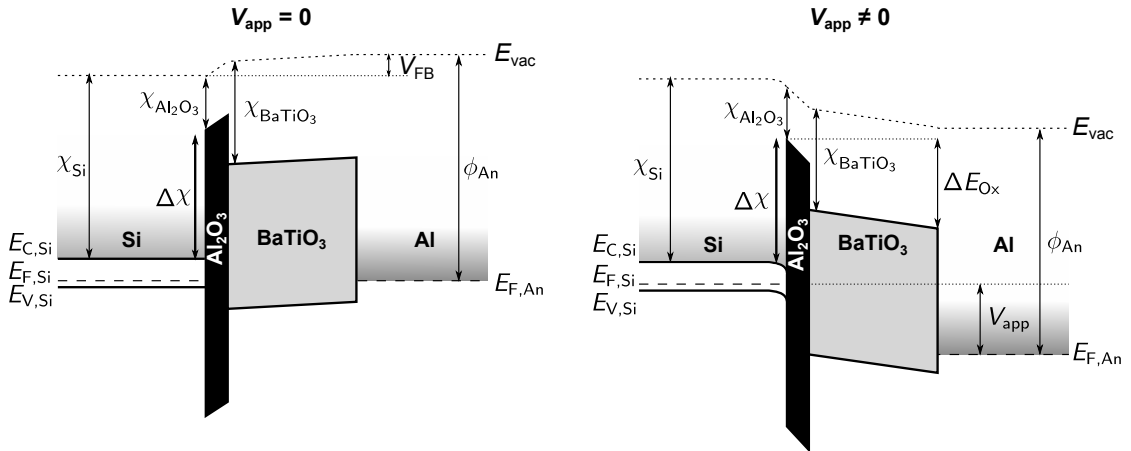
Figure 2.8.

Band structure of the device architecture that is used for FN-simulations is shown. Left and right diagram corresponds to the structure when no voltage is applied and when a positive voltage is applied, respectively.

Figure 2.9 shows the calculated tunneling currents for the before mentioned device structure using: a) a 10 nm thick BTO layer, b) a 2 nm thick Alumina layer and c) a

combination/stack of both a 2 nm Alumina layer and a 10 nm BTO layer. The values that were used for the calculation are listed in Table 2.1. This simulation clearly shows that the Alumina blocking layer decreases the leakage current by several orders of magnitude and agrees well with the experimental results we will discuss in the experimental section. Furthermore, at a thickness of 10 nm for BTO and 2 nm for Alumina the leakage current is mainly dominated by the leakage current through the Alumina layer.

Figure 2.10 shows the same device architecture but with the thickness of BTO being 5 nm comparing two different thicknesses for Alumina: 1 nm and 1.5 nm. Even a small difference of 0.5 nm in thickness for the blocking layer changes the resulting leakage current significantly due to the exponential decay of quantum mechanical tunneling with increasing thickness. Also, it is important to note that for thinner Alumina blocking layers the tunneling currents are not dominated by the Alumina layer but rather are influenced by the BTO dielectric itself.

Not only the thickness of the dielectric can largely decrease the magnitude of the leakage currents but also the electron affinity of the dielectric layer is a fundamental parameter when it comes to FN tunneling behavior. This is illustrated in Figure 2.11 where the leakage currents are calculated for a 10 nm thick BTO layer having different electron affinities $\chi_{\mathrm{BaTiO_3}}$ of 3.78 eV and 3.48 eV. This shows that a small difference of 0.3 eV in electron affinity can reduce the leakage current by several orders of magnitude and that without using any blocking layer. Doping might be a possible technique to facilitate this change in band structure and electron affinity as will be observed in the experimental section of this thesis.

Parameter	Symbol	Value	Ref.
Electron affinity of Silicon	χ_{Si}	4.05 eV	[33]
Band gap of Silicon	$E_{\mathrm{g,Si}}$	1.12 eV	[33]
Doping level of Silicon	N_A	10^{19} cm^{-3}	[10]
Intrinsic carrier concentration of Silicon	n_i	10^{10}	[33]
Electron effective mass of Silicon	$m_{\mathrm{eff,Si}}$	$0.26 \cdot m_0$	[33]
Electron affinity of Alumina	$\chi_{\mathrm{Al_2O_3}}$	1.0 eV	[34]
Electron effective mass of Alumina	$m_{\mathrm{eff,Al_2O_3}}$	$0.28 \cdot m_0$	[35]
Electron affinity of BTO (cubic)	$\chi_{\mathrm{BaTiO_3}}$	3.76 eV	[36]
Electron effective mass of BTO (cubic)	$m_{\mathrm{eff,BaTiO_3}}$	$6.5 \cdot m_0$	[37]
Electrode work function of Aluminum	ϕ_{Al}	4.08 eV	[38]

Table 2.1.

List of parameters that were used for FN tunneling calculations.
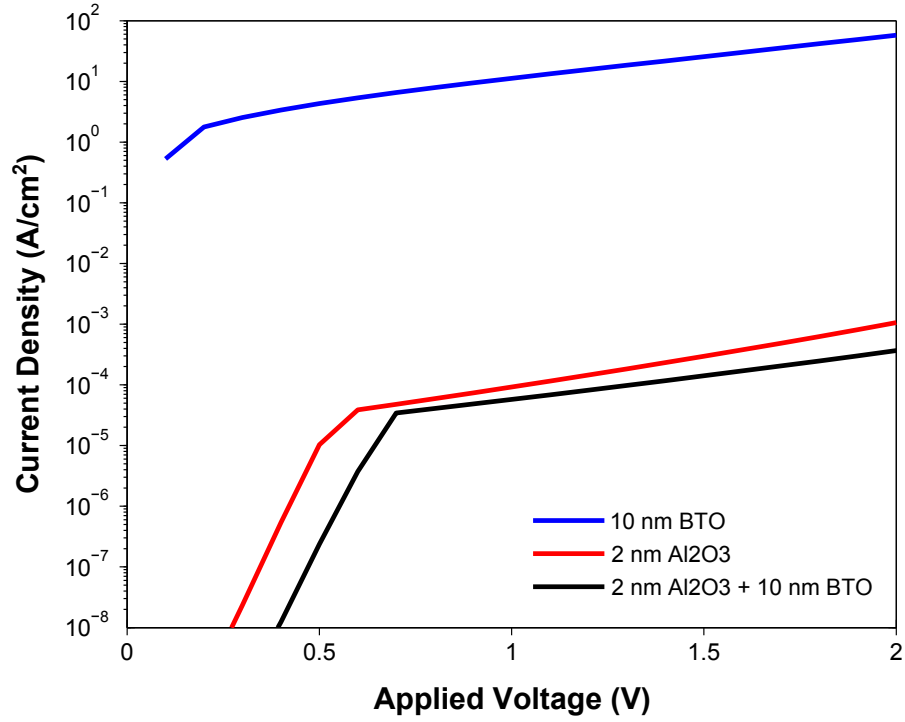
Figure 2.9.

FN tunneling currents as a function of applied voltage are plotted. Different dielectric layers are used for each calculation. A 2 nm thick Alumina layer, a 10 nm thick BTO layer and a stack of both 2 nm thick Alumina and 10 nm thick BTO.
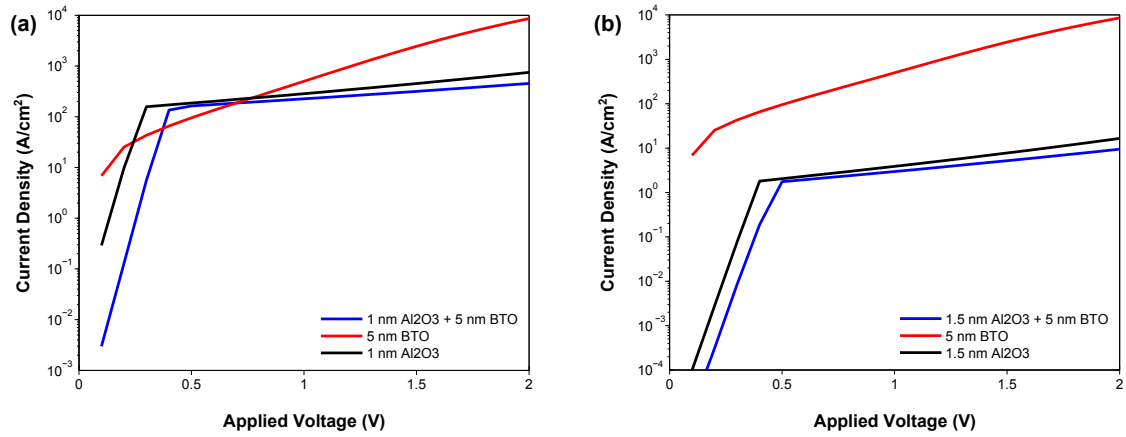
Figure 2.10.

FN tunneling currents as a function of applied voltage are plotted. For the calculation a 5 nm thick BTO layer is used. On the left and right hand side plot a 1 nm and 1.5 nm thick Alumina layer is used, respectively.
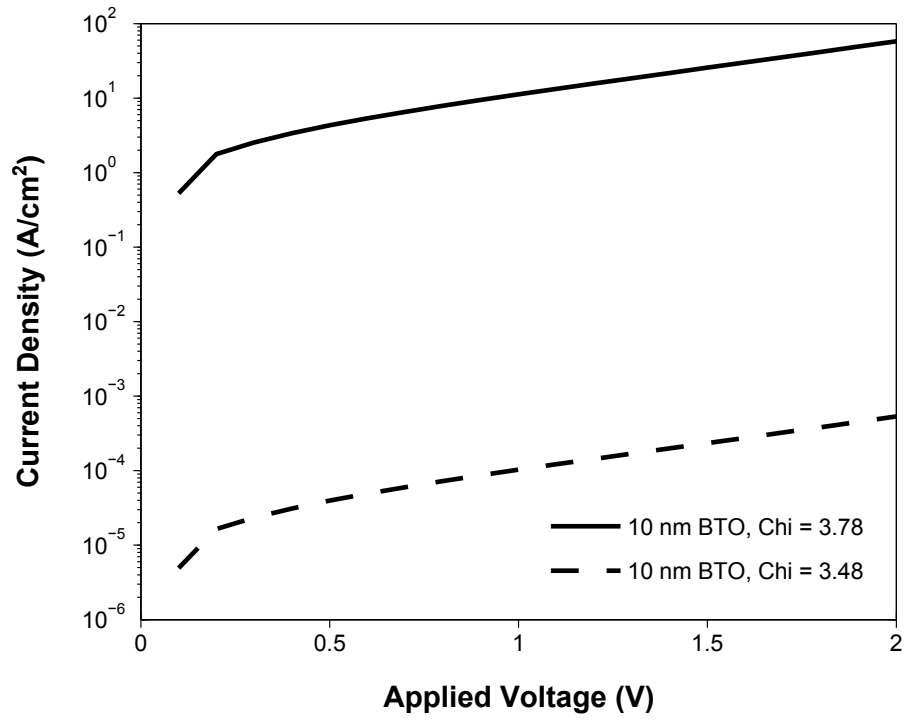
Figure 2.11.

FN tunneling currents as a function of applied voltage are plotted. A comparison between BTO layers of different electron affinities is shown.

2.4

Defect Induced Mechanisms

In the previous mechanisms the electron energy with respect to the metal electrode was of importance (i.e. temperature and applied field) for tunneling/conducting through a dielectric film. These mechanism did not consider any defects in the dielectric film and assumed an ideal dielectric film with an undisturbed band structure. In this section, defect induced tunneling and conducting mechanisms will be discussed in more detail.

In trap-assisted tunneling (TAT) electrons can tunnel in a two step process first to a trap site, that has a much lower energy than the conduction band position of the dielectric (a so-called deep trap) and in a second step tunnel from the trap to the top electrode. This is illustrated in Figure 2.13(a). There are several models (several of them discussed in [32]) that can be used for this mechanism, one of them models the current as[39]

$$J_{\text{TAT}} = e \int_0^{d_{\text{diel}}} A \cdot n_{\text{T}}(x) \frac{P_c(x)P_e(x)}{P_c(x) + P_e(x)} \mathrm{d}\,x \qquad [2.37]$$

where A is a fitting parameter, $n_{\text{T}}(x)$ is the spatial trap concentration and $P_c(x)$, $P_e(x)$ are the probabilities of electrons being captured or emitted by traps, respectively. It further should be noted that there is elastic and inelastic TAT where in the latter one the electrons captured by a trap can relax through phonon interactions. Also, if the trap density is high enough can result in the Fermi level being pinned to the trap energy level at the interface.[40] The trapped charges may also influence the electric field distribution within the dielectric layer.[41]

The Poole-Frenkel (PF) mechanism is comparable to the Schottky emission as it is based on electrons being thermally excited from a trap site inside the dielectric into the conduction band. This process can further be facilitated by an externally applied field making it easier for the electron to be elevated into the conduction band. Figure 2.13(b) illustrates the band diagram and the path of the electrons. The current density can be modeled as follows[42]

$$J_{\text{PF}}(E, T) = e\mu n_{\text{C}} E \cdot \exp \left[\frac{-e(\phi_{\text{T}} - \sqrt{eE/(\pi\epsilon_r\epsilon_0)})}{k_{\text{B}}T} \right] \qquad [2.38]$$

where μ is the electron drift mobility, n_{C} is the density of states in the conduction band and $e\phi_{\text{T}}$ is the energy level of the traps. This mechanism is commonly observed in the case of high temperatures and high fields.

The hopping conduction mechanism is caused by electrons tunneling from one trap to the next. This is similar to TAT, just that it is a sequence of tunneling as well as the traps tend to form a band below the conduction band (usually higher than deep traps).

Figure 2.13(c) illustrates the band diagram for the hopping mechanism. The current density caused by hopping conduction is given by[42]

$$J_{\mathrm{H}}(E,T) = ean_{\mathrm{C}}\nu \cdot \exp\left[\frac{e(aE - \phi_T)}{k_{\mathrm{B}}T}\right]$$

[2.39]

where a is the mean distance between traps and ν is the frequency of thermal vibration of electrons at the traps. This mechanism can still occur at lower temperatures when PF mechanism would not have enough thermionic energy to lift electrons up into the conduction band.

Additionally to these three main defect-assisted mechanism there are a few other ones that should be mentioned here:

During ionic conduction ions can move through the dielectric by means of an applied field from one trap/vacancy to another. As the mass of the ions are large compared to the electrons, this effect can mostly be neglected for thin dielectric films.

Grain boundaries can largely effect the behavior of tunneling currents through a (poly-crystalline) dielectric film. Unlike for quantum mechanical tunneling of electrons, here electrons can be localized at the grain boundaries (similar to TAT) which then act as percolation path through the layer (cf. Figure 2.12). This may largely increase leakage currents through a dielectric. However, if the resistivity of the grain boundaries is much larger than the one of the grains, this can also reduce/limit the conduction through a polycrystalline film.
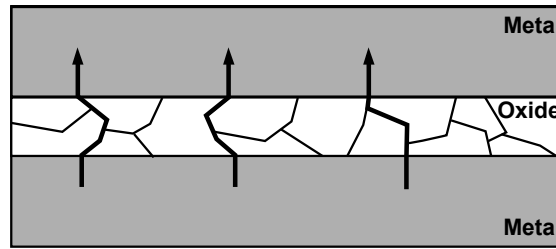
Figure 2.12.

Illustration on how grain boundaries can act as percolation paths for leakage currents in an MIM structure.

There are a few other mechanism that are not discussed here such as impact ioniza-tion,[43] hot carrier tunneling,[44] ohmic and space charge limited conduction.[42]

(a)

E_{vac}

χ

E_{vac}

Φ

$e\phi_B$

Trap-assisted tunneling

E_F

V_{app}

E_F

(b)

E_{vac}

χ

E_{vac}

Φ

$e\phi_B$ $e\phi_T$

Poole-Frenkel Emission

E_F

V_{app}

E_F

(c)

E_{vac}

χ

E_{vac}

Φ

$e\phi_B$ $e\phi_T$

Hopping conduction

E_F

a

V_{app}

E_F
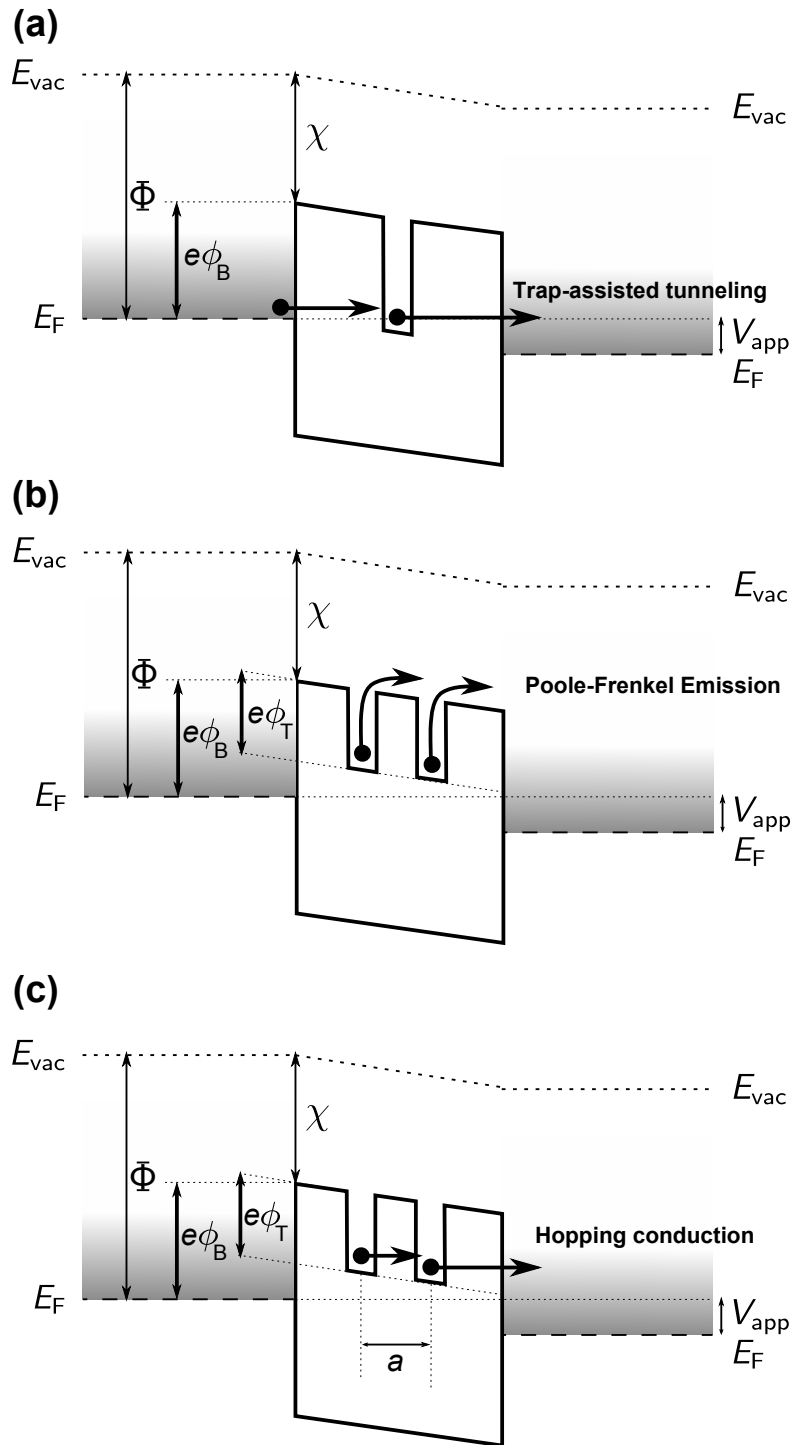
Figure 2.13.

Band diagrams illustrating (a) Trap-assisted tunneling (TAT) via deep traps, (b) Poole-Frenkel (PF) emission and (c) hopping conduction.

<div style="text-align: right">

CHAPTER **III**

</div>

Experimental Procedure

Contents

┌─ **1**
│   **Deposition Techniques**
└───

1.1 ───

Atomic Layer Deposition (ALD)

Thin film deposition has become of great importance in the semiconductor industry as device scaling progresses deep into the nm regime. While there is a wide selection of thin film deposition techniques such as chemical vapor deposition (CVD), chemical beam epitaxy (CBE), ion beam deposition (IBD), molecular beam epitaxy (MBE) and physical vapor deposition (PVD), atomic layer deposition (ALD) will be the key enabling technique in this thesis.

ALD is a form of CVD in which the chemical reaction is split up into two (or more) self-limiting surface reactions. Unlike in CVD where there is a continuous flow of precursors, in ALD the precursors are introduced sequentially until (due to the self-limiting nature) saturation of the precursor reaction with the surface has occurred and the by-products and remaining precursors are purged out. These (gaseous) precursor pulses separated by purges comprise a so-called ALD cycle that generally is separated into half-cycles: The precursor (typically a metal halide or metal organic compound) half-cycle and the oxidation/nitration/sulfation (oxygen, water, nitrogen, NH_3, H_2S,...) half-cycle.

Figure 3.1 illustrates one ALD cycle of trimethylaluminum (TMA, $Al(CH_3)_3$) and water, oxygen plasma or ozone to form a monolayer of Al_2O_3. In the case of water as a co-reactant (often referred to as **thermal ALD**) the following two half-steps occur separated by two reaction chamber purges:

[1.] TMA is pulsed into the reaction chamber. One of the methyl (CH_3) ligands reacts with the hydroxyl (O–H) group at the surface in a self-limiting fashion. This occurs until the surface is saturated (or sites are unaccessible due to steric shielding or geometric constraints).

$$Al–O–H + Al(CH_3)_3 \rightarrow Al–O–Al(CH_3)_2 + CH_4$$
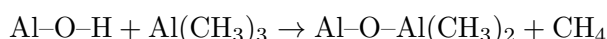
[2.] The by-products (CH_4) and unreacted precursors are purged out of the chamber.

[3.] Water is pulsed into the reaction chamber. The remaining methyl ligands can react with water to form Al_2O_3 and CH_4.

$$Al–CH_3 + H_2O \rightarrow Al–O–H + CH_4$$
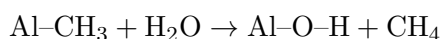
[4.] The by-product (methane) and remaining H_2O are pumped out of the chamber.

This sequence forms one ALD cycle to produce a monolayer of Al_2O_3. By repeating this sequence the number of atomic layers deposited by ALD can be controlled.
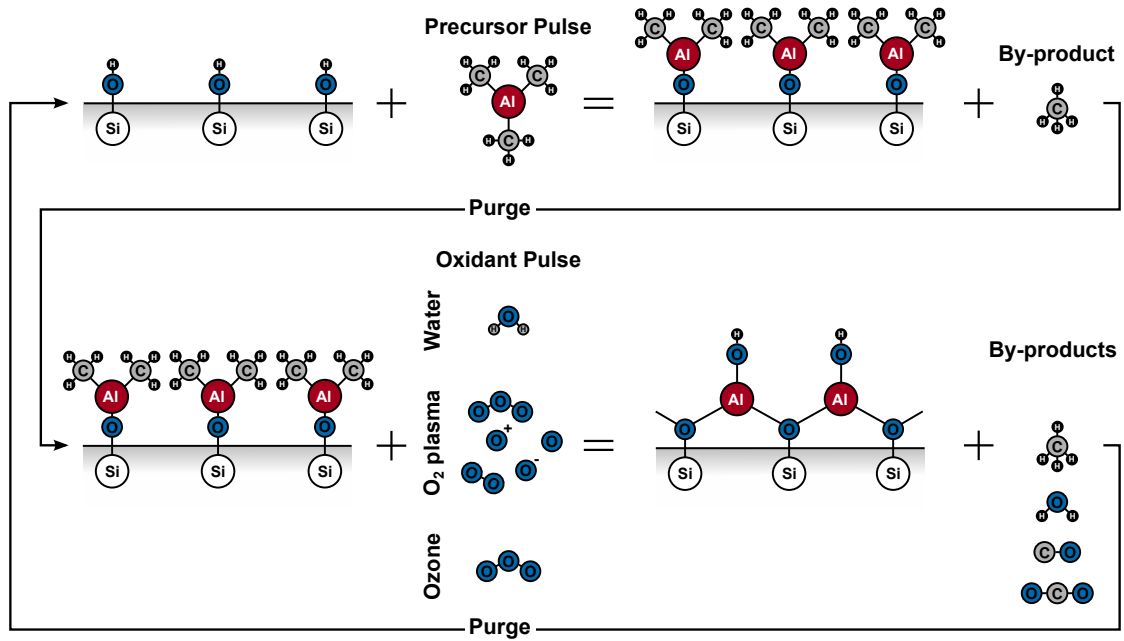
Figure 3.1.

ALD process of a Al_2O_3 is illustrated. TMA is used as a precursor in the first half-cycle. Water, ozone or O_2 plasma is used for the second half-cycle.

Due to the self-limiting nature of ALD it is known to have precise thickness control down to the sub-nanometer range as well as the ability to deposit films conformally over complex high AR 3D structures.[45] There is a range of advantages that ALD has over other thin film deposition techniques:

- The films are very continuous and pinhole-free which is crucial for thin dielectric films.

- Also films produced with ALD are extremely smooth and conformal.

- ALD can be used on very large substrates and is only limited to the size of the reaction chamber.

- Due to sequential application of the precursors the reactants are not in contact in the gas phase (unlike CVD) and therefore cannot react with each other.

- ALD operates at rather low temperatures (typically below 500 °C) which results in a small diffusion length and hence inhibits intermixing of deposited films.

- ALD is much cheaper compared to other thin film techniques (e.g. MBE).

1.1.1 **Surface Chemistry in ALD**

The self-terminating nature of ALD is strongly depending on the surface chemistry and thus needs to be discussed in detail. The adsorption of the precursor molecules on the surface can be divided into two processes called physi- and chemi-sorption. Physisorption causes minimal changes in the adsorbed precursor and its process is not dependent on the chemistry of the surface or the precursor itself. Therefore, multiple layers can be physisorped at once, rendering this process unsuitable for ALD. Chemisorption on the other hand changes chemical bonds during the adsorption process and hence may limit the chemisorption of another precursor molecule on the same surface site. Hence, ALD is limited to chemisorption that is self-limiting with its chemisorbed species stable enough to not desorp from the surface during purging.
There these types of chemisorption mechanisms[46] are illustrated in figure 3.2:

- **Ligand exchange:** (Figure 3.2 (a))
  The reactant is split on the surface and the ligand combines with a surface group to form a gaseous reaction by-product. This can also occur for more than one ligand (second reaction in figure 3.2 (a)). This process consumes additional surface groups but does not bond more metal to the surface.

- **Dissociation:** (Figure 3.2 (b))
  The reactant is split onto two or more reactive sites on the surface without producing a gaseous by-product.

- **Association:** (Figure 3.2 (c))
  The reactant forms a coordinative bond with a reactive surface site and is desorbed without releasing by-products/ligands.
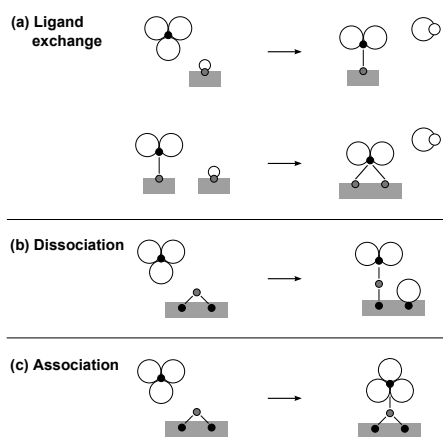
Figure 3.2.

Schematic view of chemisorption mechanisms in ALD. Big white circles are ligands, small black circles metals, small white circles are surface sites which are able to react with the ligands, small gray cycles are surface sites which are able to react with metals. Adapted from **[46]**.

1.1.2 Growth Per Cycle (GPC) and the ALD Window

A key parameter for checking whether or not the chemical reaction is in a self-limiting regime or not is the growth per cycle (GPC). Unlike in CVD where a growth rate (unit: inverse time) is stated, GPC is more useful for ALD due to the cycle based fashion it operates in. GPC is typically in the range of low fractions of an Å to less than 2–3 Å. When experimentally testing if the process is in the self-limiting regime two parameters are studied and their effect on the GPC: The precursor dosing time and the purging time. If the reaction is self-limiting the GPC has to saturate with increasing precursor dosing time as shown in Figure 3.4(a). Additionally, if the purging time is chosen too short, remaining unreacted precursor molecules in the reaction chamber may react with the second precursor (e.g. the oxidant) in the gas-phase and increase the GPC beyond its saturation point. Hence, increasing the purge time (cf. Figure 3.4(b)) should ensure a saturation at the same GPC as the precursor dose saturated value.
Temperature is another important parameter that determines self-limiting behavior. The "ALD window" is the range of temperatures in which the reaction is self-limiting and therefore is in the ALD regime.[45] For lower temperatures than the ALD window, the reactions may lack of thermal energy (reduced GPC) or the reactants could condense on the surface (increased GPC). At temperatures that are too high, surface species could desorp from the surface (and thus be unavailable for further surface reactions) resulting in a reduced GPC, or they could decompose and allow additional reactant adsorption resulting in an increased GPC. The GPC as a function of temperature is schematically plotted in Figure 3.4(c). Classically the GPC stays constant within the ALD window, however the GPC can increase/decrease due to a variation in film density, concentration of surface groups or composition as indicated by dashed lines in Figure 3.4(c).[47]
Additionally, the GPC can change as the number of cycles increases. This is the case if there are differences in the surface chemistry between substrate and ALD grown material. For substrate-enhanced growth the GPC is higher for the first couple of cycles due to the substrate surface sites being more reactive than the ones of the ALD produced material. Conversely, for substrate-inhibited growth the GPC is lower for the first few cycles.
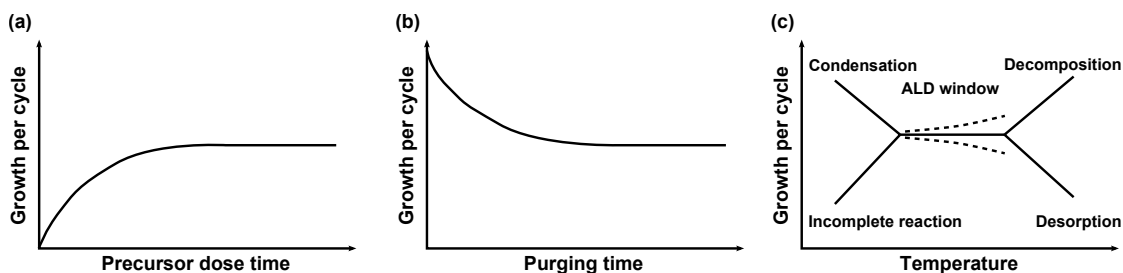
Figure 3.3.

(a) Growth per cycle (GPC) as a function of precursor dosing time showing saturation. (b) GPC as a function of purging time showing an increased GPC for too short purging times. (c) GPC versus temperature indicating the "ALD window". Dashed lines represent variations in GPC within the ALD window.[47]

1.1.3 Growth Types for ALD

Ideal two-dimensional growth (i.e. layer by layer) takes place in idealized ALD due to the self-limiting nature of the reactions. But due to steric hindrance of the ligands (available reactive surface sites are blocked by chemisorped precursor molecules) and limited number of available surface sites, growth of less than a monolayer per cycle can occur. For growth of less than a monolayer per cycle different growth processes are occurring which are schematically illustrated in Figure 3.4.[46]

These are the following growth types for ALD with less than a monolayer per cycle growth:

- **Two-dimensional growth:**
  Deposited material prefers to adsorb in the lowest unfilled layer.

- **Island growth:**
  Precursors preferentially deposit on already ALD-grown material. This growth type is commonly observed for ALD.

- **Random deposition:**
  New material deposits randomly on all available surface sites. Due to the self-limiting nature this results in a smoother layer than in continuous deposition processes like CVD.

The growth type can vary between the first few layers and the layers deposited thereafter. This strongly depends on the efficiency of the reaction of the precursors with the initial substrate. Often island growth could be dominant at first and these islands tend to grow together forming a continuous film. Ultra-thin films for a non-ideal ALD process are most likely rough and not conformal to the initial substrate.
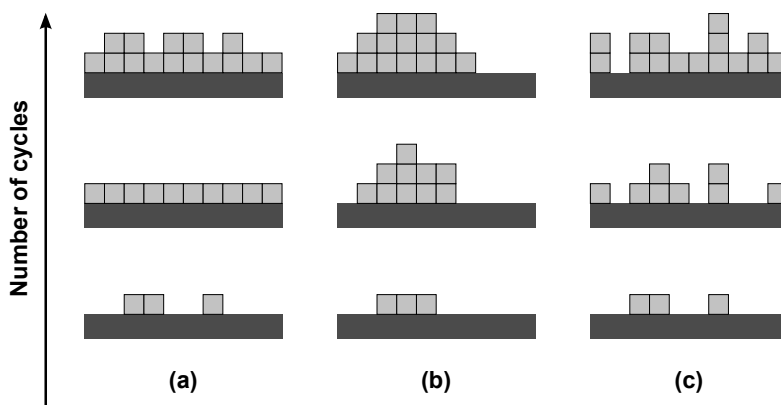
Figure 3.4.

Different growth processes schematically illustrated with increasing number of cycles. (a) two-dimensional growth, (b) island growth and (c) random deposition. Adapted from **[46]**.

1.2

Plasma-Enhanced Atomic Layer Deposition (PEALD)

Plasma enhanced ALD (PEALD) is a modification of ALD that facilitates plasma (e.g. O_2, N_2, Ar, H) as the second reactant to strip off the remaining ligands at the surface in contrast to using a gas (e.g. water vapor, ozone or NO_2). PEALD is part of energy-enhanced ALD in which energy is supplied in situ to convert a traditional thermal ALD co-reactant (e.g. O_2, N_2, etc.) into a highly reactive species with a short-term stability.[47] Other examples for energy-enhanced ALD are UV-assisted ALD and ALD using ozone or nitrogen oxide generated in an ozone generator. The additional energy and highly reactive species such as radicals, ions, electrons and high energy photons can facilitate the ALD reaction at a lower thermal budget.

Depositing Al_2O_3 by PEALD instead of thermal ALD using TMA, facilitates an O_2 plasma instead of water in the second half-step as depicted in Figure 3.1. The excited oxygen species O^* reacts with the methyl ligand forming methane and carbon dioxide as by-products: (Note that there is also a combustion-like reaction occurring forming CO and H_2O)

$$2\,[\text{Al–CH}_3] + 4\text{O}^* \rightarrow 2\,[\text{Al–O–H}] + \text{CH}_4 + \text{CO}_2$$

PEALD has advantages over conventional thermal ALD processing including lowering of process temperature (hence minimizing the thermal damage during device fabrication), improving film quality (density, electrical properties and roughness) and enabling deposition of new materials with a wider selection of precursors.[47, 48] Due to the wider space of parameters that can be used in PEALD (plasma power, pressure, exposure time) film properties and stoichiometry can be tuned. Also, in conventional thermal ALD water vapor usually takes longer purging times as it tends to stick to the reactor side-walls, whereas plasmas require only a very short time for purging.

1.2.1 Coverage of High AR Surfaces by PEALD

While for thermal ALD conformal coverage of 3D structures is considered to be one of its biggest advantages and has been shown to be feasible for an AR of 1:200,[49] PEALD is often thought to have a disadvantage because excited plasma species tend to recombine on sidewalls in narrow trenches.[50, 51] In literature, a conformal coverage of 3D structures for SiO_2 and HfO_2 up to an AR of 1:60 has been shown for PEALD films.[52] While in the experimental part of my thesis the conformal coverage of PEALD TiO_2 will be studied in detail, here I want to review two papers from literature studying PEALD in terms of high AR coverage.

The first paper that will be discussed here is an experimental work studying the conformality of Al_2O_3 and AlN deposited by PEALD by Dendooven et.al.:[53] Unlike many other approaches studying high AR coverage (based on micro/nanoscopic substrates), in this work a *macroscopic* rectangular shaped hole is masked (by cutting out a rectangle of poly–tetrafluoroethylene film that is clipped) onto a Si substrate and is studied in terms

of penetration depth of a deposited PEALD film into that macroscopic hole (as illustrated in Figure 3.5(a)). The big advantage of this method is that sample preparation for post-characterization is not required and hence many different plasma conditions can be studied very seamlessly and requires only ellipsometry for measuring the thickness of the deposited film as a function of penetration depth into the macroscopic hole. Also, the AR can simply be changed by changing the dimensions of the cut-out hole (thickness of film that is used for masking, or width of the rectangular hole).

First, they studied the difference between ALD and PEALD in terms of conformality of different ARs as seen in Figure 3.5(b)&(c), respectively. As expected, ALD shows a higher penetration depth than PEALD at the same AR. In a next step, they studied different plasma conditions during PEALD and how they affect the penetration depth/conformality. The parameters that were studied were RF plasma power, pressure and plasma exposure time as shown in the plots in Figure 3.5(d)–(f), respectively. Changing the plasma RF power from 50 W to 150 W showed a large improvement, whereas changing it from 150 W to 350 W barely showed any further improvement suggesting that the effect is saturating/leveling off. In terms of the pressure during the plasma step, minor improvements in the penetration depth were observed with increasing pressure. A continuous and fairly significant improvement is seen with increasing the plasma exposure time per cycle, although this was not studied beyond a 18 s exposure time and may improve the AR coverage even more thereafter (as will be studied for PEALD TiO_2 in the experimental part of this thesis).
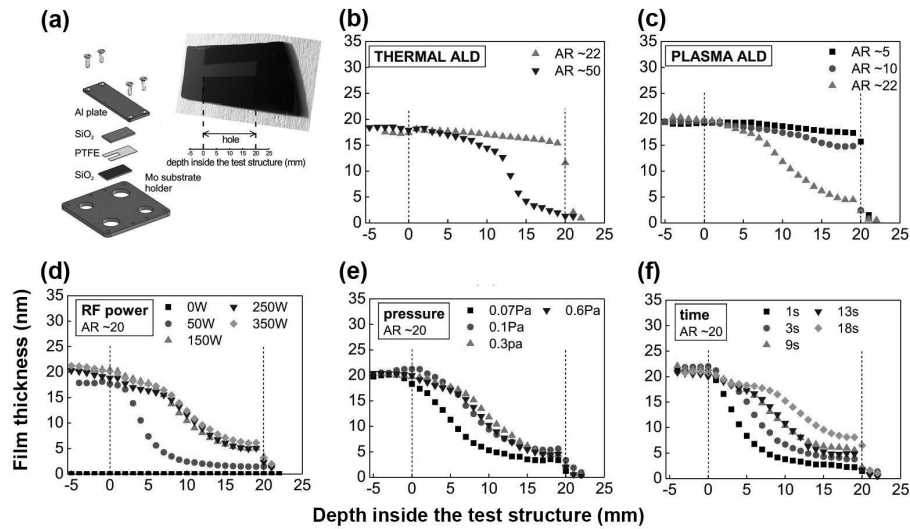

Figure 3.5.
(a) Illustration of geometry used for masking a macroscopic hole with defined AR. (b)&(c) Measured film thickness as a function of penetration depth comparing ALD and PEALD for different ARs, respectively. (d)–(f) Effect of plasma power, pressure and plasma exposure time is studied by plotting film thickness with penetration depth, respectively. Adapted from **[53]**.

The second paper that will be discussed here is a simulation-based work by Knoops et.al. studying the conformality of PEALD in general:[54] Their simulation approach is based on a simple but powerful Monte-Carlo calculation in which only two parameters are used, the recombination probability r and the reaction/sticking probability s. The first one (r) is a parameter representing surface reactions where the incoming reactant species changes in such a way that it cannot contribute to the ALD process anymore. The latter one (s) can be viewed as the probability that a surface reaction does contribute to the ALD process. The simulations process goes through the following steps: A two-dimensional rectangular trench is assumed comprised of entrance, side-walls and bottom (each being segmented into intervals). A particle is generated at the entrance with a random direction — the impact point with a side-wall/bottom is calculated for this particle (if the direction was chosen so it would go outside of the entrance, a new particle is generated instead). For this interval at the side-wall/bottom a random number between 0 and 1 is generated and if this number is smaller than r the particle recombines and does not contribute to the reaction (hence a new particle will be generated at the entrance). But if the random number was lager (or equal) r and if this interval was not occupied by another particle previously, another random number is generated and compared with the parameter s. If this random number is larger or equal to s or the interval was already occupied, the particle gets reflected at a random direction and the previous steps are repeated. If the random number was smaller than s the particle sticks to that interval and therefore contributes to the ALD reaction.

The simplicity of this model is to note, as it is 2–dimensional and does not consider any influences on the chemistry of the reactions (such as temperature and particle velocities), instead these influences can be studied by their effect on the parameters r and s. Nevertheless, this model gives insight into the different regimes that limit the conformal coverage of an high AR trench.

Figure 3.6(a) shows the absolute saturation dose (absolute number of particles generated to achieve a saturation of the intervals of the side-walls/bottom) as a function of AR and sticking probability s for the case $r = 0$, that being more representative for thermal ALD (no unstable radicals present). Here, two limiting regimes can be identified: The *Reaction-limited* regime, where $s \ll 1$ and the required dose for saturation is independent of the AR. And the *Diffusion-limited* regime, where AR is high and the required dose does not depend on the value of s. The normalized saturation dose (normalized to the dose required for saturating a trench with AR of 1) as a function of the AR for different r ($r > 0$ being representative for PEALD) and s values is plotted in Figure 3.6(b). For this case, a new regime can be identified: The *recombination-limited* regime, where r is non-zero and the dose does not anymore depend on the sticking probability s.

For these three identified regimes, the deposition profiles are illustrated at the top of Figure 3.7(a)–(c), respectively. The plots at the bottom are showing the normalized number of wall collisions (normalized to the total number of particles needed for achieving saturation) as a function of depth into the trench for representative values for r and s for the three limiting regimes. Figure 3.7(a) compares the first and last 10^6 particles for the reaction-limited case. In (b) the wall collision profiles of $6 \cdot 10^5$ particles in steps

46

of 10^5 are compared for the diffusion-limited case. And lastly in (c) the first and last 10^7 particles are compared for the recombination-limited case.

These plots show that in the reaction-limited regime growth occurs simultaneously throughout the trench, in the diffusion-limited regime a moving deposition front is observed and in the recombination-limited regime growth occurs throughout the trench but with a reduced rate near the bottom.
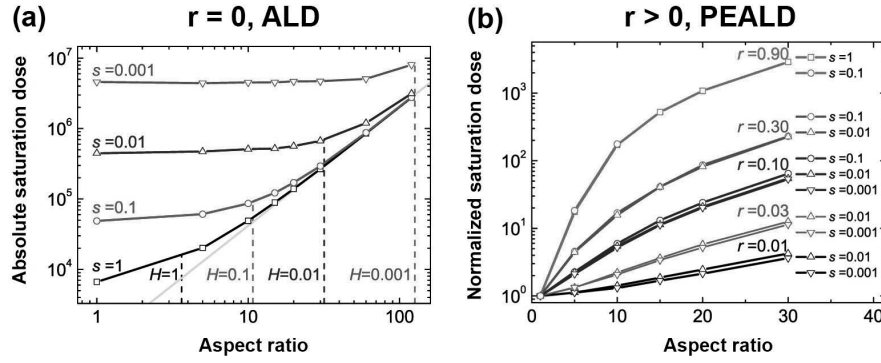
Figure 3.6.

(a) Case of $r = 0$ (representing thermal ALD). Absolute saturation dose as a function of AR and sticking probability s is plotted. (b) Case of $r > 0$ (representing PEALD). Normalized saturation dose plotted as a function of AR, s and r. Adapted from **[54]**.
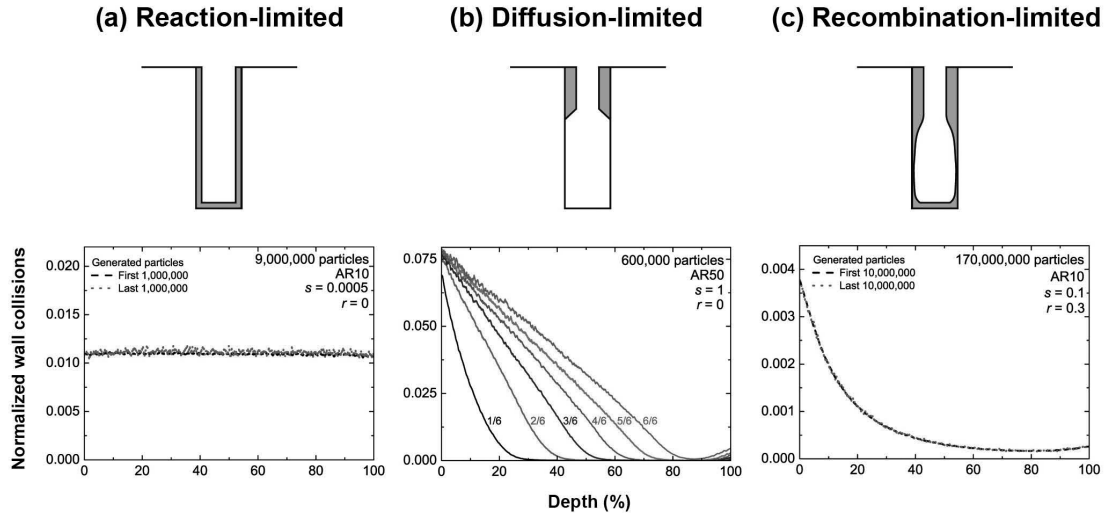
Figure 3.7.

Normalized wall collisions are plotted as a function of depth into the trench for the three limiting regimes. Comparison of (a) first and last 10^6 particles for the reaction-limited regime (AR= 10, $s = 0.0005$, $r = 0$), (b) $6 \cdot 10^5$ particles in steps of 10^5 for the diffusion-limited regime (AR= 50, $s = 1$, $r = 0$) and (c) first and last 10^7 particles for the recombination-limited regime (AR= 10, $s = 0.1$, $r = 0.3$). Adapted from **[54]**.

2

Material Characterization by High Energy Photons (X-Rays)

2.1

X-Ray Photo-Electron Spectroscopy (XPS)

One of the most commonly used techniques for obtaining surface sensitive information about the chemical composition is X-ray photo-electron spectroscopy (XPS). Additionally, chemical state (e.g. oxidation state and local binding) and electronic state information can be extracted from peak fitting models. The experimental setup of XPS is illustrated in Figure 3.8(a): An X-ray beam is generated (typically 1.5 keV) and focused onto a sample surface. This process of high energy photons radiated onto a sample can knock out electrons from the core (leaving core holes) hence emitting photo-electrons (illustrated in Figure 3.8(b)) that are measured by a kinetic electron energy analyzer at a defined angle. Additionally, at the end of the energy analyzer there is an electron detector counting electrons. XP spectra are plots of electron counts as a function of electron energy. The fact that electrons penetrate only about 10 nm of a solid material makes XPS a very surface sensitive technique. Also, this requires the experimental setup to be carried out in ultra-high vacuum.

XPS, in principle, can detect any element with an atomic number of 3 (Lithium) or heavier and usually gives a concentration detection limit of ~ 0.1 at%. However, this accuracy strongly depends on the element and overall concentration in the sample.

Most modern XPS system have a sputtering gun (e.g. Ar^+ ions) to enable depth profiling of a sample. This is especially useful when dealing with thin films. Additionally, for analyzing thin films, electrons from different depths can be detected by angle-resolved XPS (ARXPS). In this technique the emission angle at which the electrons are collected is changed providing information about the thickness and composition of ultra-thin films.
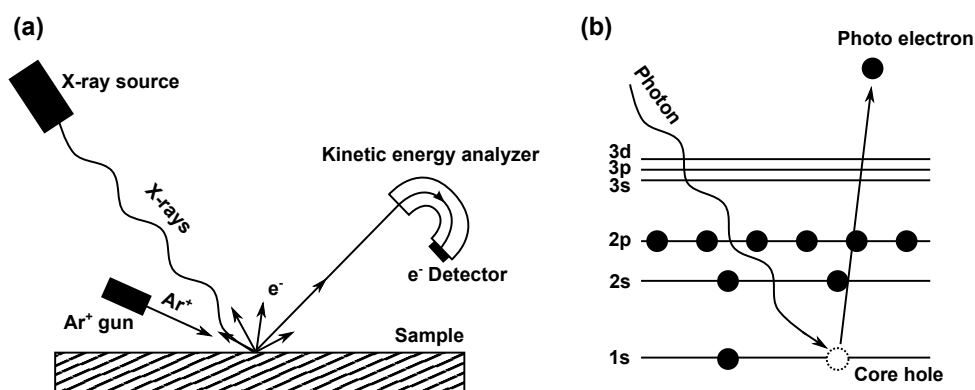
Figure 3.8.

(a) Experimental setup of XPS is shown schematically. (b) Illustration of high energy photon exciting a core electron that can be measured by the kinetic energy analyzer.

2.2

X-Ray Diffraction (XRD)

Here a short summary will be given on X-ray diffraction (XRD) that is the most common technique to investigate the structure of materials. The experimental setup consists of the X-ray source, a sample stage and an X-ray detector. Usually X-rays are generated by heating a filament to produce electrons that then are accelerated by an applied voltage to bombard a target material. If these electrons have sufficiently high energy they can move inner shell electrons that in turn generate characteristic X-ray spectra. The most commonly used target material is Cu producing Kα ($\lambda = 0.154$ nm) radiation. As this wave length is comparable to atomic distances in a periodic lattice it is suitable for investigating crystalline structures. For this purpose Figure 3.9 illustrates diffraction on a periodic lattice with distance d between atomic planes. The incident wave comes at an angle θ with respect to the sample and has a wave length λ. The incident wave is scattered by the atoms and if the scattered wave at each atomic plane stays in phase, constructive interference occurs. They stay in phase if the path length of each scattered wave is an integer multiple of the wavelength. Looking at the geometry of incident and diffracted beam as well as the spacing between atoms and using simple trigonometry (illustrated in Figure 3.9), one arrives at the Bragg condition for constructive interference:

$$2d\sin\theta = n\lambda \qquad\qquad \textbf{[3.1]}$$

Hence, at specific angles θ constructive interference is observed corresponding to specific distances d in the periodic crystal. These distances are also labeled d_{hkl} according to lattice planes with so-called Miller indices (hkl). These indices give information about the type and orientation of the plane.

For acquiring diffraction profiles 2θ–ω scans are carried out in which the X-ray source is usually at a fixed position, the stage rotates with ω and the detector rotates with 2θ. In this setup, an intensity profile is recorded by the detector as a function of its position 2θ. The angle of the sample stage ω is always set to half the value of 2θ resulting in a symmetric setup where the incident beam has the same angle θ with the sample as the reflected beam. Figure 3.10 illustrates the 2θ–ω scanning setup.
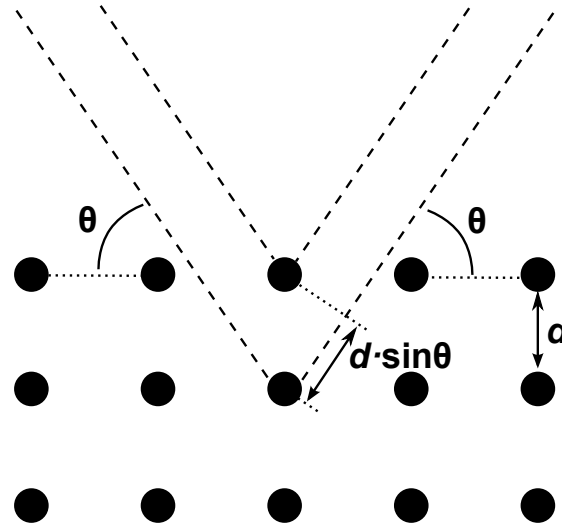
Figure 3.9.

Graphical illustration of a wave scattered by a periodic lattice. If the difference in path length ($= 2d\sin\theta$) of waves scattered by two neighboring atomic planes is equal to an integer multiple of the wave length then constructive interference occurs fulfilling Bragg's law.
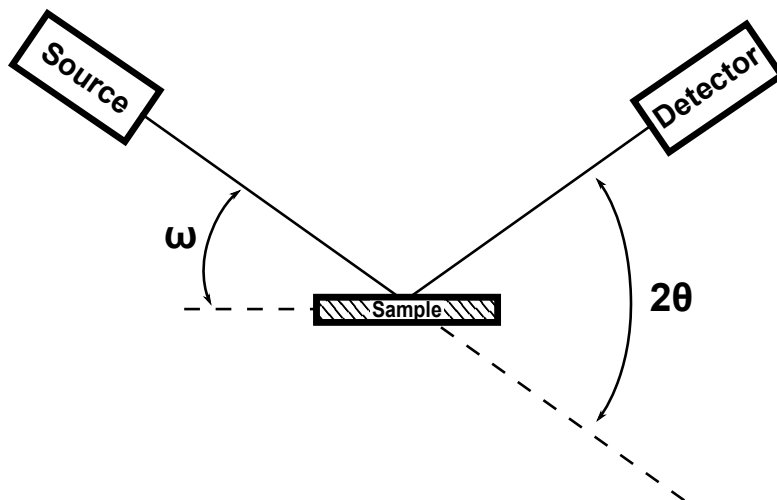
Figure 3.10.

Schematic setup for XRD measurements with the 2θ–ω scanning geometry. For a symmetric setup ω is set equal to θ.

2.2.1 Grazing Incidence X-Ray Diffraction (GIXRD)

A technique based on XRD is the grazing incidence XRD (GIXRD) technique in which ω is set to a fixed shallow angle ($\sim 1°$) while the detector scans over the 2θ range. This technique is similar to the previous one but is specifically useful for thin films on a (ideally amorphous) substrate. Due to the shallow incidence the signal stemming from the topmost surface is much larger compared to the signal stemming from the deeper regions of the sample due to the limited penetration depth. Figure 3.11 illustrates the setup used for GIXRD.

As intensity reduces with increasing angle 2θ there are two ways of reducing the scanning time for GIXRD (or XRD in general):

- Instead of using a point detector that scans along 2θ, using an areal detector that records the whole 2-dimensional information with one single measurement (also includes more information such as texture)

- Using synchrotron radiation instead of conventional Cu-Kα radiation, as the much higher intensity results in an improved signal-to-noise ratio and shorter exposure times.
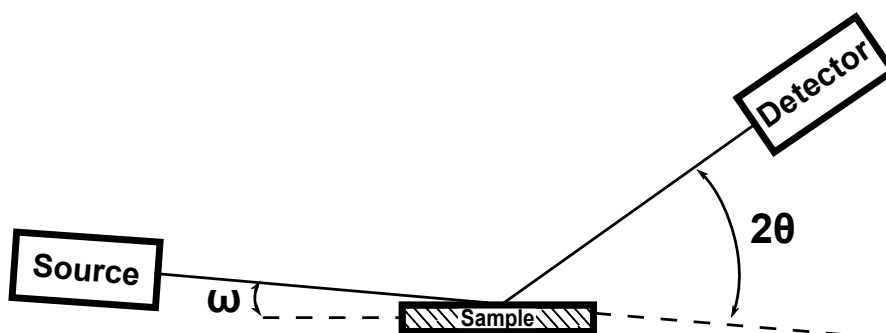
Figure 3.11.

Schematic setup for GIXRD measurements with a shallow fixed angle ω. The detector scans along 2θ.

2.2.2 X-Ray Reflectivity (XRR)

X-ray reflectivity (XRR) is an X-ray diffraction technique that is used to investigate density, thickness and roughness of thin films. Experimentally this is a 2θ–ω scan between $2\theta = 0°$ and $2\theta \sim 5°$. For a typical XRR pattern of a single layer thin film the first drop in intensity corresponds to the density of the layer. The distance between fringes (Kiessig fringes) is inversely related to the thickness of the film. The slope of the falloff of the fringes is related to the roughness of the surface. A typical XRR plot is shown in Figure 3.12 and the three film properties and its characteristic features in the XRR plot are emphasized. For more than one layer the features are more difficult to interpret and are inter-dependent, but fitting software is well developed for obtaining accurate film properties for multiple layers.
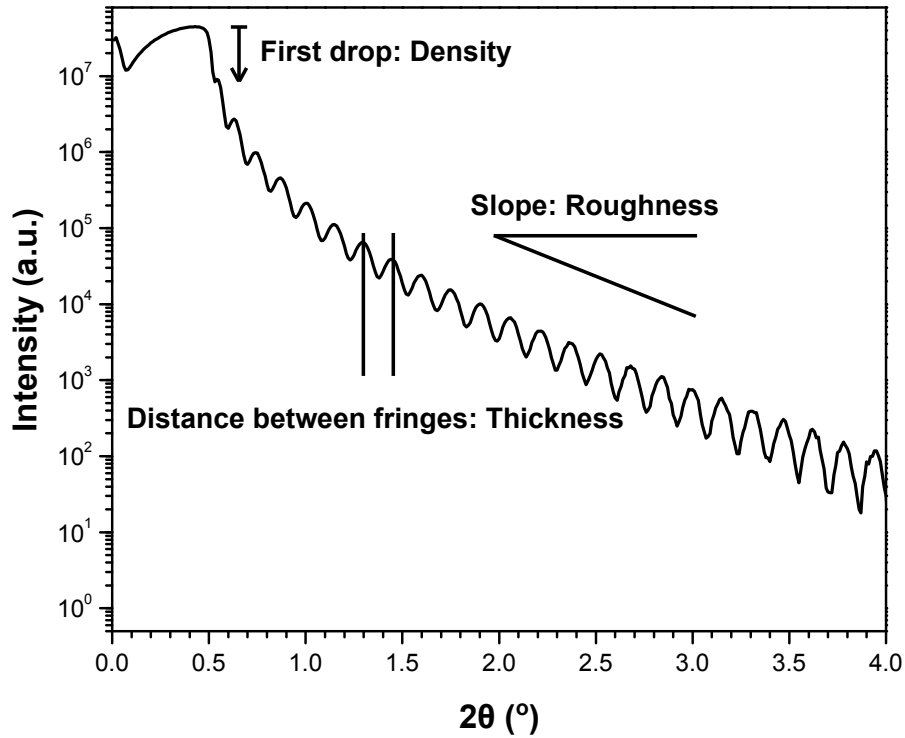
Figure 3.12.

Typical X-Ray Reflectivity (XRR) curve. Features of the XRR plot that give insight into the properties of the measured film (density, thickness, roughness) are indicated.

---

3 ──

Material Characterization by Low Energy Photons (UV/Visible)

3.1 ──

Spectroscopic Ellipsometry

Spectroscopic ellipsometry is a commonly applied technique used for determining optical properties and thickness (as well as roughness, composition, crystallinity) of thin films. For this purpose, this technique measures changes in polarization resulting from a reflection (or transmission) from a material structure (such as a thin film on top of a substrate) to gain insight into the investigated material. Figure 3.13 illustrates the experimental setup of spectroscopic ellipsometry schematically. The incident beam has a predetermined polarization and is reflected (or transmitted) from a sample. The reflected beam's change in polarization is then measured by a circular analyzer. This procedure is typically done at changing incident wavelength as well as different angles of incidence.
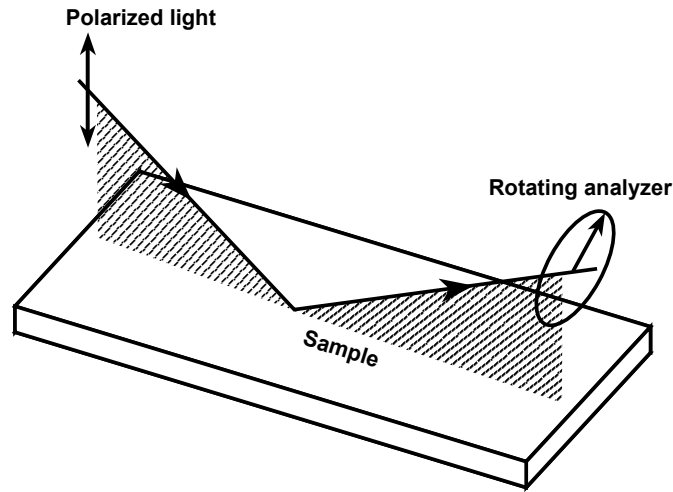
Figure 3.13.

Schematic setup of spectroscopic ellipsometry is illustrated. Incident beam is polarized and reflected off the sample, then the polarization change is measured by a circular analyzer.

The parameters measured by ellipsometry are the amplitude change Ψ and phase change Δ of the reflected wave with respect to the incident wave. With these two parameters the ratio of the two complex reflection coefficients R_p and R_s (corresponding to the p and s components of the polarized wave) is given by

$$\frac{R_p}{R_s} = \tan(\Psi)e^{i\Delta} \qquad\qquad \textbf{[3.2]}$$

Usually the angle of incidence is chosen close to the Brewster angle to maximize the difference between R_p and R_s. A typical experimental result obtained from ellipsometry is plotted in Figure 3.14.
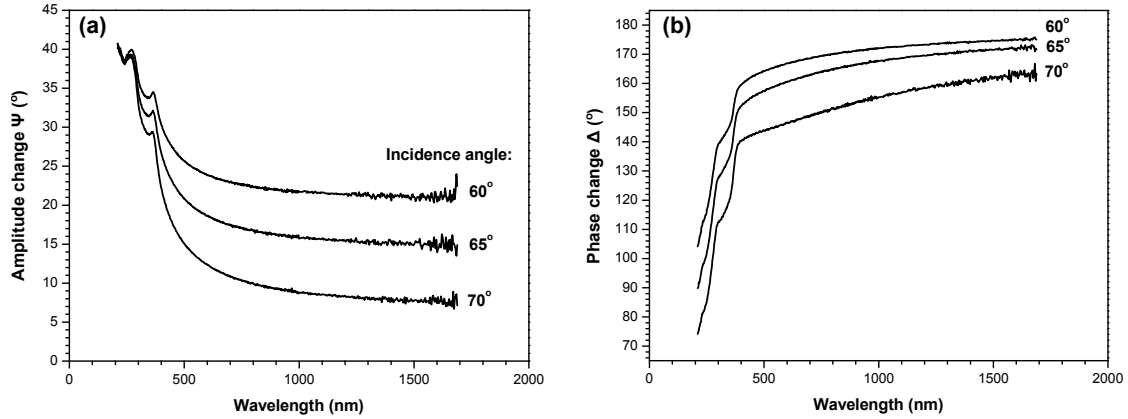
Figure 3.14.

Typical data is shown as obtained from spectroscopic ellipsometry. Polarization change is plotted as a function of wavelength of the incident beam at different angles of incidence. As the reflectance ratio is complex, two components are measured: Amplitude change Ψ and phase change Δ as displayed in (a) and (b), respectively.

Spectroscopic ellipsometry can provide information about optical properties and the thickness of a thin film by fitting models to obtained experimental data. It is important to note, that optical properties and film thickness are intertwined in the fitting model. Hence, to accurately determine the thickness of a thin film one has to know the optical properties (i.e. $n(\lambda) + i \cdot k(\lambda)$) of this material very accurately. For this purpose, either previous experimental data (from literature) can be used, or the Cauchy model can be employed to model the optical constants:[55]

$$n(\lambda) = A + \frac{B}{\lambda^2} + \frac{C}{\lambda^4} \qquad \textbf{[3.3]}$$

$$k(\lambda) = \beta \cdot \exp\left[\gamma\left(\frac{1}{\lambda} - \frac{1}{L}\right)\right] \qquad \textbf{[3.4]}$$

where A, B, C, β, γ and L are all fitting parameters.

3.2

Ultraviolet Photo-Electron Spectroscopy (UPS)

Ultraviolet photo-electron spectroscopy (UPS) is a technique in which the photo-electric effect is used to measure the work function (WF) of a metal or the valence band offset of a semi-conductor. Figure 3.15(a) illustrates a basic setup of an UPS instrument. An UV photon source is focused onto a surface and an electron counter is placed in a 90° angle to the sample surface (if the detector geometry deviates from this angle the WF is measured incorrectly[56]). The energy of the incident photons can be varied which results in plots of photon energy versus electron count. For these plots Fowler's hypothesis is used in determining the WF of metals. Straight lines are fitted to plots of quantum yield to the half power versus incident photon energy. For energies lower than the photo-electron onset a straight baseline is fitted. After the onset an increase is observed that is fitted linearly and the intersection point of this line with the baseline gives the photo threshold (i.e. the WF).[57] A typical UPS plot for determining the WF is displayed in Figure 3.15(b).

(a)   **(b)**
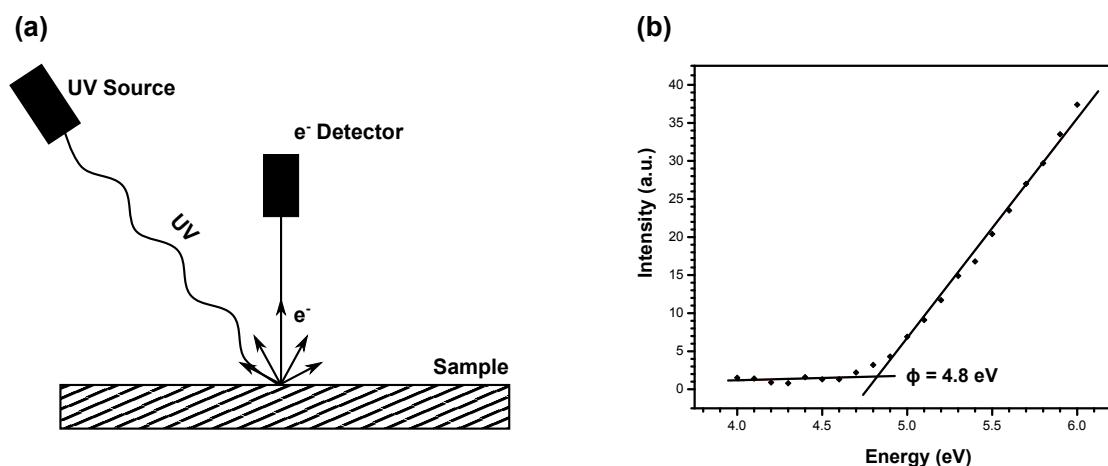
Figure 3.15.

(a) Illustration of the experimental setup for UPS. (b) Typical plot for a metal measured by UPS. Linear regression gives photo threshold that determines the WF.

4

Material Characterization by Electrons

An important tool for this thesis' characterization work was the transmission electron microscope. This section will give an overview of how it operates and which techniques it has to offer. This has been already very well discussed in my diploma thesis and hence my text has been reused here and slightly modified.[58]

4.1

Transmission Electron Microscopy (TEM)

The transmission electron microscope (TEM) became a powerful tool in material science in the last few decades and tackles the challenges and questions that arise from modern science, material physics and nanotechnology. The first TEM was build in 1932 by the group of E. Ruska and M. Knoll (as well as the group of H. Johannson and E. Brüche) that only had a similar resolution limit as a conventional light microscope. Nowadays modern TEM reach resolutions below one Ångström by means of an aberration corrector. The reason for being able to achieve such resolutions is that the wavelength λ of electrons (of the order of pm) is much smaller than the wavelength of (visible) light ($\sim$500 nm) and therefore the theoretical resolution limit δ defined by the Abbe diffraction limit is much smaller:

$$\delta = \frac{0.61 \cdot \lambda}{n \cdot \sin \alpha} \approx \frac{0.61 \cdot \lambda}{\alpha}$$

[3.5]

where n is the refractive index and α the collection semi-angle. In the case of the TEM the refractive index is equal to one and the collection angle is very small due to aberrations and small diffraction angles. Hence, in TEM the wavelength, the aberrations and the collection angle govern the resolution limit.

Electrons can easily be focused to a designated part of the sample which can give local diffraction information unlike X-ray methods (as discussed in the previous section) that averages over the bulk.

Additionally, electrons (= ionizing radiation) interacting with the sample produce a wide range of secondary signals from the sample such as characteristic X-rays that can be facilitated for spectrometry and elemental mapping. One common technique is energy dispersive X-ray spectroscopy (EDX).

Magnetic lenses are applied to focus electrons building an electro-optic system. To achieve high resolution in a TEM the aberrations of the magnetic lenses have to be corrected and minimized. The main disadvantage of using electrons is that extremely thin specimens are required to transmit electrons. This makes sample preparation difficult (as discussed in a following section).

Figure 3.16 illustrates the basic setup of a TEM operating in both imaging and diffraction mode.[59] There are two types of sources for electrons: Field-emission and thermionic sources. Field-emission sources emit electrons when a high electric field is applied while thermionic ones produce electrons when heated. The big advantage of field-emission

sources is that they irradiate monochromatic electrons. Tungsten, Wolfram or LaB_6 are commonly used as filament which lies inside the Wehnelt cylinder. The emitted electrons are accelerated by the applied voltage between filament (cathode) and anode (typically $80 - 300$ kV) and then focused by condensor lens(es) with the typical diameter of the electron beam being a few micrometers. The electron beam is diffracted by transmitting through a specimen and forms the first diffraction pattern in the back focal plane where an objective aperture can be inserted to select a specific diffraction spot. Selecting a diffracted spot for the formation of an image makes it a dark-field (DF) image. While selecting the un-diffracted spot results in an image that is called bright-field (BF) image. Beams that pass the objective aperture form the first intermediate image by use of the objective lens. In the plane where this image is formed a selector aperture can be inserted to select a specific area to get a diffraction pattern from — this technique is called selected area diffraction (SAD). Below this selector aperture there are two more magnetic lenses (intermediate and projector lens) to increase the magnification of the final image at the imaging plane. The strength of the intermediate magnetic lens is changed to switch between imaging and diffraction mode. Switching between image and diffraction pattern can be done almost instantaneously and is one of the big advantages of using a TEM.

Setup, components such as magnetic lenses and their aberrations as well as contrast formation of TEM images, theory of diffraction among many other topics are discussed in more detail in the standard textbooks.[59–63]

Bright field imaging   **Selected area diffraction**

Wehnelt cylinder

Anode
Condensor lens
Condensor aperture

Specimen

Objective lens

Objective aperture   **1ˢᵗ diffraction pattern**

Selector aperture   **1ˢᵗ image**
Intermediate lens

                           2ⁿᵈ image   **2ⁿᵈ diffraction pattern**

Projector lens

Screen/Camera
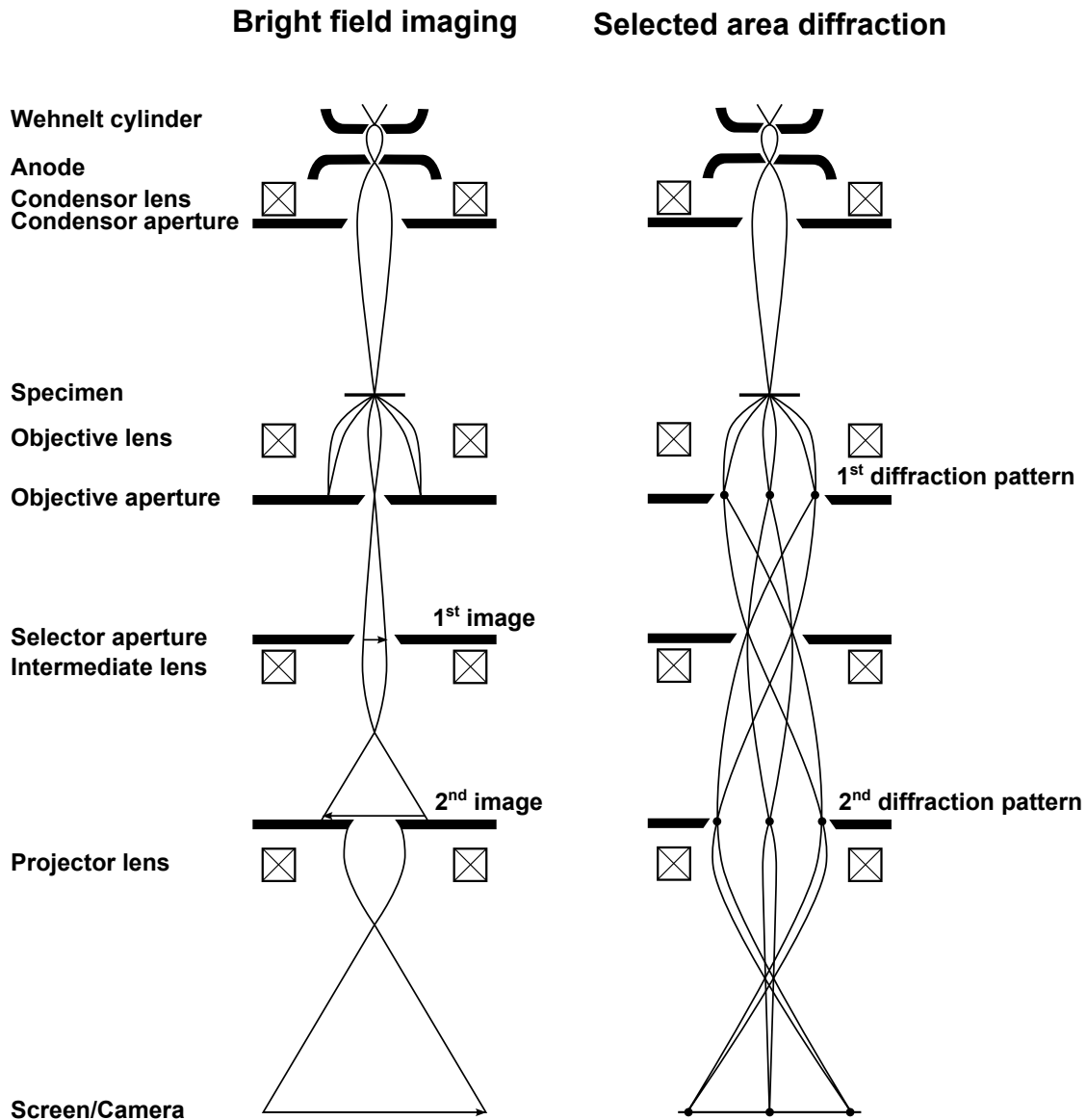
Figure 3.16.

Schematical setup of a TEM is depicted. Bright field (BF) imaging mode and selected area diffraction (SAD) mode are illustrated on the left and right side, respectively. The intermediate lens in SAD mode is used at lower voltages than in imaging mode in order to display the diffraction pattern on the screen. Adapted from **[59]**.

4.1.1 High-Resolution TEM (HRTEM)

BF and DF TEM imaging techniques are not capable of resolving columns of atoms. This becomes more clear once one is aware that the diffracted electron wave function can be written as the Fourier transform of $f(\vec{r})$, the scattering factor distribution: $\psi(\overrightarrow{\Delta k}) = \mathcal{F}[f(\vec{r})]$. For BF/DF only a very small range of k values in the reciprocal space is selected by the objective aperture and therefore cuts off higher spatial frequencies (that being equivalent to smaller distances). In high-resolution TEM (HRTEM) a bigger (or no) objective aperture is used. Since HRTEM is a phase contrast imaging technique the aperture has to include the transmitted beam and at least one of the diffracted beams. The formation of lattice fringes in phase contrast imaging may be illustrated by looking at the interference of two beams: 0 and g. The resulting intensity gives a sinusoidal oscillation normal to $\vec{g}$ with the distance of the maxima being equal to $1/g$.[62] Figure 3.17 illustrates lattice fringes for different apertures.
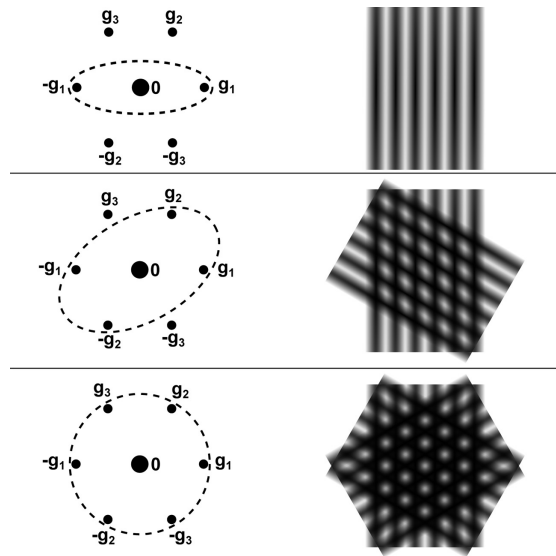
Figure 3.17.

Lattice fringes resulting from the interference of the selected diffraction spots as depicted on the left. Area of selection corresponds to the apertures that are illustrated by dashed ellipses.

Note that the fringes observed are not direct images of the structure but instead give information about crystal orientation and lattice spacings.

In the idealized case (no aberrations) the spatial resolution increases with increasing number of collected (diffracted) beams within the aperture. But mainly due to spherical aberration of the objective lens the information corresponding to high spatial frequencies (high k values) is lost. This sets the spatial point resolution of the TEM. Nowadays, thanks to spherical aberration correction this limit has fallen below 1 Å. Furthermore, each (ideal) point in the sample becomes a disc in the image. This is described by the

point spread function (PSF). Thus, the object wave function $\psi(\vec{r})$ is convoluted (denoted by $\otimes$) with the PSF and gives the intensity distribution at the imaging plane. The Fourier transform of the PSF is called the contrast transfer function (CTF). This is summarized in the following table:

Object		**Image**
$\psi(\vec{r})$	$\rightarrow$	$\psi(\vec{r}) \otimes \mathrm{PSF}(\vec{r})$
$\mathcal{F}[\psi(\vec{r})] = \psi(\vec{g})$	$\rightarrow$	$\mathcal{F}[\psi(\vec{r})] \cdot \mathcal{F}[\mathrm{PSF}(\vec{r})] = \psi(\vec{g}) \cdot \mathrm{CTF}(\vec{g})$

The CTF can be expressed as $\exp(i\chi(\vec{g}))$ where $\chi(\vec{g})$ is the phase distortion function that is given by[62]:

$$\chi(\vec{g}) = \pi \Delta f \lambda g^2 + \frac{1}{2}\pi C_{\mathrm{s}} \lambda^3 g^4 \qquad \textbf{[3.6]}$$

For the object wave function the phase-object approximation can be applied (holds only for thin specimen). Hence, the 3-dimensional potential $V(x, y, z)$ of the sample is projected onto a 2-dimensional potential of thickness t:

$$V_t(x, y) = \int_0^t V(x, y, z) \mathrm{d}z \qquad \textbf{[3.7]}$$

Furthermore, it is assumed that $V_t(x, y) \ll 1$ for thin specimen that being the so-called weak phase object approximation (WPOA). Thus,

$$\psi(x, y) = \mathrm{e}^{i\sigma V_t(x,y)} \approx 1 + i\sigma V_t(x, y) \qquad \textbf{[3.8]}$$

where σ is the interaction constant.
Finally, putting the CTF and Equation 3.8 together gives

$$I = \psi \cdot \psi^* = 2\sigma V_t \sin(\chi(\vec{g})) \qquad \textbf{[3.9]}$$

At points where $\sin(\chi(\vec{g}))$ is zero no contrast is transferred. Hence, to optimize the CTF one has to minimize the number of zeros of this function. This can be achieved by balancing the focus Δf and the spherical aberration C_{s}. The optimum is obtained at the Scherzer defocus and is given by[62]

$$\Delta f_{\mathrm{Scherzer}} = -1.2\sqrt{C_{\mathrm{s}}\lambda} \qquad \textbf{[3.10]}$$

At $\Delta f_{\mathrm{Scherzer}}$ all information is transferred up to the first zero-crossover.

Interpreting HRTEM/phase contrast images of atomic structures is not an easy task due to the fact that the contrast is affected by spherical aberration, defocus, thickness of the specimen and the microscope itself (PSF).

4.1.2 **Cross-sectional TEM Sample Preparation**

TEM sample preparation in a cross-sectional view is necessary and useful for a lot of samples but especially important when dealing with thin films deposited on a substrate. With this technique film thickness, morphology, interfaces and structure can be investigated in a TEM. In this section, a conventional way of preparing cross-sectional TEM samples is explained as it introduces less artifacts into the sample compared to a focused ion beam (FIB) preparation approach. While the conventional approach is less destructive it also takes more effort and time to learn this and carry out this procedure.
Figure 3.18 illustrates the main steps of a conventional cross-sectional TEM sample preparation. In the following list the steps will be explained assuming the sample is a thin film that was deposited on a Si substrate:

[1.] The Si sample is broken apart into at least two pieces (roughly 100 mm × 10 mm rectangles) and glued together face to face using a Gatan G1 two component epoxy. This epoxy glue is liquid at room temperature and hardens when heated over ~ 150 °C. This step makes a stack of two Si pieces with the deposited layers embedded in between (hence it would be protected from oxidation from this point on, in case the sample is sensitive to air exposure).

[2.] Once more the pieces are embedded with the same glue within two pieces of Si to make the stack more robust against the mechanical treatment in the next steps.

[3.] This stack is sliced by a diamond saw orthogonal to its long side (100 mm long) to cut one or more samples of width 1–2 mm.

[4.] The sliced sample is further drilled with a circular drill to make the rectangular shape fit the TEM holder's restriction of a maximum diameter of 3 mm. Figure 3.18 displays a zoom-out of the cross-section showing that the Si pieces with the deposited layer face each other and are separated by roughly 1 μm of epoxy glue.

[5.] Now the sample is mechanically polished (starting with a rough lapping paper of 30 μm granular size and transitioning step-wise to a fine paper of 1 μm) from both sides to have a thickness of below 20 μm. Note that the illustration shows the side view of the sample that was displayed in the previous step.

[6.] In this (optional) step the sample is further grinded by a dimple grinder (illustration in Figure 3.18) to make the sample thinner close to the center/cross-section.

[7.] The very thin sample is carefully removed from the stub/holder that was used for grinding by acetone and transfered to a (diameter 3 mm) TEM slot grid with the Gatan two component epoxy.

[8.] In the last step, the sample is ion milled by a Gatan PIPS 2 at 5 kV, 3 kV, 1 kV at angle setting 5, 3, 1, respectively. This is done until a hole starts to form at the cross-section. Close to the hole the sample should be less than 100 nm in thickness, hence electron transparent and ready for TEM characterization.

Even though conventional cross-sectional TEM preparation is much less destructive and hence introduces less artifacts than an FIB approach, potentially still artifacts such as heating,[64, 65] generation of an amorphous layer[66] or physical/chemical damage/(re)deposition may be introduced.[65]
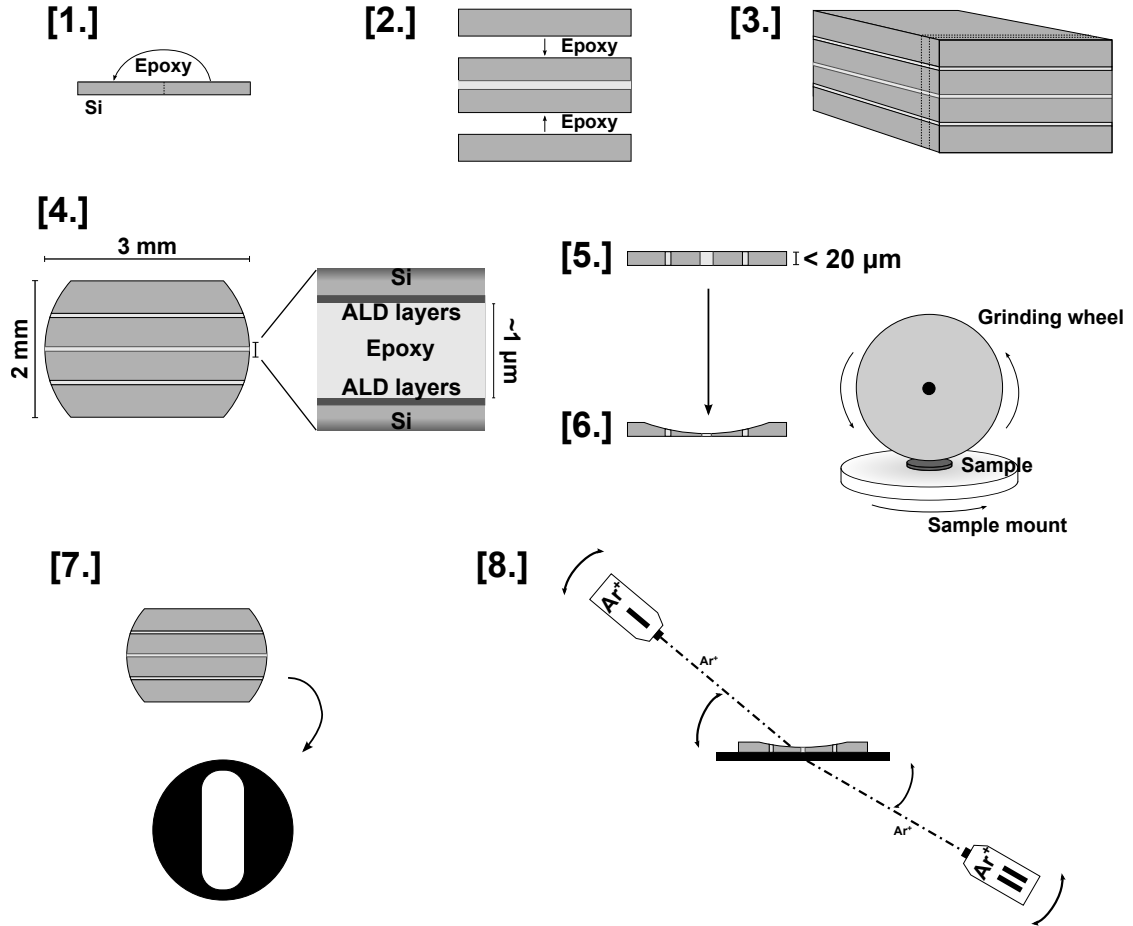

Figure 3.18.

Graphical illustration of the cross-sectional TEM sample preparation steps. Each step from (1.)–(8.) is explained in the main text.

4.2

Selected Area Electron Diffraction (SAD)

As just described, in the plane where the first intermediate image is formed by the objective lens a selector aperture can be inserted to select a specific area to get an SAD pattern from. An SAD pattern gives information of the Fourier-transformed object wave function $\psi(\vec{r})$, or to be more precise, about $|\mathcal{F}[\psi(\vec{r})] \cdot \mathcal{F}[\text{PSF}(\vec{r})]|^2$. In Fourier space periodic features in the object wave function (eg. stemming from a crystalline lattice) are equivalent to single points (with their distance from the center being inverse proportional to the spacing of the corresponding periodicity in real space). This property is very useful when categorizing the structure of an area with periodic features (or lack thereof).

Figure 3.19 illustrates the different categories of SAD patterns that can be observed depending on the type of structure that is investigated:

- **Amorphous, (a):**
  It has no long-range order and consists of randomly arranged atoms (that still may have a short/medium-range order). Its SAD pattern has an un-diffracted central spot and intensity falling off radially from that center. A radial intensity profile shows a broad peak with its peak distance from the center corresponds inversely to the next-nearest neighbor distance of the atoms (radial atomic distribution function).

- **Crystalline, (b):**
  It has a periodic long range order and consists of atoms arranged in a lattice. Its corresponding SAD pattern shows sharp peaks that stem from different symmetry planes in the crystal. Also, the observed pattern is a 2-dimensional cut of the 3-dimensional reciprocal lattice of the crystal.

- **Polycrystalline (without texture), (c):**
  It has domains of long-range order, but these domains are randomly oriented. This causes the discrete diffraction spots to become diffraction rings. The radius of the ring is inversely proportional to the distance of the corresponding symmetry planes in the crystal.

- **Polycrystalline (with texture), (d):**
  It has domains of long-range order and these domains are not completely randomly oriented but have preferred directions (i.e. a texture). Here only certain arcs of the rings are visible depending on the texture of the material. An arc always shows an equivalent arc mirrored across the center (un-diffracted) spot.

- **Nanocrystalline, (e):**
  It has small domains (few 100 nm or less in diameter) of long-range order (that actually may contain texture or not). The resulting SAD pattern shows spots and small arcs of the diffraction rings (with some or no texture observed).
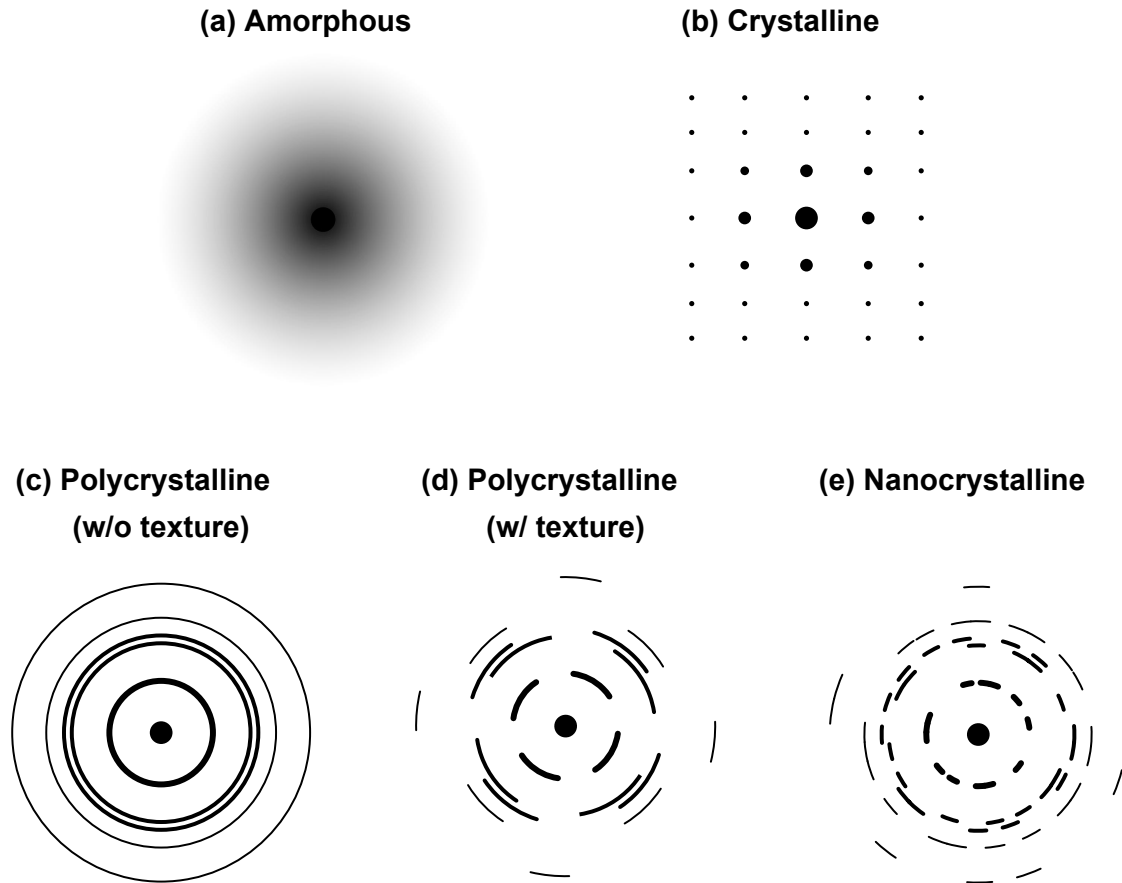
Figure 3.19.

Illustration of SAD patterns originating from different structures: (a) Amorphous, (b) Crystalline, (c) Polycrystalline without texture, (d) Polycrystalline with texture and (e) Nanocrystalline. Note that dark and bright are inverted in this illustration.

Experimental Work

Contents

┌─ 1 ───┐
│   │
│   **PEALD of TiO$_2$ on High AR Substrates**   │
│   │
└──┘

As described in the introduction of this thesis, key pieces of modern day technology such as the DRAM keep following the trend of device scaling.[67] Two strategies are pursued to maintain the necessary capacitance while scaling down the area of the DRAM: Using a high–k dielectric and facilitating a high aspect ratio (AR) surface to enhance the capacitance by the effective surface area.[68–70] Hence, first the conformal coverage of TiO$_2$ on high AR substrates is studied in detail in this section.

1.1

Introduction

Promising candidates for high–k dielectric materials are HfO$_2$,[27] BaTiO$_3$[18] as well as TiO$_2$.[71] Furthermore, TiO$_2$ is the basis for more complex high–k dielectrics such as the perovskites (BaTiO$_3$, SrTiO$_3$ and BaSrTiO$_3$) as well as Al-doped TiO$_2$ that not only have a high dielectric constant but also exhibit low leakage currents.[72] Aside from being an attractive choice for a high–k dielectric, TiO$_2$ has a wide variety of applications such as dye-sensitized solar cells,[73] gas sensors[74] and photocatalysis.[75] Generally, crystalline TiO$_2$ exists in three polymorphic modifications — anatase, rutile, and brookite — that have different dielectric constants. Anatase has a dielectric constant of around 40 whereas rutile's dielectric constant is about 80, although there is a large variation in these values depending on synthesis method and geometry.[76–78] The brookite phase is theoretically estimated to have an even higher dielectric constant than the rutile phase.[79, 80] There are no experimental reports for the dielectric constant of brookite TiO$_2$ due to the fact that it is not a stable phase by itself and is always accompanied by secondary phases.

Atomic layer deposition (ALD) is a thin film deposition technique that is known to have precise thickness control down to the sub-nanometer range as well as the ability to deposit films conformally over complex high AR 3D structures.[45] Plasma enhanced ALD (PEALD) is a modification of ALD that facilitates plasma (e.g. O$_2$, N$_2$, Ar, H) as the second reactant to strip off the remaining ligands at the surface in contrast to using a gas (e.g. water vapor, ozone, or NO$_2$). PEALD has advantages over conventional thermal ALD processing including lowering of process temperature (hence minimizing the thermal damage during device fabrication), improving film quality (density, electrical properties and roughness) and enabling deposition of new materials.[47, 48] While for thermal ALD it has been shown that conformal coverage of 3D structures up to an AR of 1:200 is feasible,[49] PEALD is often thought to have a disadvantage because excited plasma species tend to recombine on sidewalls in narrow trenches.[50, 51] In literature, a conformal coverage of 3D structures for SiO$_2$ and HfO$_2$ up to an AR of 1:60 has been shown for PEALD films.[52] Simulations indicate that for PEALD processing with plasma species that have low probability of recombination loss a conformal coating of ARs of 1:30 should be feasible, whereas for plasma species that exhibit high recombina-

tion losses ARs as low as 1:10 may be challenging.[54] Conformal coatings of high AR substrates is important not only for DRAM but can also be facilitated to functionalize nanoparticles[81] and to fabricate nanostructures.[82]

In this section we establish PEALD as a fabrication approach to synthesize a thin film (< 20 nm) of TiO_2 on the surface of a high AR trench substrate with thickness controlled down to the nanometer scale. We show that a conformal coverage of trenches up to an AR of 1:30 can be obtained by increasing the in-cycle plasma exposure time. Cross-sectional transmission electron microscopy (TEM) is used to evaluate step coverage (i.e. thickness of deposited layer at the bottom divided by its thickness at the top of the high AR trench substrate). High resolution TEM (HRTEM) and grazing incidence X-ray diffraction (GIXRD) data reveal structural information of the deposited TiO_2 layer and are further corroborated by energy dispersive X-ray spectroscopy (EDX) maps.

1.2

Experimental Methods

1.2.1 Material Fabrication

TiO_2 was deposited by plasma enhanced atomic layer deposition (PEALD) in a Fiji ALD reactor (Cambridge Nanotech/Ultratech) that is equipped with a remote inductively coupled plasma generator. The base pressure of this ALD reactor is 200 mTorr while there is a constant flow of Ar at 60 sccm in the precursor manifold line. Tetrakis-(dimethylamido)titanium (TDMA–Ti) and O_2 plasma were used as precursors. The titanium precursor was maintained at 75 °C and was pulsed for 0.3 s per cycle followed by a 60 s long exposure (i.e. valve separating chamber and pump closed). After the TDMA–Ti exposure the chamber is purged for 60 s to remove the remaining (unreacted) precursor and the by-product resulting from the reacted ligands. As co-reactant an oxygen plasma is used generated by a remote inductively coupled plasma generator at a power of 300 W. A constant flow of Ar with 200 sccm is provided through the plasma line while during the plasma step there is an additional O_2 flow of 50 sccm. After the plasma exposure the chamber is purged for another 10 s. Substrate temperature and plasma exposure time are varied and studied in this paper. All TiO_2 films were deposited by 200 cycles with the above described parameters.

1.2.2 Material Characterization by TEM

The cross-sections of the samples were prepared following the conventional TEM sample preparation procedure described by Strecker et al.[83] Samples were glued face–to–face, mechanically polished to less than 10 μm. Final thinning to TEM transparency was performed by ion milling in a precision ion polishing system (Gatan, PIPS 2). Selective area diffraction (SAD) pattern analysis was performed in order to examine the crystallinity of (PE)ALD TiO_2 films on trench substrates. The diffraction data were collected over the selected area of $3.4 \cdot 10^4$ nm^2. The morphology of the trenches and step coverage was

examined using transmission electron microscopy (TEM, FEI Tecnai G2 F20 X–TWIN FEG, 200 kV) equipped with an energy dispersive X-ray spectrometer (EDX) that was utilized to examine the elemental composition of the trenches in plan and cross sectional view.

1.2.3 Material Characterization by XRD

For the grazing incidence X-ray diffraction (GIXRD) data a synchrotron radiation measurement was conducted at the SLAC National Laboratory (Stanford, CA). Synchrotron radiation yields a better signal–to–noise ratio compared to conventional XRD sources due to the higher intensity and the directionality of the beam. The beam energy was 12.7 keV, resulting in a wavelength λ of 0.97626 Å. The beam power was 10 kV $*$ 20.0 mA. The sample was placed 150 mm away from an aerial detector with a grazing angle ω set to 1°. The detector was exposed for 30 seconds per measurement. The recorded aerial diffraction pattern was then integrated radially to display the intensity versus 2θ plots (unprocessed aerial data is shown in Figure 4.9). The amorphous background was subtracted.

1.3

Results and Discussion

A typical substrate that is used for enhancing the capacitance of a dynamic random access memory (DRAM) device is illustrated in Figure 4.1(a). Cylindrical holes are etched into thermally grown SiO$_2$ to enhance the effective surface area of the substrate that therefore increases the capacitance. The substrate that is used in this work consists of trenches (i.e. cylindrical holes) that have a diameter of about 55 nm and a depth of 1600 nm, giving a high aspect-ratio (AR) of 1:30. The morphology of the trenches resembles a conical cylinder that reduces in diameter with depth. To assess how well a dielectric layer can coat such a high AR substrate, thermal atomic layer deposition (ALD) and plasma enhanced ALD (PEALD) of TiO$_2$ thin films were studied as shown in the schematic in Figure 4.1(b). The step-coverage is the metric used to assess the quality of coverage of the deposited films and is defined as the thickness d_{bottom} of the film at the bottom of the trench-like substrate divided by the thickness d_{top} at the top, in percent [cf. inset images in Figure 4.1(b)]. Figure 4.1(c) shows a cross-sectional transmission electron microscopy (TEM) image of the high AR trench substrate without any deposition at low magnification. To compare thermal ALD with PEALD in terms of step-coverage 200 cycles of TiO$_2$ were deposited on the high AR substrate using both techniques with a substrate temperature of 250 °C. In PEALD of TiO$_2$ an O$_2$ plasma exposure time of 3 s was chosen per cycle. Figure 4.1(d) and (e) display cross-sectional TEM images taken of TiO$_2$ deposited by thermal ALD at the top and bottom of the trench-like substrate, respectively. The measured thickness was averaged for five different locations in the sample. Thickness of the TiO$_2$ layer deposited by ALD was (12.51 ± 0.18) nm and (12.06 ± 0.14) nm at the top and at the bottom respectively, corresponding to a

step-coverage of (96.4 ± 1.4) %. Figure 4.1(f) and (g) show analogous results for TiO_2 deposited by PEALD. For PEALD of TiO_2 the thickness of the layer was (14.68 ± 0.48) nm and (11.64 ± 0.35) nm at the top and at the bottom respectively, corresponding to a step-coverage of (79.3 ± 2.6) %. The thickness of TiO_2 deposited by (PE)ALD decreases monotonically from top to bottom of the trench.

The observation of a step coverage close to 100 % for the TiO_2 film deposited by thermal ALD on a substrate with an AR of 1:30 is in good agreement with literature data.[49, 84] During thermal ALD the precursor pulse time is the main limiting factor for high AR coverage.[85] Hence, the perfect coverage of TiO_2 during thermal ALD ensures that the chosen TDMA–Ti pulse time of 0.3 s is sufficiently long and cannot be a limiting factor during PEALD either. The lower step-coverage for the TiO_2 film deposited by PEALD can be explained by the fact that excited plasma species are likely to recombine on the sidewalls of narrow trenches.[50, 51]
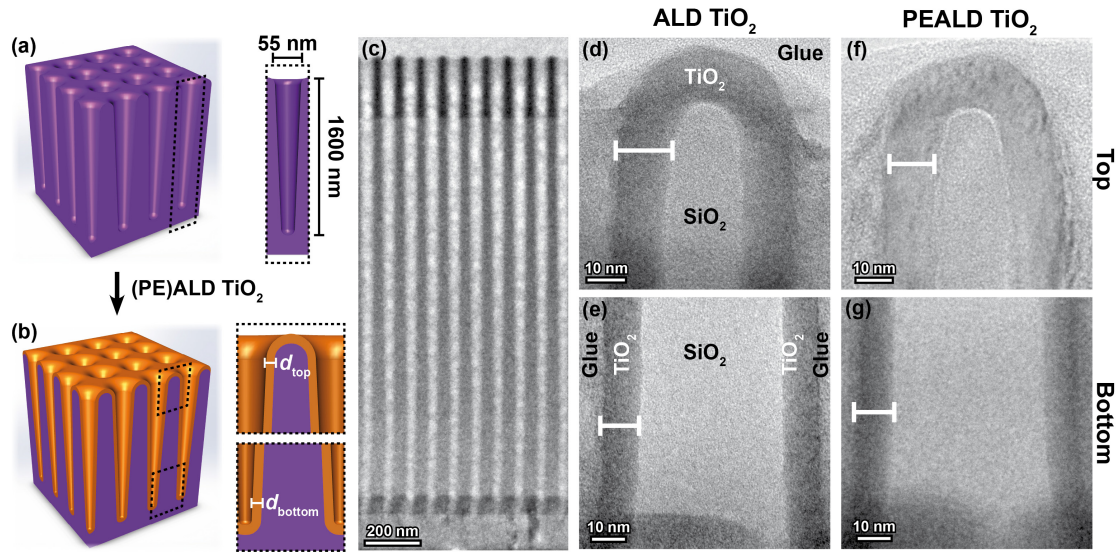
Figure 4.1.

(a) Schematic illustrating the morphology of the high AR trench substrate. Inset indicates dimensions of trench-like holes that give an AR of 1:30. (b) Illustration of substrate covered with TiO_2 by (PE)ALD. The step coverage (in percent) d_{bottom} / d_{top} is measured as shown in the inset images. (c) Cross-sectional TEM image of high AR trench substrate. (d),(e) Trench substrate with TiO_2 deposited by thermal ALD (250 °C, 0.3 s TDMA–Ti (heated to 75 °C) pulse, 0.06 s H_2O pulse) in cross-sectional view at the top and bottom, respectively. (f),(g) Trench substrate with TiO_2 deposited by PEALD (250 °C, 0.3 s TDMA–Ti (heated to 75 °C) pulse, 3 s O_2 plasma) in cross-sectional view at the top and bottom, respectively.

To further investigate the morphology and chemistry of PEALD TiO_2 films on high AR substrates elemental energy dispersive X-ray spectroscopy (EDX) maps were performed in scanning TEM mode both in cross-sectional view and plan view as displayed in Figure 4.2(a)–(d) and (e)–(h), respectively. The maps colored in green for the Si–K

edge are shown in (b) and (f). The Ti–K edge maps in yellow are displayed in (c) and (g). The red maps in (d) and (h) view the signal resulting from the O–K edge.

From the EDX maps a clear interface between the PEALD TiO$_2$ layer and the high AR SiO$_2$ substrate can be found. This observation is in agreement with a low diffusion coefficient of Titanium in thermally grown SiO$_2$, that has been reported[86] to be lower than $6 \cdot 10^{-19}$ cm^2/s at 1000 °C (substrate temperature in our sample was as low as 250 °C).
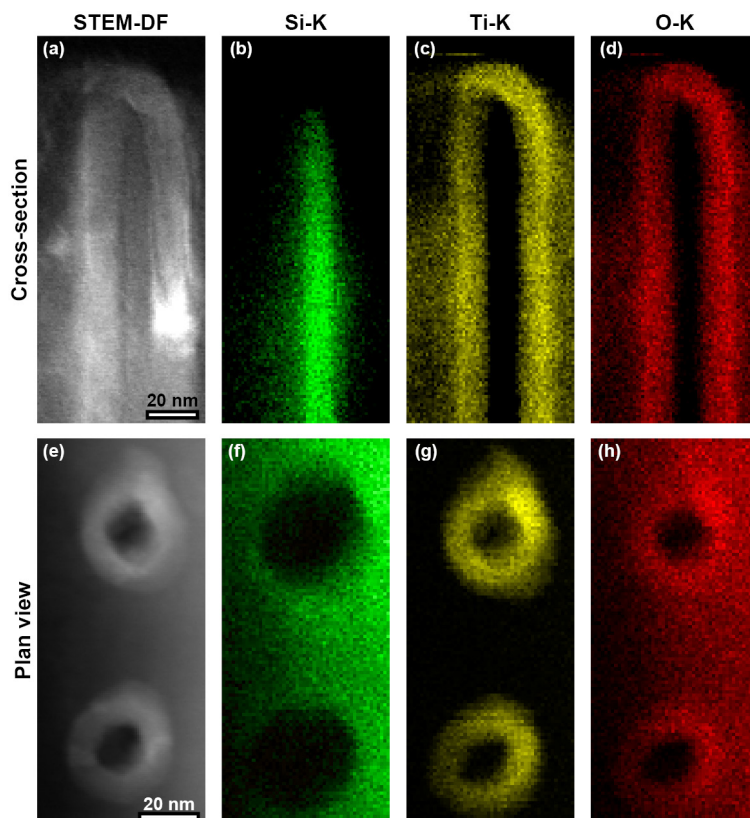
Figure 4.2.

STEM-DF and EDX maps illustrate the morphology of PEALD TiO$_2$ films on high AR trench substrates in cross-sectional view, (a)–(d), and plan view, (e)–(h). EDX elemental maps of Si, Ti and O are shown in (b)&(f), (c)&(g) and (d)&(h), respectively.

In terms of step-coverage PEALD at a common plasma exposure time (3 s per cycle) showed inferior performance compared to thermal ALD (as seen in Figure 4.1). Previously, it has been shown that the conformality of PEALD can be improved by (i) increasing the plasma power, (ii) increasing the chamber pressure and (iii) increasing the plasma exposure time.[53] Also, for thermal ALD it is known that reactant exposure time is the limiting factor for coating high ARs conformally.[85]

Hence, studying the effect of changing the plasma exposure time on the step-coverage during PEALD of TiO_2 is of interest. The plasma exposure times in this study are 1–2 orders of magnitude longer than conventionally applied. While from an industrial perspective extended plasma duration may not be desirable it may become feasible in next generation reactor designs. Figure 4.3 plots step-coverage of PEALD TiO_2 films (200 cycles) on high AR trench substrates at 200 and 250 °C substrate temperature as a function of the plasma duration per cycle. The step-coverage of the PEALD TiO_2 film at substrate temperature 200 °C and plasma duration per cycle of 3 s, 60 s and 180 s was $(89.3 \pm 4.4)\%$, $(92.9 \pm 2.1)\%$ and $(95.9 \pm 2.0)\%$, respectively. For the PEALD TiO_2 film at a substrate temperature of 250 °C the step-coverage for the samples with a 3 s, 60 s and 180 s plasma duration was $(79.3 \pm 2.6)\%$, $(85.5 \pm 3.2)\%$ and $(93.4 \pm 5.2)\%$, respectively. Corresponding TEM micrographs, detailed thicknesses from the top and bottom of the trench and GPC at the top of the trenches can be found in section 1.5. Any positive step coverage, even at a short plasma duration (3 s), is compatible with the surface recombination loss probability r of oxygen on SiO_2, that being as low as $\sim 10^{-4}$.[87, 88] Furthermore, the reaction probability s (also referred to as sticking probability) of an oxygen plasma during PEALD of Al_2O_3 has been reported to be higher than 0.1.[54] Due to the low recombination loss probability r and the high reaction probability s the PEALD TiO_2 process is in the diffusion-limited deposition regime, i.e. that is the regime in which the saturation dose strongly increases with increasing AR (but depends little on the reaction probability s).[54] This also explains the improvement in step coverage with prolonging the plasma duration which increases the dose of plasma radicals.

Combustion-type reactions of oxygen radicals with the organic CH_3 groups of the TDMA–Ti precursor produce CO, CO_2 and H_2O.[89] The H_2O produced in the primary combustion reaction can further react with an unreacted organic ligand giving rise to a thermal ALD component during PEALD. This secondary thermal ALD reaction plays a minor role in case of a flat substrate since the secondary reaction competes with primary combustion of ligands where the flux of oxygen radicals is much larger than the amount of secondary H_2O. However, it might become more dominant for a high AR trench substrate as the flux of plasma radicals decreases with increasing depth into the trenches, resulting in unreacted CH_3 groups that are available to react with the secondary H_2O.

Reactivity of TDMA–Ti precursor with oxygen (no plasma) alone was observed during our experiments and to our knowledge there has been no report about this observation in literature to date. Oxygen's reactivity with TDMA–Ti is fairly low (0.057 Å/cycle for 100 pulses of TDMA–Ti with 15 s exposure of oxygen) but might contribute to the improvement of step-coverage during long exposure times due to no recombination losses of unexcited species of O_2 down the high AR trench. It should be noted that at 250 °C the TDMA–Ti precursor starts to decompose which might contribute to the step coverage.[90]

Radicals are less likely to recombine at trench side-walls at lower temperature.[54] Hence, the overall lower step coverage of TiO_2 grown at a higher temperature of 250 °C can be explained by the fact that the recombination loss probability r for oxygen increases for increasing temperatures.[91]
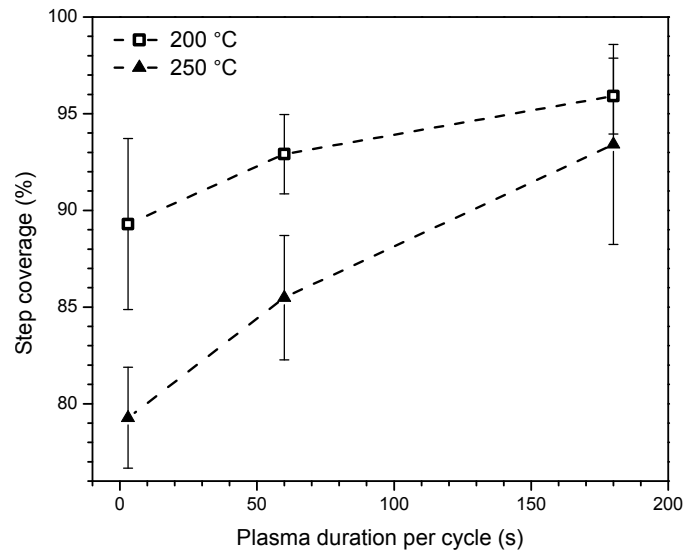
Figure 4.3.

Step coverage of PEALD TiO$_2$ on high AR trenches as a function of plasma exposure time in the oxidation half-cycle at a substrate temperature of 200 and 250 °C. Error bars indicate standard deviations taken from 5 measurements within the same cross-sectional TEM sample.

To get insight into the structure of the deposited films TEM and grazing incidence X-ray diffraction (GIXRD) were employed as displayed in Figure 4.4. The high resolution TEM (HRTEM) micrograph in cross-sectional view (taken at the top of the high AR trench substrate) in Figure 4.4(a) displays PEALD TiO$_2$ deposited at 250 °C with a plasma exposure time of 60 s. The SiO$_2$ high AR substrate shows amorphous contrast whereas the deposited TiO$_2$ shows lattice fringes that are displayed in Figure 4.4(b) in an inverse (filtered) fast Fourier transformation (IFFT) image. From the IFFT two lattice spacings of 4.32 and 3.49 Å with an angle of 64.7° can be identified as (200) and (111) planes of the brookite phase of TiO$_2$, respectively. Figure 4.4(c) compares the experimentally acquired selected area diffraction (SAD) pattern (sample with 250 °C substrate temperature) with a simulation of the electron diffraction pattern for the anatase phase of TiO$_2$. The diffraction spots in the SAD pattern fit very well to the simulated anatase pattern. In addition, two spots corresponding to a spacing of 2.91 and 2.49 Å are observed and can be attributed to the (211) and (102) planes of the brookite phase of TiO$_2$, respectively. To corroborate the structural data obtained by TEM, Figure 4.4(d) displays GIXRD patterns of PEALD TiO$_2$ deposited at 200 and 250 °C with a plasma duration of 60 s. The peaks stemming from the underlying Si substrate are denoted by an empty triangle. At both substrate temperatures the anatase phase peaks of TiO$_2$ (denoted by a solid rhombus symbol) are observed. In the sample with substrate temperature of 250 °C an additional peak for the brookite phase of TiO$_2$ (denoted by empty square) can be found at 19.6° corresponding to the (121) plane. Further brookite peaks may overlap with Si and/or anatase peaks at 16.1°, 29.8° and 34.2° for the (111),

(231) and (241) planes in brookite, respectively. Detailed overview of peak positions and corresponding phase are listed in Table 4.1. Raw data from the areal detector is available in section 1.5 and shows that there is no texture in the PEALD grown crystalline TiO_2 film.

The structural information gained from the SAD pattern of the sample deposited at 250 °C in Figure 4(c) agrees very well with the data obtained from GIXRD in Figure 4.4(d). Most diffraction spots in the SAD pattern align with the anatase diffraction rings whereas for brookite only few spots could be identified. Also, in GIXRD the peak area for the (121) diffraction peak of the brookite phase is much smaller than the peaks stemming from the anatase phase. While for the sample deposited at 200 °C no peaks of brookite could be identified, the presence of a small fraction thereof cannot be ruled out. Hence, the dominant phase for PEALD TiO_2 is anatase with a low fraction of brookite in case of a substrate temperature of 250 °C. This observation agrees very well with previous literature data.[92, 93] The areas of the anatase peaks of the sample deposited at 250 °C are larger than the peak areas for the sample deposited at 200 °C indicating that the crystalline/amorphous fraction is higher in case of a higher deposition temperature. A higher substrate temperature than 250 °C was not considered because it would not fall into the window of operation for ALD.[90]
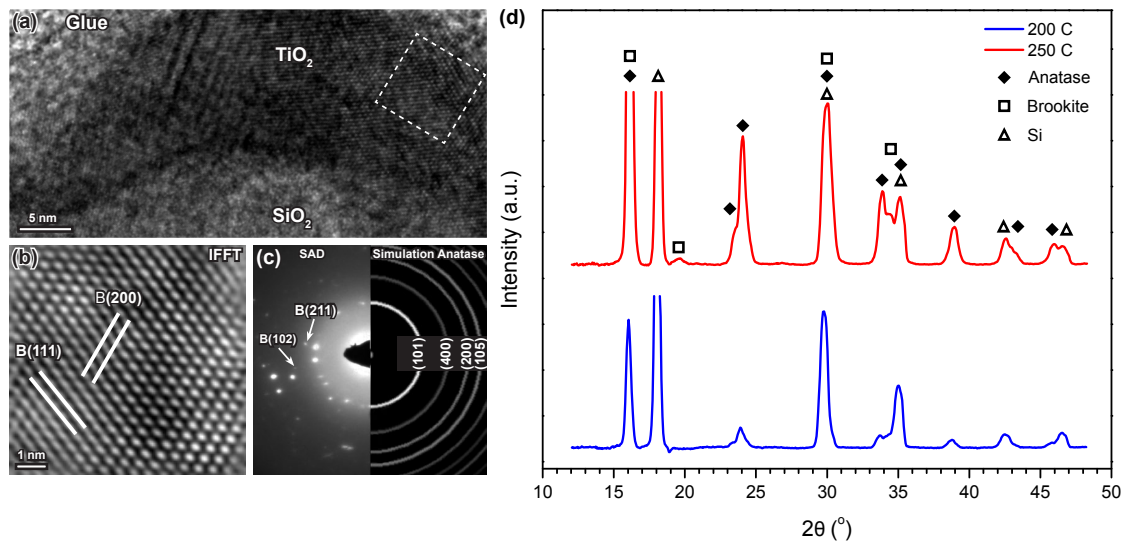
Figure 4.4.

(a) HRTEM of PEALD TiO_2 at the top of the trench substrate deposited at 250 °C and 60 s plasma exposure time. (b) IFFT of indicated area [dashed square in (a)] revealing (200) and (111) planes of the brookite phase. (c) SAD pattern in comparison with the simulated electron diffraction pattern of the anatase phase shows good agreement. The (211) and (102) diffraction spots of the brookite phase are indicated by arrows. (d) GIXRD patterns of PEALD TiO_2 films at 200 and 250 °C substrate temperature with a plasma exposure time of 60 s. The brookite (121) peak can be clearly identified for the 250 °C sample.

1.4

Conclusion

In summary, we have demonstrated that the conformal coverage of TiO$_2$ on trenches up to an AR of 1:30 can be obtained by PEALD. At a standard plasma time of 3 s during PEALD the step coverage is inferior to the step coverage of TiO$_2$ deposited by thermal ALD. We showed that for PEALD of TiO$_2$ the step coverage can be enhanced by increasing the plasma exposure time per cycle, thus approaching the high conformality achieved by thermal ALD. In addition, the step coverage improves with decreasing substrate temperature due to the temperature dependence of the recombination loss coefficient. TiO$_2$ deposited by PEALD at 200 °C is crystalline and shows the anatase phase. At a substrate temperature of 250 °C the brookite phase that is a crystalline modification of TiO$_2$ with a high dielectric constant is also present in the film as shown with GIXRD, SAD and HRTEM. Hence, morphology, crystalline modification and coverage of the TiO$_2$ layer can be controlled by the substrate temperature and the plasma duration during PEALD.

1.5

Additional Information

1.5.1 EDX Line Scans

In Figure 4.5 cross-sectional and plan view scanning TEM dark field micrographs are shown in (a) and (c), respectively. EDX line scans across the trench are indicated by an orange dotted line in the dark field image. Si, Ti and O K–edge intensity profiles are plotted in (b) and (d) in cross-sectional direction and planar direction, respectively. Intensity profiles show the same trend observed in the EDX maps in Figure 4.2.
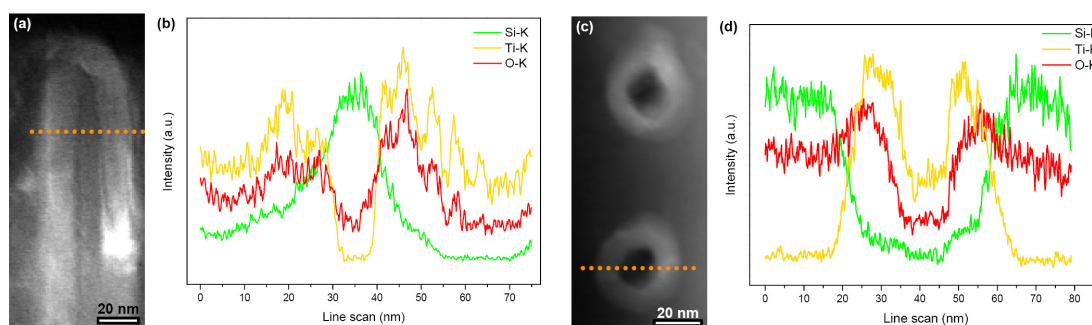
Figure 4.5.
EDX line scans in cross-sectional and plan-view of PEALD TiO$_2$ on trench substrate for the Si, Ti and O K–edges plotted in (b) and (d), respectively. Lines for the EDX scans are indicated in the STEM dark field micrographs in (a) and (c).

1.5.2 Cross-Sectional TEM of PEALD TiO$_2$ with Different Plasma Exposure Times

Figure 4.6 shows cross-sectional TEM images of PEALD TiO$_2$ deposited at 200 °C on high AR trench substrates at top and bottom for plasma exposure times 3 s, 60 s and 180 s. The thickness is indicated by a white bar and is (14.4 ± 0.7) nm, (13.0 ± 0.3) nm and (11.7 ± 0.2) nm measured at the top for the 3 s, 60 s and 180 s plasma duration sample, respectively. The thickness measured at the bottom is (12.8 ± 1.0) nm, (12.1 ± 0.7) nm and (11.2 ± 0.5) nm for the sample with 3 s, 60 s and 180 s plasma exposure time, respectively.

Figure 4.7 displays cross-sectional TEM images of PEALD TiO$_2$ deposited at 250 °C on high AR trench substrates at top and bottom for plasma exposure times 3 s, 60 s and 180 s. The indicated thickness at the top of the trench is (14.7 ± 0.5) nm, (14.1 ± 0.5) nm and (15.3 ± 0.9) nm for the 3 s, 60 s and 180 s plasma duration sample, respectively. The thickness measured at the bottom is (11.6 ± 0.4) nm, (12.0 ± 1.0) nm and (14.3 ± 0.6) nm for the sample with 3 s, 60 s and 180 s plasma exposure time, respectively. Thicknesses were averaged over 5 different positions to give an accurate value and standard deviation.
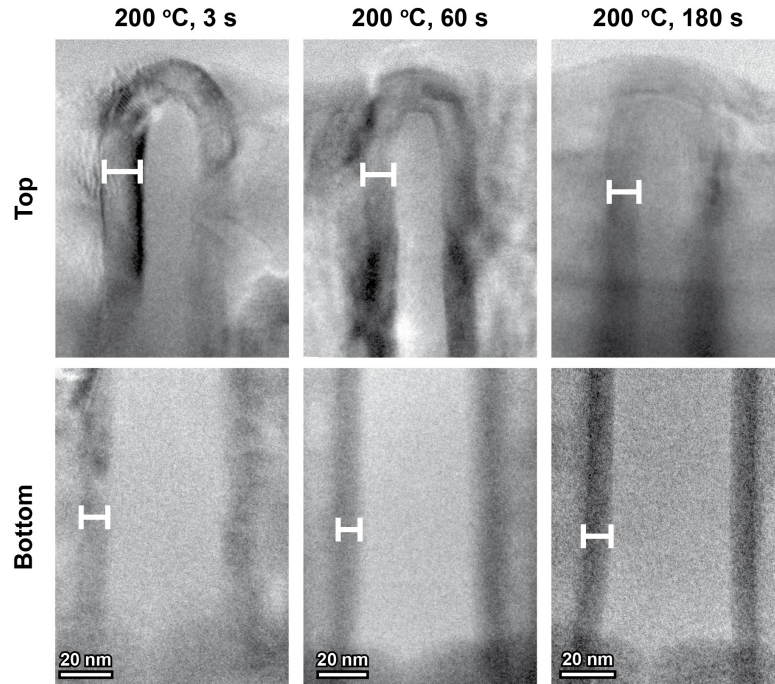
Figure 4.6.

Cross-sectional TEM micrographs for PEALD TiO$_2$ deposited at 200 °C on high aspect ratio trenches at 3 s, 60 s and 180 s plasma exposure time per cycle. Measured film thickness is indicated by a white bar.
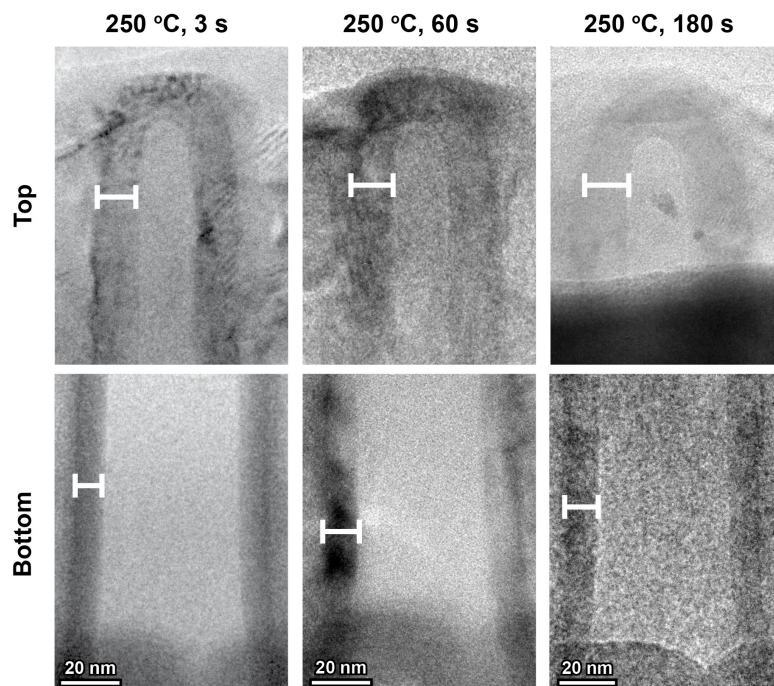
Figure 4.7.

Cross-sectional TEM micrographs for PEALD TiO$_2$ deposited at 250 °C on high aspect ratio trenches at 3 s, 60 s and 180 s plasma exposure time per cycle. Measured film thickness is indicated by a white bar.

1.5.3 Growth per Cycle as a Function of Plasma Exposure Time

The growth per cycle (GPC) of TiO$_2$ as a function of plasma exposure time per cycle deposited at 200 and 250 °C is shown in Figure 4.8. The thickness at the top was measured at 5 different positions, averaged and was divided by the number of cycles (i.e. 200) to calculate the GPC. The GPC at substrate temperature 200 °C was (0.72 ± 0.04) Å, (0.65 ± 0.01) Å and (0.59 ± 0.01) Å for 3 s, 60 s and 180 s, respectively. For TiO$_2$ deposited at 250 °C the GPC was (0.73 ± 0.02) Å, (0.70 ± 0.03) Å and (0.76 ± 0.04) Å at 3 s, 60 s and 180 s plasma exposure time per cycle, respectively. The GPC for TiO$_2$ deposited by thermal ALD at 250 °C was (0.63 ± 0.01) Å.

The GPC is slightly higher at 250 °C substrate temperature compared to 200 °C. Interestingly, the GPC for TiO$_2$ deposited at 200 °C decreases with increasing plasma exposure time per cycle. This might be explained by an increase in density as the plasma duration is extended.
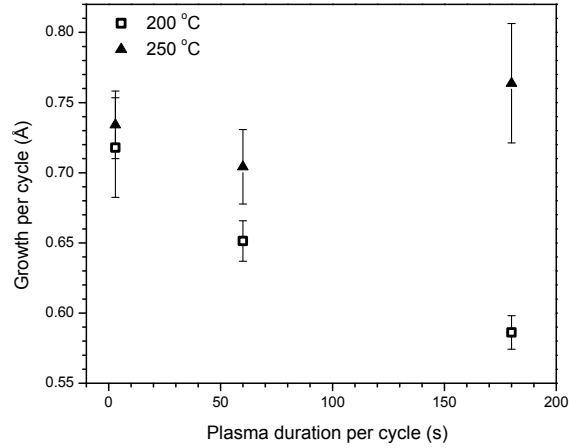
Figure 4.8.

Growth per cycle as function of plasma exposure time per cycle at 200 and 250 °C substrate temperature as calculated from the thickness measured at the top of the trench substrate. Error bars indicate standard deviation for 5 measurements.

1.5.4 Raw GIXRD areal detector data

In Figure 4.9 the raw data taken from the areal detector that was used during GIXRD synchrotron experiments are shown. The diffraction ring patterns of PEALD TiO_2 deposited at 200 °C and 250 °C are displayed in (a) and (b), respectively. Plasma exposure time per cycle for both samples was 60 s. The intensity of the diffraction rings is very uniform along the half circle indicating that there is no texture present in the PEALD TiO_2 film. For the final plot shown in main section in Figure 4.4 the intensity was integrated over the half circle and the amorphous background was subtracted.
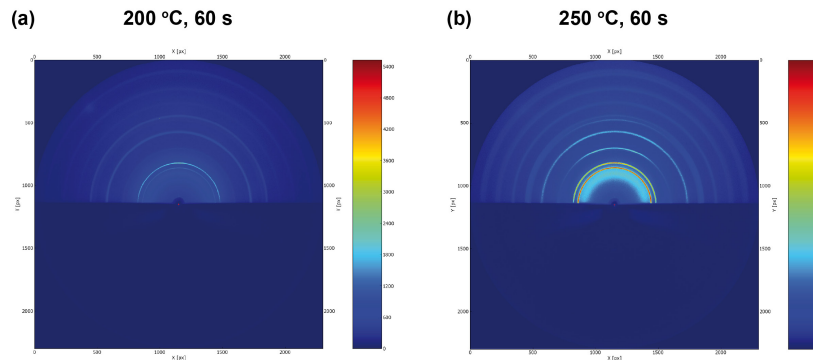
Figure 4.9.

Raw data of areal detector for GIXRD patterns of PEALD TiO_2 deposited at 200 °C and 250 °C as seen in (a) and (b), respectively. Plasma exposure time per cycle for both samples was 60 s. No texture is observed.

1.5.5 Crystallographic peak analysis of GIXRD

An overview of all peaks observed as well as the corresponding phase it originates from is summarized in Table 4.1. In detail: The peaks stemming from the underlying Si substrate are denoted by an empty triangle and are located at 18.1°, 29.8°, 35.1°, 42.2° and 46.5° for the (111), (220), (311), (400) and (331) planes, respectively. At both substrate temperatures the anatase phase peaks of TiO$_2$ (denoted by a solid rhombus symbol) are seen at 16.1°, 23.4°, 24.1°, 29.8° [overlap with Si (220) peak], 33.7°, 35.1° [overlap with Si (311) peak], 38.8°, 43.1° and 45.7° for the (101), (103), (004) [together with (112)], (200), (105), (211), (204), (220) and (215), respectively. In the sample with substrate temperature of 250 °C an additional peak for the brookite phase of TiO$_2$ (denoted by empty square) can be found at 19.6° corresponding to the (121) plane. Further brookite peaks may overlap with Si and/or anatase peaks at 16.1°, 29.8° and 34.2° for the (111), (231) and (241) planes in brookite, respectively.

Peak position [°]	Si substrate	TiO$_2$ anatase	TiO$_2$ brookite
16.1		(101)	(111)
18.1	(111)		
19.6			(121)
23.4		(103)	
24.1		(004), (112)	
29.8	(220)	(200)	(231)
33.7		(105)	
34.2			(241)
35.1	(311)	(211)	
38.8		(204)	
42.2	(400)		
43.1		(220)	
45.7		(215)	
46.5	(331)		

Table 4.1.

Summary of peaks observed in GIXRD for PEALD TiO$_2$ deposited at 250 °C and corresponding phases.

2

Crystallization of TiO$_2$ Produced by PEALD

The study on the coverage of high AR trench substrates by PEALD TiO$_2$ also indicated that not only the temperature but also the plasma exposure time have an effect on the morphology of the film. In this section, this observation is studied in more detail.

2.1

Introduction

For HfO$_2$ it was shown that depending on the type of plasma employed — remote or direct — during PEALD the deposited film turned out amorphous or poly-crystalline, respectively.[94] For Si grown by plasma-enhanced chemical vapor deposition (PECVD) a substrate DC bias influences the morphology of the film as shown by Koshku et al.[95] These observations were attributed to the fact that the energy of the incident ions or electrons facilitates the nucleation and the growth of crystallites.

Generally, crystalline TiO$_2$ exists in three polymorphic modifications — anatase, rutile, and brookite — that have different dielectric constants. Anatase has a dielectric constant of around 40 whereas rutile's dielectric constant is about 80, although there is a large variation in these values depending on synthesis method and geometry.[76–78] The brookite phase is theoretically estimated to have an even higher dielectric constant than the rutile phase.[79, 80]

For PEALD, TiO$_2$ was reported (and also observed in the previous section) to be in the anatase phase but the effect of plasma exposure time has not been studied.[96] Only after a thermal anneal at 1100 °C the film is converted into the rutile phase.[97] Furthermore, it was previously shown that PEALD TiO$_2$ exhibits a surface with lower roughness as well as a higher dielectric constant and lower leakage currents compared to TiO$_2$ deposited by thermal ALD.[98] Also, a dependence of the crystallization temperature of TiO$_2$ (in an post-deposition anneal) on the oxidation agent was found.[90] When plasma was present the crystallization temperature was reduced.

In this section we show XRD and TEM results of TiO$_2$ deposited at different plasma exposure times in the second half-step during PEALD. These results reveal that extended plasma exposure times result in a more crystalline TiO$_2$ film. Crystallization of TiO$_2$ using an extended plasma exposure is attractive due to the flexibility in substrates that can be used: They do not need to be lattice-matched, and may even be amorphous.

2.2

Experimental Methods

2.2.1 Material Fabrication

TiO$_2$ was deposited by plasma enhanced atomic layer deposition (PEALD) in a FlexAL ALD reactor (Oxford Instruments) that is equipped with a remote inductively coupled plasma generator. The base pressure of this ALD reactor is 10^{-7} Torr. The substrates were single-side polished p-doped Si wafers (sheet resistance of 0.008 $\Omega\cdot$cm, (100) oriented). Titanium-tetraisopropoxide (TTIP) and O$_2$ plasma were used as precursors. The titanium precursor was maintained at 75 °C and was pulsed for 5 s per cycle. After the TTIP exposure the chamber is purged for 60 s to remove the remaining (unreacted) precursor and the by-product resulting from the reacted ligands. As co-reactant an oxygen plasma is used generated by a remote inductively coupled plasma generator at a power of 300 W. After the plasma exposure the chamber is purged for another 60 s. Substrate temperature and plasma exposure time are varied and studied in this section.

2.2.2 Material Characterization

TEM samples were prepared as described in section 1.2.2. The morphology of the deposited TiO$_2$ thin films was examined using transmission electron microscopy (TEM, FEI Tecnai G2 F20 X–TWIN FEG, 200 kV). The crystallinity of TiO$_2$ was examined using grazing incidence X-ray diffraction (GIXRD). XRD was conducted in an X'Pert PRO diffractometer (PANalytical). Cu Kα with a wavelength of $\lambda = 1.54056$ Å and a power of 45 kV $*$ 40 mA was used as incident X-ray source. Grazing angle was set to $\omega = 1$ °. Further, synchrotron experiments were conducted at SLAC, Stanford as described in section 1.2.3.

2.3

Results and Discussion

Figure 4.10 shows GIXRD patterns of PEALD grown TiO$_2$ films deposited at three different plasma exposure times (3 s, 60 s and 180 s) for each PEALD oxidation half-cycle. These samples were approximately 20 nm thick and were deposited by 600 cycles. The diffraction peaks observed at 51° and 54° stem from the underlying Si substrate. The peaks observed at 25.3°, 37.8°, 48.4°, 55.1° and 62.7° can be attributed to the (101), (004), (200), (211) and (204) planes of the anatase phase. Crystalline peaks for the 60 s sample appear to be sharper and an additional peak is observed at 36.2° that either may be attributed to (101) planes of the rutile phase or (012) planes of the brookite phase. In the 180 s sample this specific peak shows up as a shoulder of the neighboring (004) peak of anatase. The sample deposited with 3 s plasma exposure time shows no crystalline peaks.

Hence, the dominant phase for PEALD TiO_2 is anatase with a low fraction of brookite (and/or rutile) in case of a substrate temperature of 250 °C and a plasma exposure time of 60 and 180 s. This observation agrees very well with previous literature data.[92, 93] The sample deposited with 3 s plasma exposure time turned out to be amorphous.
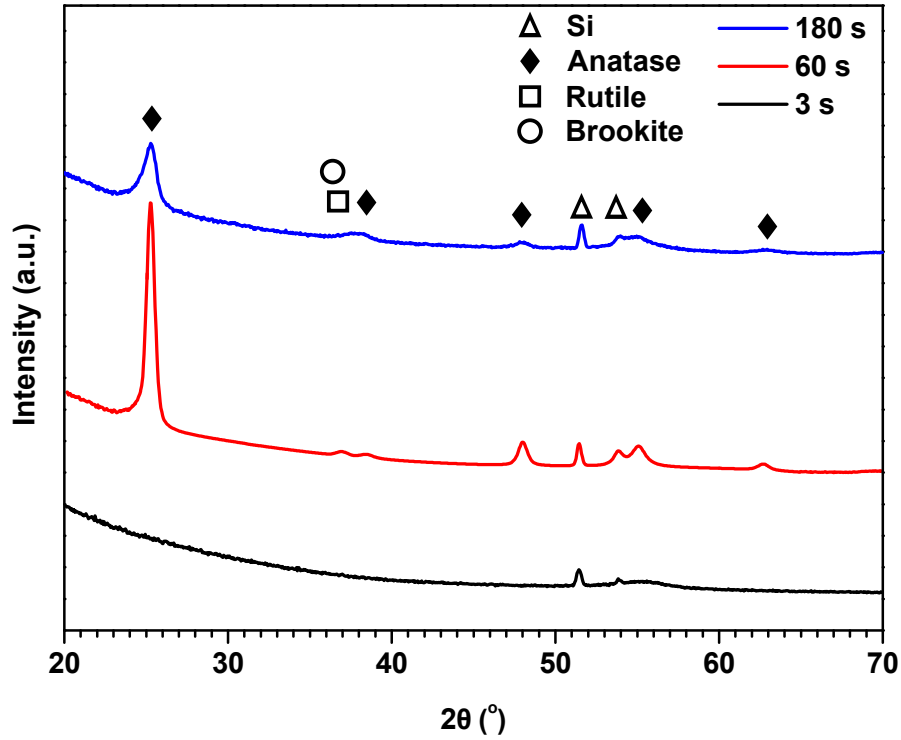
Figure 4.10.

GIXRD patterns of TiO_2 on planar Si substrates deposited at 250 °C with varied plasma exposure times 3 s, 60 s and 180 s for each cycle.

To get further inside, synchrotron measurements were performed to analyze the phases of PEALD TiO_2 at different substrate temperatures as well as plasma exposure times. Figure 4.11 displays the raw data obtained from the areal detector from the GIXRD experiments. Crystalline diffraction rings are observed at (b) and (c) (corresponding to 250 °C and 60 s and 180 s plasma exposure time, respectively) indicating that there's no texture present in the film. The dots with high intensity stem from the underlying Si substrate.

The lack of texture in the deposited film is expected due to the amorphous nature of the native SiO_2 on the crystalline Si substrate.

(a)   **150 °C, 60 s**   **(b)**   **250 °C, 3 s**

(c)   **250 °C, 60 s**   **(d)**   **250 °C, 180 s**
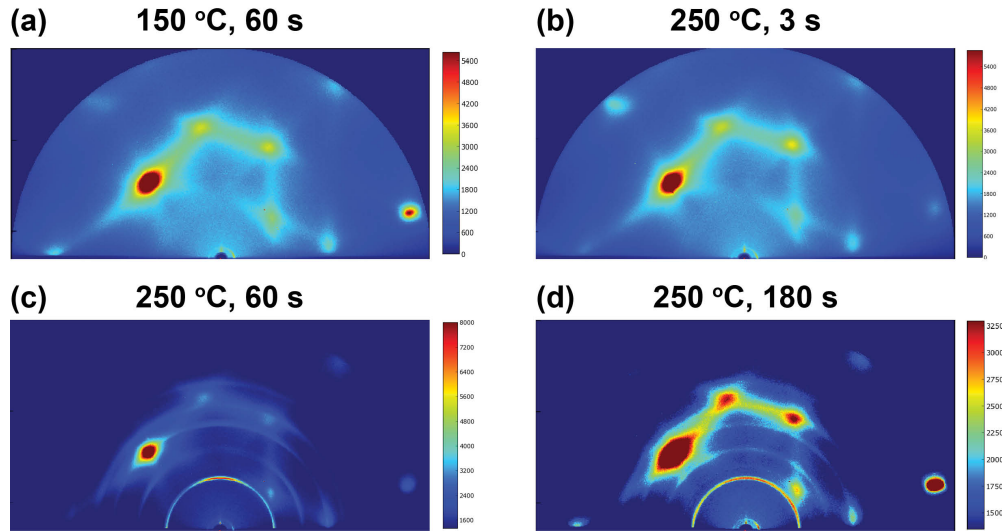
Figure 4.11.

Areal detector raw data from GIXRD experiments using synchrotron radiation of samples of PEALD TiO$_2$ is shown. (a) for TiO$_2$ deposited at 150 °C and 60 s plasma exposure time per cycle. (b), (c) & (d) correspond to TiO$_2$ films deposited at 250 °C with 3 s, 60 s and 180 s plasma exposure time, respectively.
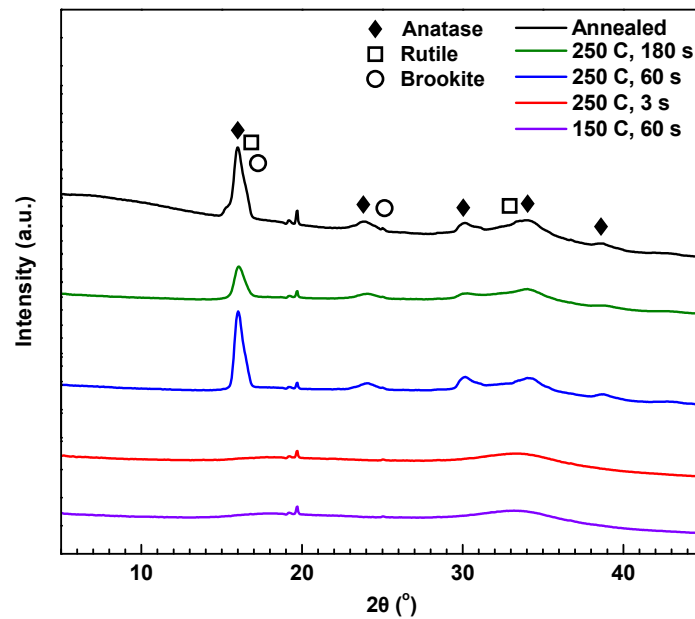
Figure 4.12.

Synchrotron GIXRD patterns of TiO$_2$ deposited on planar Si substrates by PEALD at 150 °C with a 60 s plasma exposure time and at 250 °C with a 3 s, 60 s and 180 s plasma exposure time. For comparison a TiO$_2$ sample annealed at 1000 °C is shown as well.

To obtain intensity–2θ plots the raw data was integrated radially and a line profiles of segments were taken that do not contain peaks/streaks from the underlying Si substrate. The final plots are displayed in Figure 4.12. In addition to the previous three samples grown at 250 °C an additional sample was investigated at 150 °C and a reference sample was used that has been annealed at 1000 °C. Peaks stemming from the anatase phase can be observed for the samples deposited at 250 °C with a 60 s and 180 s plasma exposure time (as well as for the control sample) at 15.9°, 23.7°, 30.0°, 34.1° and 38.5° for the (101), (004), (200), (211) and (204) planes, respectively. Both rutile and brookite have their strongest peak at almost the same location as the (101) peak of anatase and hence are not clearly distinguishable. Rutile has one additional peak at 33.6° for the (211) plane that shows up as a shoulder of the (211) peak of the anatase phase. An additional brookite peak can be observed at 25.1° corresponding to the (022) plane.

These results are consistent with the observed patterns in Figure 4.10 and further show that there's no texture in the film and that at 60 s plasma exposure time the TiO_2 film turns out to be crystalline at 250 °C but amorphous at 150 °C.

To further corroborate the results, cross-sectional TEM samples were investigated as shown in Figure 4.13. The TEM micrographs depicted in Figure 4.13(a)–(c) show PEALD TiO_2 deposited at 250 °C with a plasma exposure time of 3 s, 60 s and 180 s, respectively. Crystalline fringes can be observed in the latter two cases but the sample at 3 s plasma exposure time appears to be amorphous.

The TEM observation confirms the results obtained by GIXRD and shows a dependence of crystallization on the plasma exposure time.
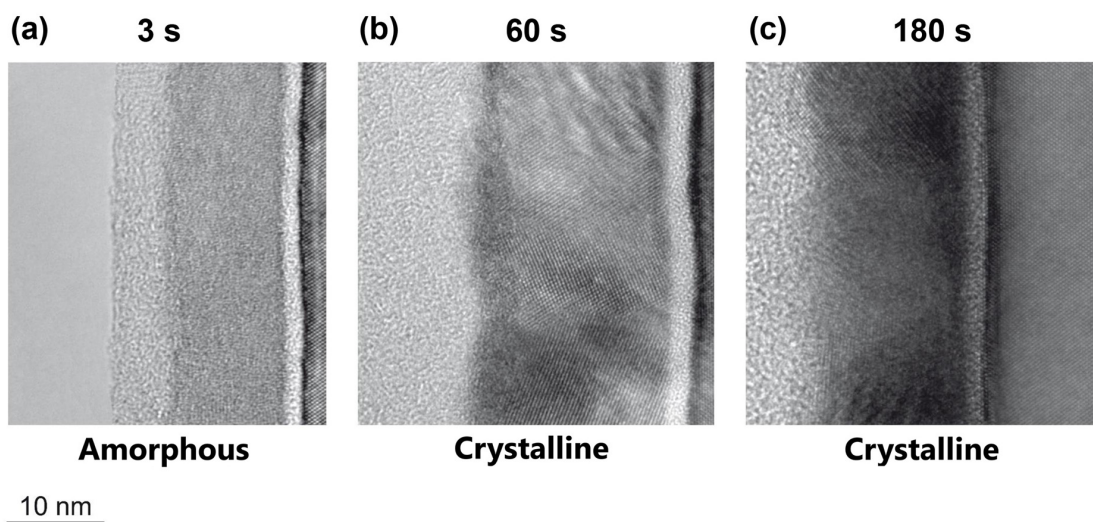
Figure 4.13.

TEM micrographs of PEALD TiO_2 deposited at 250 °C with a plasma exposure time of 3 s, 60 s and 180 s are shown in (a), (b) and (c), respectively. In (a) amorphous contrast is observed whereas for (b) and (c) crystalline fringes can be seen.

2.4

Conclusion

In summary, we have demonstrated the effect of plasma exposure time for the second PEALD oxidation half-step on the crystalline structure of a PEALD TiO$_2$ film. At 250 °C deposition temperature and 3 s plasma exposure time the sample is in its amorphous phase whereas at 60 and 180 s the film turns out to be crystalline. The crystalline modification of the TiO$_2$ film is mainly anatase with a low fraction of either brookite and/or rutile. For further studies temperatures between 150 ° and 250 °C will be of interest. From an application standpoint this result is very promising because it reveals another process parameter for tuning structural, morphological (and hence electronic) properties.

3

PEALD of BaTiO$_3$

After studying PEALD of TiO$_2$ in-depth with regard to its morphology and step-coverage we moved on to the more complex ternary system BaTiO$_3$ (BTO). While BTO was deposited by ALD in the past,[14] its deposition by PEALD has not been reported to our knowledge and hence its benefits are worth exploring. The implications of PEALD BTO on future applications for DRAM, we believe, are significant.

3.1

Introduction

The use of high–k thin films that exhibit a low leakage current is essential in realizing DRAM capacitors with high charge storage density and long storage lifetime.[22, 72] Among high–k thin films, perovskites such as BTO, SrTiO$_3$ (STO), or (Ba,Sr)TiO$_3$ (BST) are attractive candidates due to their exceptionally high dielectric constants maintained even for thin films ($>$100).[14, 15, 20–22, 99] Recent development of DRAM have also necessitated the down-scaling of features to smaller dimensions ($<$ 30 nm), i.e. higher ARs, for enhanced information storage densities. Therefore, the conformal coating of high–k thin films over the inner surface of high AR trenches is of great importance. In this regard, ALD, which is dominated by unique self-limiting surface reactions, is an attractive tool to fabricate DRAM capacitors. ALD enables the deposition of conformal films over complex 3-dimensional geometries with precise thickness control. Additionally, one can minimize the thermal damage of the device in the process of the deposition due to the relatively low process temperature ($<$ 400 °C) during ALD.[45] PEALD, in which excited species (such as ions and radicals) generated by a plasma are used to react with ligands of the precursor during the second half-step, has several advantages compared to the conventional thermal ALD;[100] for example, the highly reactive plasma species give more flexibility in processing conditions and materials properties. PEALD films are also known to possess higher density and less contamination originated from unreacted ligands, which potentially results in the lowered electrical leakage current of dielectric oxide films.[100]

In this section, we demonstrate for the first time the successful deposition of PEALD BTO films using cyclopentadienyl(Cp*)-type barium precursor, Ba(^{i}Pr$_3$Cp*)$_2$ (^{i}Pr$_3$Cp* = 1,2,4–trisisopropyl–cyclopentadienyl). The growth behaviors of the individual oxides (i.e., BaO and TiO$_2$) and of BaTiO$_3$ have been tested and the ALD growth-mode was confirmed. The detailed compositional, morphological, and crystallographic characteristics of the PEALD BTO are presented, and compared to those of thermal ALD BTO films previously reported.[18] PEALD of BTO films showed to result in more uniform and denser films with more crystallites dispersed in the amorphous BTO matrix, compared to thermal ALD BTO. Lastly, the electrical performance of PEALD BTO films is shown as a function of Ba–to–Ti cation ratio for the possible application in charge storage capacitors.

3.2

Experimental Methods

3.2.1 Material Fabrication

BTO films were deposited in a commercial PEALD reactor (FlexAl, Oxford Instruments). Ba(^{i}Pr$_3$Cp)$_2$ (Air Liquide) and Ti(OCH(CH$_3$)$_2$)$_4$ (TTIP, Sigma Aldrich) were utilized as the Ba and Ti precursors, respectively. The precursor canisters of the Ba and Ti precursors were heated to 180 and 55 °C, respectively. Oxygen plasma was generated from an inductively coupled plasma system (plasma power, 250 W; operating pressure, 15 mTorr). The BaO PEALD process consisted of i) Ba precursor injection (3 s) followed by ii) Ba precursor exposure (60 s) to enhance diffusion and adsorption of the precursor molecules, iii) precursor purging by Ar (60 s), iv) plasma stabilization (2 s), v) O$_2$ plasma injection (10 s) and vi) Ar purging (2 s). In case of the TiO$_2$ PEALD process, i) TTIP injection (5 s), ii) precursor purging by Ar (5 s), iii) plasma stabilization (2 s), iv) O$_2$ plasma injection (3 s) and v) Ar purging (2 s) were employed. The BTO films with different cation composition ratios ([Ti]/([Ba]+[Ti]) = 0.26–0.76) were fabricated by alternately depositing one BaO cycle and several TiO$_2$ cycles, which together form one super-cycle.

3.2.2 Material Characterization

The film thickness (d_{BTO}), roughness and density were measured by X-ray reflectivity (XRR) measurements (X'Pert Pro, PANalytical). The film thickness was also confirmed by a spectroscopic ellipsometer (Woollam M2000). High-resolution transmission electron microscopy (HRTEM) at an acceleration voltage of 300 kV was employed to analyze the crystallization of the samples (FEI Titan ETEM 300 kV). TEM sample preparation is described in section 1.2.2. The composition analysis was conducted by X-ray photoelectron spectroscopy (XPS, PHI VersaProbe Scanning XPS Microscope) with Al (Kα) radiation (1486 eV). Atomic force microscopy (AFM, JEOL 5200) was used to characterize the surface morphology of the films. For the electrical measurement, Pt/BTO/p-doped Si metal–insulator–semiconductor capacitors were fabricated using highly p-doped Si wafers (a sheet resistance of 0.008 Ω·cm) as substrates and a DC-sputtered Pt (200 nm) film as the top electrode. The electrical properties, i) capacitance at 1 kHz and ii) current density–voltage (J–V) curves (0 to +2 V) were measured by an LCR meter (Agilent, model no. E4980A) and a Keithley SourceMeter (2636A), respectively. The detailed process to obtain dielectric constants of BTO (ϵ_{BTO}) as well as the equivalent oxide thickness (EOT), i.e. $d_{\text{BTO}}(3.9/\epsilon_{\text{BTO}})$, were reported at **[10, 18, 27]**.

3.3

Results and Discussion

We first investigated the basic ALD characteristics of the individual oxides BaO and TiO$_2$ in order to be able to deposit stoichiometric BTO. Figure 4.14(a) and Figure 4.14(b) show the growth per cycle (GPC) of BaO as a function of substrate temperature (200–350 °C) and Ba precursor pulse time, respectively. The GPC of PEALD BaO in the range of 250–300 °C was nearly constant at 0.25–0.26 nm/cycle with 4–7 % non-uniformity on a 4-inch wafer. Furthermore, the GPC values of PEALD BaO at 250 °C were saturated with a precursor pulse time longer than 3 s. However, the GPC of BaO was significantly increased to 7.60 ± 0.02 nm/cycle at 350 °C. Similarly, the measured GPC values of PEALD TiO$_2$ were ~0.045 nm/cycle with 2 % non-uniformity at substrate temperatures of 200–300 °C (Figure 4.14(c)). Further, the GPC of PEALD TiO$_2$ showed to be saturated with a precursor pulse time greater than 3 s as seen in Figure 4.14(d).

The saturation of the GPC with increasing precursor pulse time (in the range of 250–300 °C) implies that the deposition of BaO using Ba(^{i}Pr$_3$Cp)$_2$ and O$_2$ plasma lies within the ALD window. The high GPC even at a relatively low deposition temperature (250 °C) clearly shows the benefit of using oxygen plasma as an oxidant over water or ozone. Furthermore, the deposition at 250 °C is appropriate to sustain thermal stability of the Ti-alkoxide-type precursor, TTIP, important for TiO$_2$ ALD growth.[26] The significant increase in GPC of BaO at 350 °C may be ascribed to the partial decomposition of Ba(^{i}Pr$_3$Cp)$_2$ to smaller alkyl-substituted Cp* complexes.[22] Lee et al.[22, 26] also reported the chemical vapor deposition like growth of SrO when Sr(^{i}Pr$_3$Cp)$_2$ was initially supplied to fresh substrates which readily provide oxygen (e.g. IrO$_2$ and RuO$_2$). Hence, these substrates show to be unfavorable for depositing films with a uniform Ba–to–Ti ratio in the direction of growth. In our work, this is not the case due to higher bond dissociation energies of Si–O and Ti–O bonds over the Ba–O bond (bond dissociation energies Hf$_{298}$ (kJ/mol); Si–O: 798; Ti–O: 662; Ba–O: 563).[101] The observed GPC values of TiO$_2$ are consistent with the previously reported GPC values, 0.04–0.05 nm/cycle at similar deposition conditions.[90] These results imply that the ALD mode deposition of BTO, which is fabricated by repeating BaO and TiO$_2$ layers alternately, is possible at the temperature range where both of them show a constant GPC, i.e. 250–300 °C.
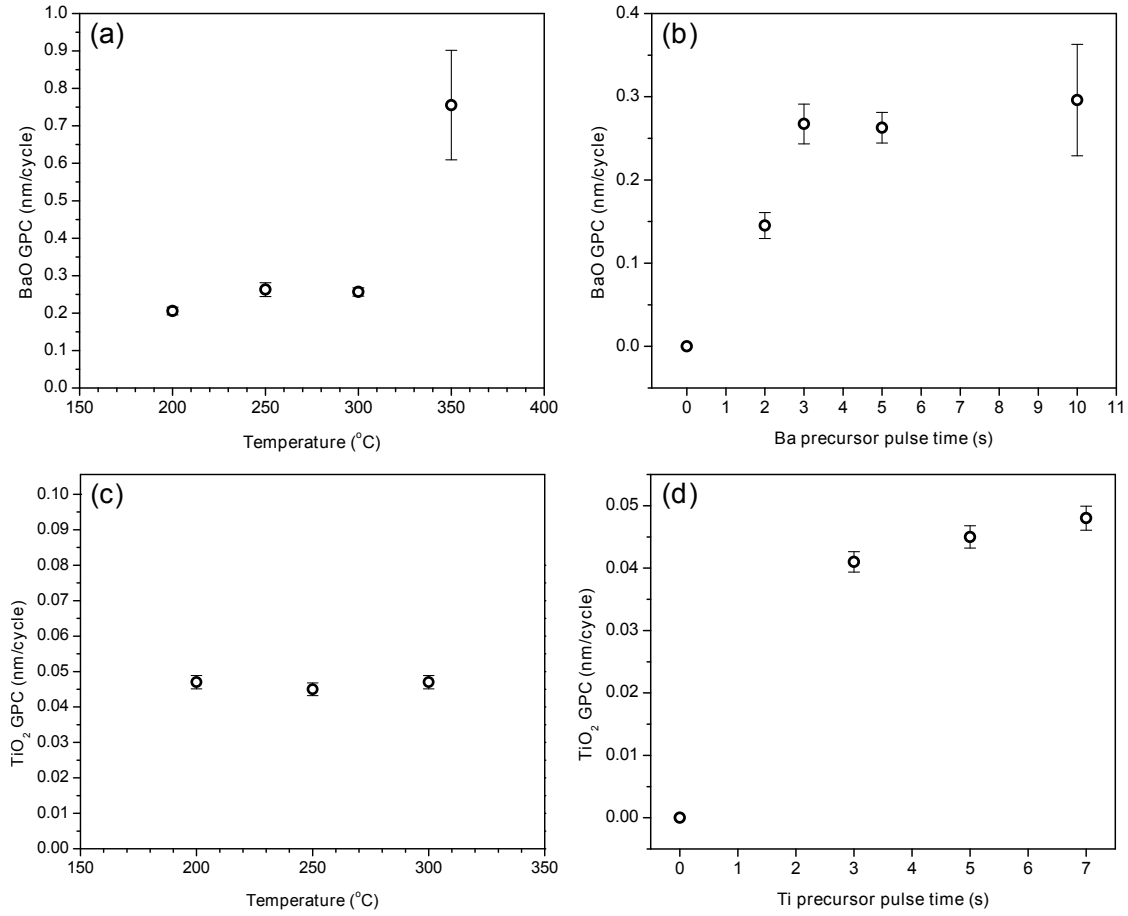
Figure 4.14.

GPC of BaO as a function of (a) substrate temperature (with the precursor pulse time of 3 s) and (b) Ba precursor pulse time (with the substrate temperature of 250 °C). GPC of TiO$_2$ as a function of (c) substrate temperature (with precursor pulse time of 5 s) and (d) Ti precursor pulse time (with a substrate temperature of 250 °C). Error bars indicate standard deviations obtained by 5 measurements.

Figure 4.15(a) shows the cation ratio [Ti]/([Ba]+[Ti]) inside the film depending on the ALD cycle ratio (i.e., the number of TiO$_2$ cycles per one BaO cycle). The cation ratios were controllable by simply changing the Ba:Ti cycle ratio. The film becomes slightly Ba-rich ([Ti]/([Ba]+[Ti]=0.48) when the Ba:Ti cycle ratio is 1:1, and becomes slightly Ti-rich ([Ti]/([Ba]+[Ti]=0.52) when the cycle ratio is 1:2. Figure 4.15(b) shows the GPC versus the Ba:Ti cycle ratio. The GPC per super-cycle is increased with increasing number of Ti cycles, however, the GPC per individual ALD cycle is monotonically decreased due to the small GPC of TiO$_2$ over BaO. At the Ba:Ti cycle ratio of 1:3, for example, the growth per individual cycle is measured to be 0.065 nm/cycle while the growth per super-cycle is 0.26 nm/cycle. At this deposition condition, the thickness of the BTO film increases linearly with increasing number of individual cycles (Figure 4.15(c)).
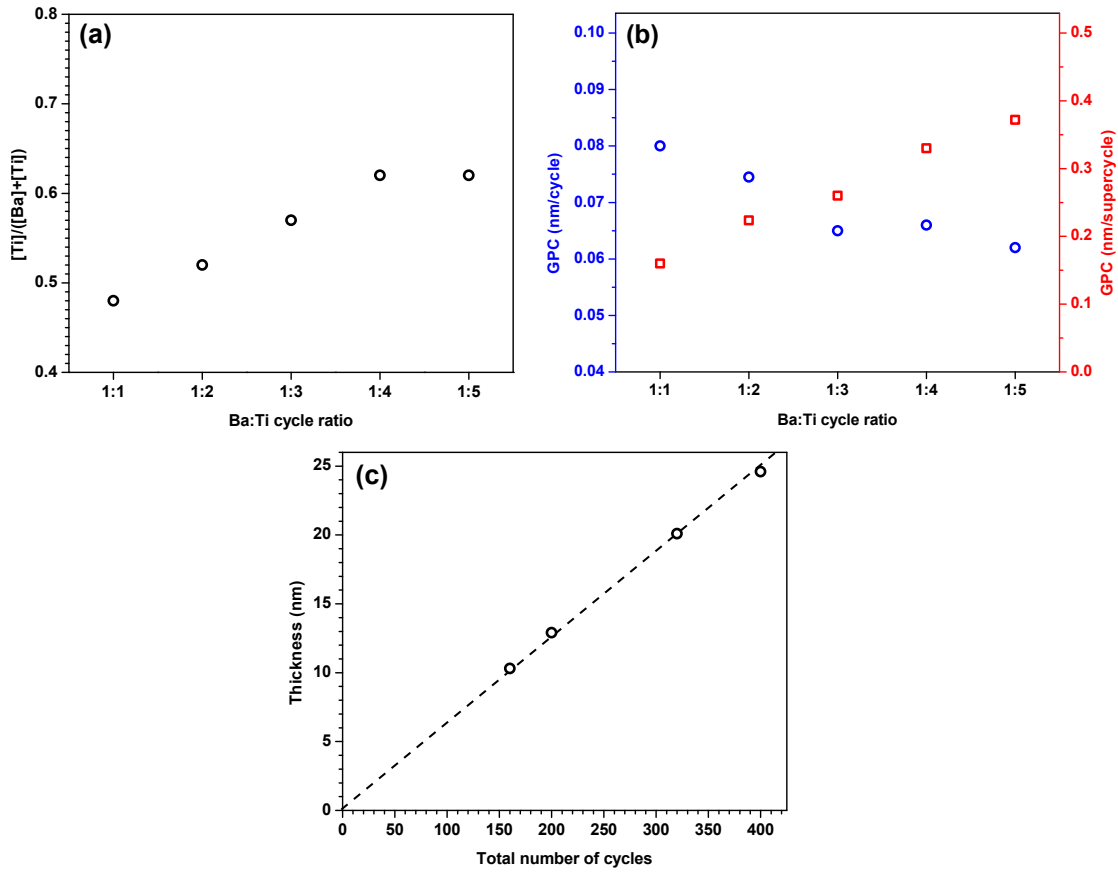
Figure 4.15.

(a) Composition ratio ([Ti]/([Ba]+[Ti])) and (b) GPC (blue: per individual cycles, red: per super-cycle) vs. Ba:Ti cycle ratio. (c) Thickness of the BTO film vs. total number of individual ALD cycles for BTO with a Ba:Ti cycle ratio of 1:3.

We investigated the compositional, morphological and crystallographic properties of PEALD BTO (Ba:Ti cycle ratio of 1:3) deposited at 250 °C. Figure 4.16 shows the XPS depth profile of a slightly Ti-rich BTO film with a cation ratio [Ti]/([Ba]+[Ti]) of 0.52 being uniform throughout the whole thickness ($\sim$12 nm). The carbon content was below the detection limit of XPS ($<$ 1 at%) except for the top-most surface ($<$ 2 nm) coming from the surface contamination. Surface morphology analysis by AFM (Figure 4.17(a)) showed a root mean square roughness of 0.40 nm. Figure 4.17(b) displays a cross-sectional TEM image of as-deposited PEALD BTO revealing small crystallites embedded in the amorphous matrix. The inset shows lattice spacings of 0.2 nm in agreement with (100) directions of cubic (a 0.394–0.403 nm), tetragonal (a 0.394–0.399 nm, c 0.399–0.404 nm), or rhombohedral (a 0.400 nm, θ 89.5°) BTO.[102] A high film density of 5.0 g/cm^3 is measured by XRR for as-deposited PEALD BTO (data can be seen in Figure 4.20 in the additional information section).

The XPS result shows that the ligand exchange reaction between the Ba and Ti precursors with the O$_2$ plasma (forming Ba–O and Ti–O bonds) occurs without the formation of any carbonate species which was also observed by Lee et al. for thermal ALD STO deposited on a Ru substrate.[22] The roughness measured by AFM for PEALD BTO is smaller than that of thermal ALD BTO (0.63 nm) with a similar thickness.[18] One possible explanation for this is that the incident plasma species with an ion energy of ~20 eV effectively migrate surface atoms into sites with a high surface energy, eventually resulting in the lowered roughness without damaging the surface, supported by Takagi et al.[103] As-deposited PEALD BTO shows 1–2 nm sized crystallites embedded in the amorphous matrix whereas thermal BTO appears to be completely amorphous.[18] Note that the crystallinity of as-deposited thermal ALD BTO films can be enhanced after being post-treated by an O$_2$ plasma presumably due to the ion bombardment at the surface, providing the required energy for atomic rearrangement.[18] Similarly, during the deposition of PEALD BTO, O$_2$ plasma species with the primary object of oxidizing precursors activated the BTO film to be partly crystallized. Further, XRR showed that the density of PEALD BTO is significantly higher compared to thermal ALD BTO (3.3 g/cm^3),[18] which further confirms the partial crystallization of the film (the density of amorphous BTO: 4.3 g/cm^3; polycrystalline BTO: 5.61 g/cm^3).[104]
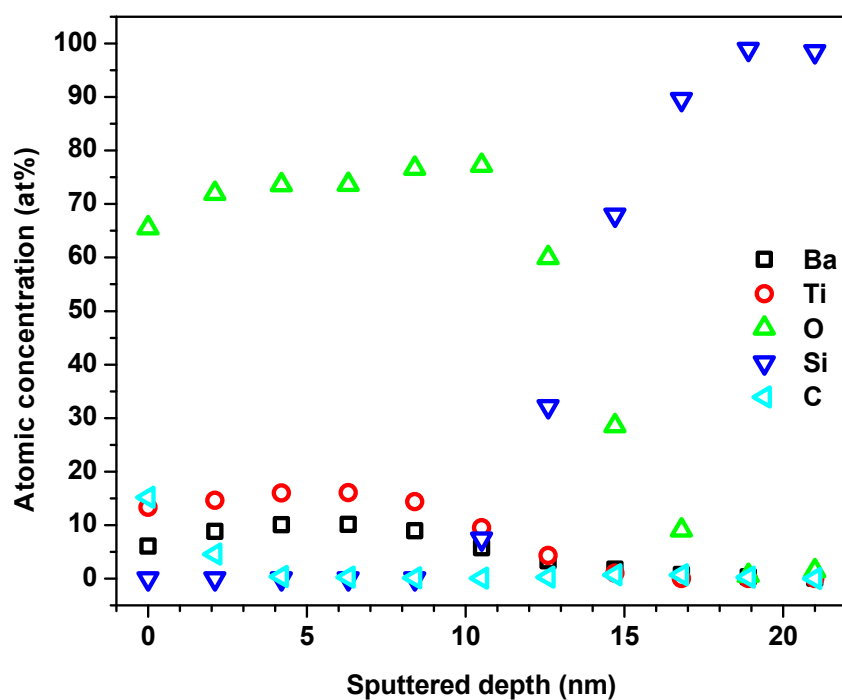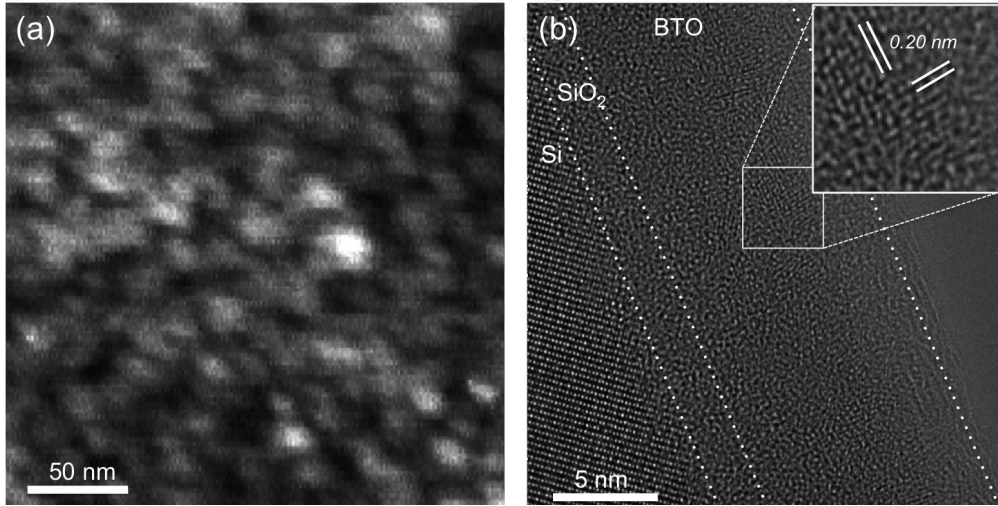

Figure 4.16.
XPS depth profile spectra of 12 nm-thick BTO (Ba:Ti cycle ratio of 1:3) deposited at 250 °C. Sputtering depth was calculated from sputtering time with the assumption of a sputtering rate of 7 nm/min.

Figure 4.17.

(a) AFM topography image and (b) High resolution TEM image of an as-deposited 12 nm thick BTO film (Ba:Ti cycle ratio of 1:3) deposited at 250 °C. The inset in (b) shows a zoomed-in view of the BTO film revealing crystalline lattice fringes (d_{100} of cubic BTO = 0.200 nm).

The electrical properties of PEALD BTO showed a strong dependence upon the Ba–to–Ti cation ratio ($[Ti]/([Ba]+[Ti])$). As shown in Figure 4.18(a), the EOT shows a minimum, i.e., the dielectric constant shows a maximum, at $[Ti]/([Ba]+[Ti]) \sim 0.55$–0.6. The leakage current density at +1.6 V (electron is injected from the bottom electrode into the BTO film), becomes larger at a higher $[Ti]/([Ba]+[Ti])$: the current density is steeply increased by four orders of magnitude between the $[Ti]/([Ba]+[Ti])$ cation ratios 0.46 and 0.57.

A similar trend observed for the dielectric constant of BTO was reported for ALD STO films, which also achieved the maximum dielectric constant of 90 at $[Ti]/([Sr]+[Ti])$ of 0.49 (the Sr:Ti cycle ratio of 1:3) where the strongest diffraction peaks (corresponding to the STO perovskite structure) were observed.[22] We hypothesize the enhanced crystallization of the BaO/TiO$_2$ mixture at such composition ratios may have resulted in the lowered EOT. For inorganic materials, the maximum nucleation temperature (T_n) and the maximum crystal growth temperature (T_g) is roughly proportional to the melting point (T_m) of the material ($T_n = 0.56 \cdot T_m$; $T_g = 0.94 \cdot T_m$).[105] Interestingly, the melting point of a BaO/TiO$_2$ mixture at $[Ti]/([Ba]+[Ti]) \sim 0.6$ was reported to be the lowest (1375 °C), presumably resulting in a higher fraction of crystallization compared to other stoichiometries (cf. Figure 4.21 in the additional information section). One of the possible reasons for the increased leakage current with a higher Ti content may be the fact that TiO$_2$ has a lower band gap than BaO. The band gaps of bulk TiO$_2$ and BaO are known to be 2.04 eV and 5.2 eV, respectively.[106] The lower band gap of TiO$_2$ compared to BaO may cause a smaller barrier height for the electrons flowing from the top electrode trough the dielectric layer in the case of BTO films with a higher Ti content. The current density vs. applied voltage (J–V) plot of the BTO films with

different stoichiometries are displayed in the additional information section in Figure 4.22. The differences in shape and slope of the J–V curves for different stoichiometries may be ascribed to different tunneling mechanisms being prevalent. More detailed analyses regarding the leakage mechanism in PEALD BTO are currently under investigation.
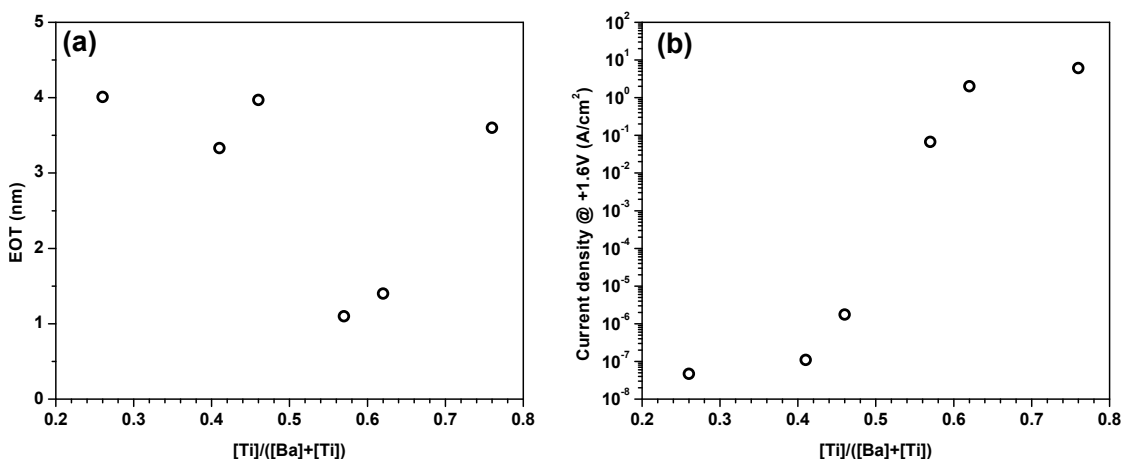
Figure 4.18.

Electrical properties of an as-deposited 12 nm thick BTO film deposited at 250 °C: (a) EOT and (b) Leakage current density (at +1.6 V) vs. [Ti]/([Ba]+[Ti]) ratio are plotted.

Figure 4.19 shows cross-sectional TEM images taken of 80 super-cycles BTO deposited on the high AR trench substrate by PEALD. At the very top of the trench (Figure 4.19(a)) the deposition profile is mushroom–shaped with the thickness falling off from 18 to 13 nm. Going further down into the trench as seen in Figure 4.19(b) the thickness reduces further to 4 nm. At the very bottom the thickness is measured to be 3.5 nm, as shown in (c). This gives a step-coverage of only around 20 % for an AR of 1:30.

The poor step-coverage indicates that the precursor is close to the limit of its ALD window and it the precursor molecules appear not to be stable enough to diffuse down the high AR trench substrate. There is a possibility that there is a CVD component to the reaction of this precursor with the surface during PEALD. Hence, in future work developing new precursors that are stable for high AR coverage will be of importance.
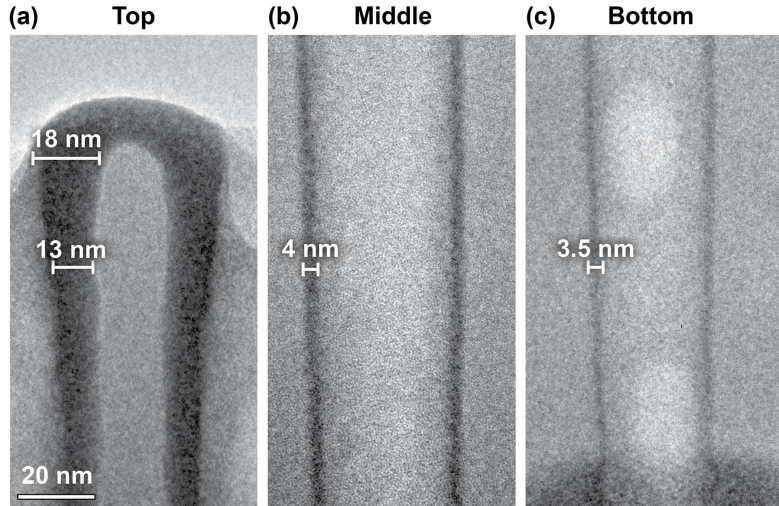
Figure 4.19.

Cross-sectional TEM of 80 super-cycles of BTO deposited on high AR trenches by PEALD shown at the top (a), middle (b) and bottom (c) of the trenches. Thicknesses are indicated.

3.4

Conclusion

For the first time, we have successfully demonstrated the ALD-mode deposition of BTO using plasma-enhanced ALD, and characterized the physical, chemical and electrical properties of the film. The improvement in crystallinity and density of the film was clearly observed when the oxygen plasma was used as an oxidizing agent instead of water. The correlation of electrical properties with Ba–to–Ti cycle ratio was also elucidated. We showed that the slightly Ti-rich BTO ($[Ti]/([Ba]+[Ti])\sim0.55$–0.6) has the lowest EOT while Ba-rich films ($([Ti]/([Ba]+[Ti]) < 0.4$) show the lowest leakage current. The first successful demonstration of PEALD BTO thin films presented in this study may be the stepping-stone to the emergence of next generation DRAMs and novel energy storage devices with a ultra-high charge/energy storage density.

3.5

Additional Information

To ease the reading flow of the main section, three additional figures are listed here:
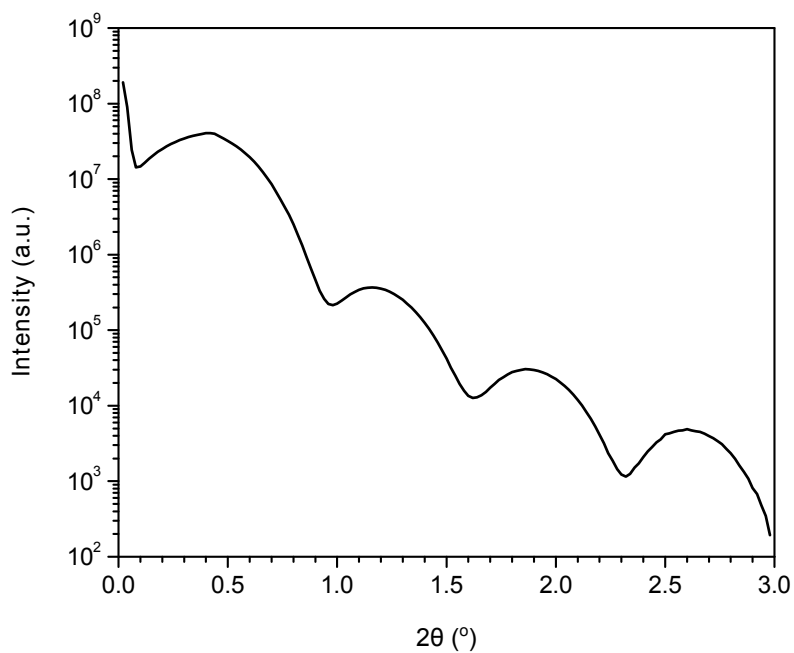
Figure 4.20.

XRR data of BTO by PEALD. Fit yields a density value of 5.0 g/cm^3.
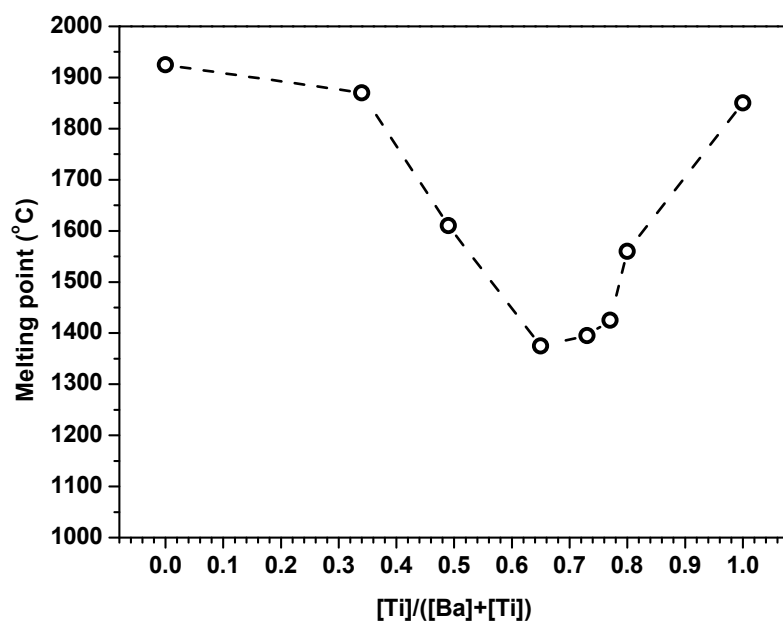
Figure 4.21.

Melting points of the BaO–TiO$_2$ system depending on [Ti]/([Ba]+[Ti]). At [Ti]/([Ba]+[Ti]) = 67 %, the melting point showed the lowest value 1375 °C. Data taken from **[107]**.
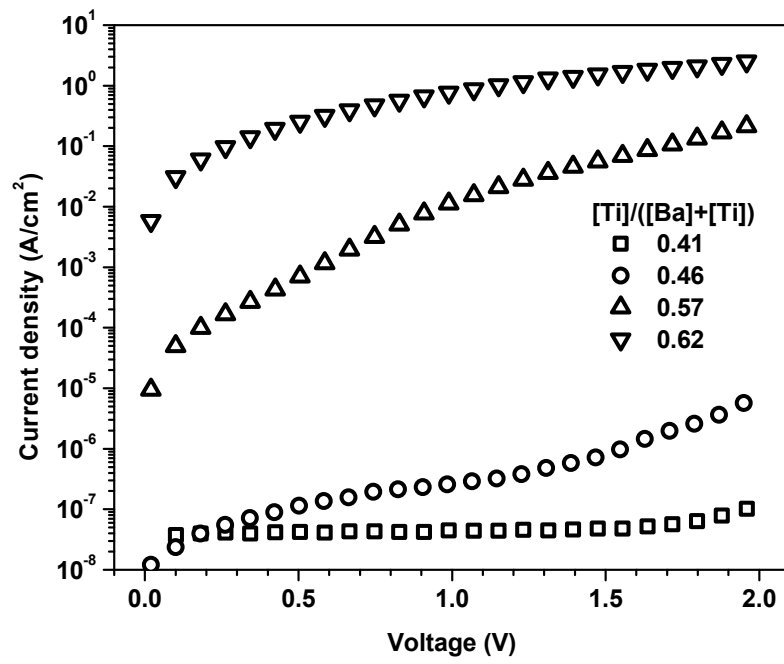
Figure 4.22.

The current density vs. applied voltage (J–V) plot of the BTO films with different stoichiometries.

<div style="border:1px solid black; padding:10px;">

4

Crystallization of PEALD BaTiO$_3$

</div>

Similarly, like we studied the effect of plasma time on the morphology and crystallization of TiO$_2$ we investigated this same effect for BaTiO$_3$.

4.1

Introduction

For many materials grown by ALD the resulting structure is amorphous due to the low process temperature. Materials in their amorphous state tend to have much lower dielectric constants than their crystalline counterparts. Hence, especially for perovskite structures such as BaTiO$_3$ (BTO) which have ultra-high dielectric constants in their crystalline structure it is of interest to find ways of crystallizing the amorphous as-deposited (PE)ALD film. Therefore, various in-situ or ex-situ techniques such as seed-layering[26] or thermal annealing[15] have been used for crystallizing the ALD film. These techniques, however, often need a higher process temperature (>500 °C) than acceptable for DRAMs.

Crystallization by facilitating a plasma is advantageous because it does not require elevated temperatures. Instead the film is crystallized by the kinetic energy of ions and radicals transferred to the surface of the deposited film.[108] Crystallization can be facilitated more easily in-situ for direct plasmas but this may also be damaging the deposited film.[94] For remote plasmas the plasma source is located further away from the substrate and hence reduces the flux of ions and therefore also minimizes the damage inflicted on the film. However, due to the low ion density it is more challenging to crystallize the film by a remote plasma.[94, 108]

For thermal ALD of BTO a post-plasma treatment using a remote oxygen plasma showed to improve crystallinity and density.[18] For PEALD BTO the effect of a post-treatment on these properties has been unexplored to date.

In this section a TEM study of as-deposited (short and long in-cycle plasma exposure times) and oxygen plasma exposure (PE) post-treatments of PEALD BTO is reported. HRTEM shows the crystalline fraction as well as the location where crystallization is occurring for the different plasma exposure samples. AFM, XRR and XPS are conducted to gain further insights into the properties of PEALD BTO such as density, roughness and oxygen content in the film.

4.2

Experimental Methods

4.2.1 Material Fabrication

The fabrication process of PEALD BTO films was described in section 3.2.1. One super-cycle (SC) for the PEALD process for BTO is composed of one sub-cycle of BaO deposition and three sub-cycles of TiO deposition. XPS analysis showed slightly Ti-rich BTO with a cation ratio $[Ti]/([Ba]+[Ti]) = 0.6$.

Oxygen plasma for both Ba and Ti was generated from inductively-couple plasma (ICP) generator (plasma power 250 W, plasma pressure 15 mTorr). To modulate the degree of crystallization in the BTO films, O_2 plasma treatment condition has been modified in two manners: i) PEALD with prolonged in-cycle plasma and ii) PEALD with post-deposition plasma. In the former method, O_2 plasma injection time for each BaO and TiO sub-cycle is increased from 10 s to 120 s. In the latter method, additional O_2 plasma exposure was carried out for 1 and 3 hr after deposition.

4.2.2 Material Characterization

Similarly like described in section 3.2.2, the film thickness, roughness and density were measured by XRR measurements (X'Pert Pro, PANalytical). The film thickness was also confirmed by a spectroscopic ellipsometer (Woollam M2000).

The physical thickness of the BTO films are too thin to carry out GIXRD to confirm crystallinity. Hence, HRTEM of cross-sectional TEM samples were obtained at an acceleration voltage of 300 kV to analyze the crystallization of the samples (FEI Titan ETEM 300 kV). TEM sample preparation is described in section 1.2.2.

The composition analysis was conducted by XPS (PHI VersaProbe Scanning XPS Microscope) with Al $(K\alpha)$ radiation (1486 eV). AFM (JEOL 5200) was used to characterize the surface morphology of the films.

4.3

Results and Discussion

Figure 4.23 shows cross-sectional TEM images of the PEALD BTO samples with different in-cycle plasma treatment times as well as different post-treatment plasma exposure (PE) treatments. Prolonged plasma exposure results in larger crystallized areas inside the BTO films. For the BTO film with an in-cycle plasma exposure time of 10 s (Figure 4.23(a)), there are barely areas showing lattice fringes, indicated by white dashed circles (~1 nm sized grains). The BTO film with an in-cycle plasma exposure time of 120 s (Figure 4.23(d)), however, shows more crystalline grains of 2–5 nm in diameter across the whole film from the surface down to the BTO/SiO_2 interface. Zoomed-in HRTEM images of the long exposure sample in Figures 4.23(e) and (f) confirm that the crystalline

area has a lattice spacing (0.20 nm) matching the (100) orientation of the cubic BTO ($a = 0.40$ nm). The sample with the short in-cycle plasma exposure (10 s) was further O$_2$ PE post-treated after deposition. Figures 4.23(b) and (c) show the TEM images after the post-deposition PE treatments for 1 and 3 hr, respectively. Significant differences in crystallization behavior were found between the 1 and 3 hr plasma treatment; after a 1 hr exposure, crystalline grains of 1.5 to 3 nm were found preferentially on the top half of the film (near the surface). In contrast, after a 3 hr exposure, slightly larger crystalline grains of 2 to 4 nm were formed over the whole film uniformly. This shows that prolonged plasma exposures form more nuclei within the whole film and grow them into larger crystalline grains similar to thermal annealing processes.
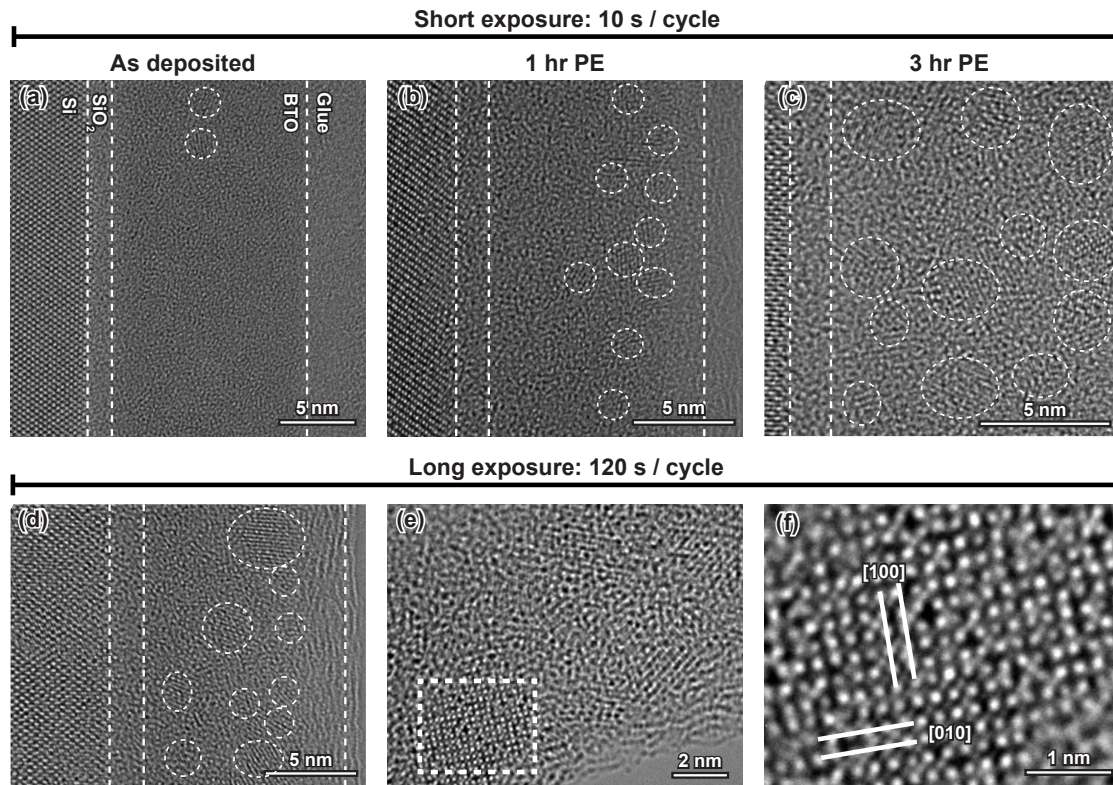
Figure 4.23.

Cross-sectional TEM micrographs are shown for PEALD BTO (40 SC) with a short in-cycle plasma exposure (10 s per cycle) as-deposited, 1 hr and 3 hr PE post-treated in (a), (b) and (c), respectively. (d) Cross-sectional TEM for PEALD BTO (40 SC) with a long in-cycle PE (120 s per cycle) is shown with a zoomed in HRTEM micrograph displayed in (e) and (f). Lattice spacings agree with cubic BTO (100) type planes.

Taking cross-sectional TEM images from Figure 4.23 and segmenting them into areas that show crystalline fringes and areas that do not (i.e. amorphous) gives a first order (assuming the TEM sample is 10 nm or less in thickness) semi-quantitative evaluation

of the crystalline fraction inside the film and where crystallization preferentially occurs. For this purpose the segmented image is sliced up into 1 nm thick slices parallel to the SiO_2/BTO interface and the crystalline fraction (crystalline area/amorphous area) is calculated for each slice. Figure 4.24 shows the resulting crystalline fractions as a function of distance from the SiO_2/BTO interface. The as-deposited (10 s) PEALD BTO sample is compared to the PE post-treatments (1 hr and 3 hr) and the extended in-cycle plasma (120 s) sample in Figure 4.24(a) and (b), respectively.

The as-deposited PEALD BTO film already has a very low fraction of crystallites in the amorphous phase. In the 1 hr post-treatment case the crystallization seems to occur mainly close to the surface of the BTO film. The decrease in crystalline fraction at the topmost surface is due to the amorphization during TEM sample preparation. For the sample with 3 hr post-treatment the crystalline fraction increased throughout the layer indicating that the extended time gives rise to more diffusion of high energy radicals/ions deeper into the film. In the case of an extended in-cycle plasma the crystallizations also seems to occur throughout the whole layer comparable to the 3 hr PE post-treated sample.
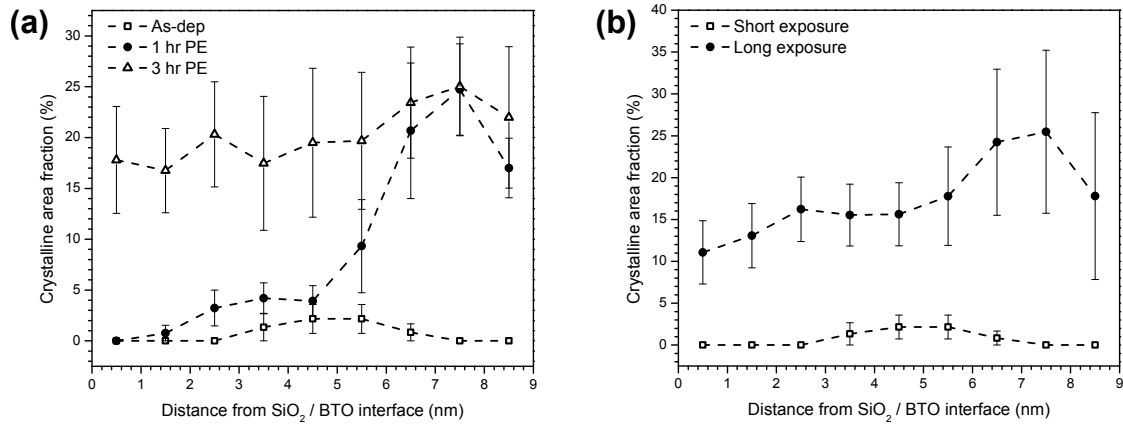
Figure 4.24.

Crystalline area fractions are plotted as a function of distance from the SiO_2/BTO interface comparing different PE post-treatments as seen in (a). The difference between short and long in-cycle plasma exposure time is shown in (b).

To get further insight into the properties of the PEALD BTO thin films AFM, XPS and XRR were conducted. Figure 4.25 shows AFM images taken of as-deposited PEALD BTO as well as 1 hr and 3 hr PE post-treated samples. The resulting root mean square (RMS) roughness values were measured to be between 0.34 and 0.41 nm for all samples. This trend was also confirmed by XRR measurements (cf. Figure 4.28 in section 4.5). Additionally, XRR yields density values for all three samples that are almost identical (~ 4.9 g/cm^3). The oxygen content inside the film as a function of sputtering depth obtained by XPS is displayed in Figure 4.26 comparing as-deposited and 3 hr PE post-treated case. A decrease in oxygen content is observed with increasing sputtering time and the overall content for the 3 hr PE post-treated samples is higher. The full XPS

profile of the PEALD BTO film showing the absence of Carbon in the film is shown in section 4.5 in Figure 4.27.

The density of PEALD BTO (4.9 g/cm^3) is around 50 % higher than that of previously reported thermal ALD BTO (3.3 g/cm^3).[18] Unlike for the case of a PE post-treatment of thermal ALD BTO film, here the PE post-treatment almost did not affect the density of PEALD BTO. The as-deposited PEALD BTO film's high density may indicate that it has already reached its maximum density by the plasma exposure during deposition and hence even in the as-deposited case the film is a mixture of amorphous and nanocrystallites. Also, PE post-treatment did not affect the roughness of the surface of PEALD BTO (while overall its RMS roughness is lower compared to thermal ALD BTO) whereas in the case of thermal ALD BTO it did improve the RMS surface roughness from 0.63 to 0.45 nm.[18] The XPS data indicates that the oxygen PE post-treatment indeed increased the oxygen content in the film and might have reduced the vacancy and trap density in the film. This would reduce leakage currents through the film based on the trap-assisted tunneling mechanism.
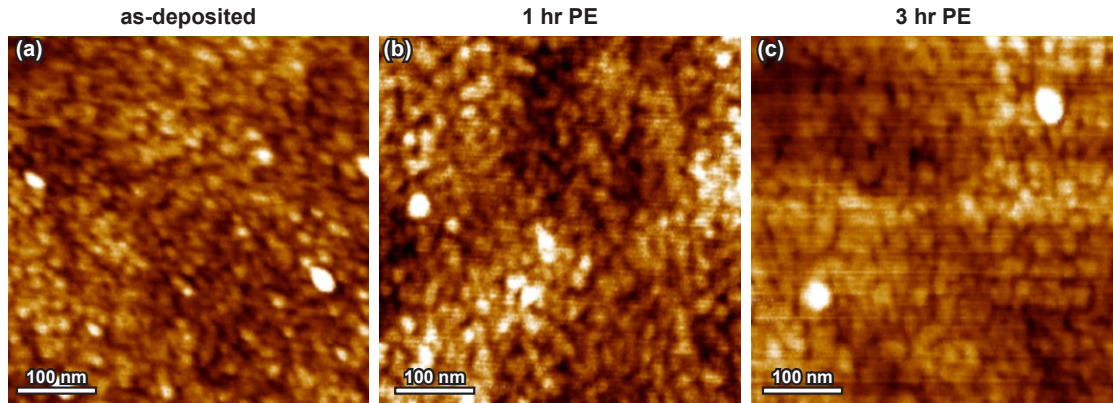
Figure 4.25.

AFM images of PEALD BTO as-deposited, 1 hr and 3 hr PE post-treated are shown in (a), (b) and (c), respectively.
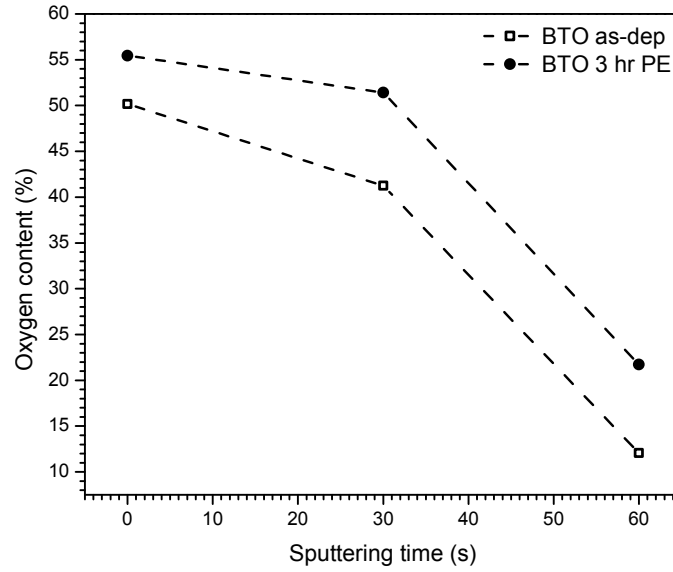
Figure 4.26.

Oxygen content (obtained by XPS) is plotted as a function of sputtering time comparing as-deposited and 3 hr PE post-treated PEALD BTO.

4.4

Conclusion

In summary, it was shown that extended in-cycle plasma as well as a PE post-treatment can enhance the crystalline fraction inside a PEALD BTO film. This in turn is likely increasing the dielectric constant of the deposited film. Unlike for post-treatments of thermal ALD of BTO, the film did not show a significant increase in density or decrease in surface roughness. Further, the oxygen content in the film is increased by a PE post-treatment that may decrease the trap density in the film and hence would reduce leakage currents through the dielectric. As these plasma treatments require only a very low thermal budget (< 300 °C) this finding is very promising for integrated circuit manufacturing.

4.5

Additional Information

Figure 4.28 shows XRR plots of PEALD BTO as-deposited, 1 hr and 3 hr PE post-treated. The fit of the experimental data yields the following density, thickness and roughness values: 4.95 g/cm^3, 12.2 nm and 0.77 nm for as-deposited, 4.99 g/cm^3, 12.1 nm and 0.75 nm for 1 hr PE post-treated and 4.92 g/cm^3, 12.0 nm and 0.83 nm for 3 hr PE post-treated.
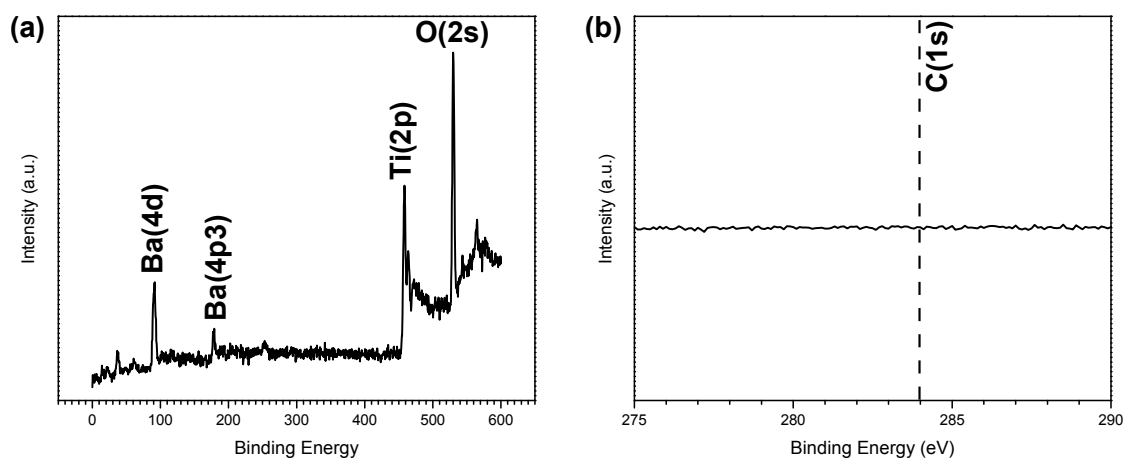
Figure 4.27.
(a) XPS plot of PEALD BTO showing corresponding Ba and Ti peaks. (b) High resolution XPS shows no Carbon peak.
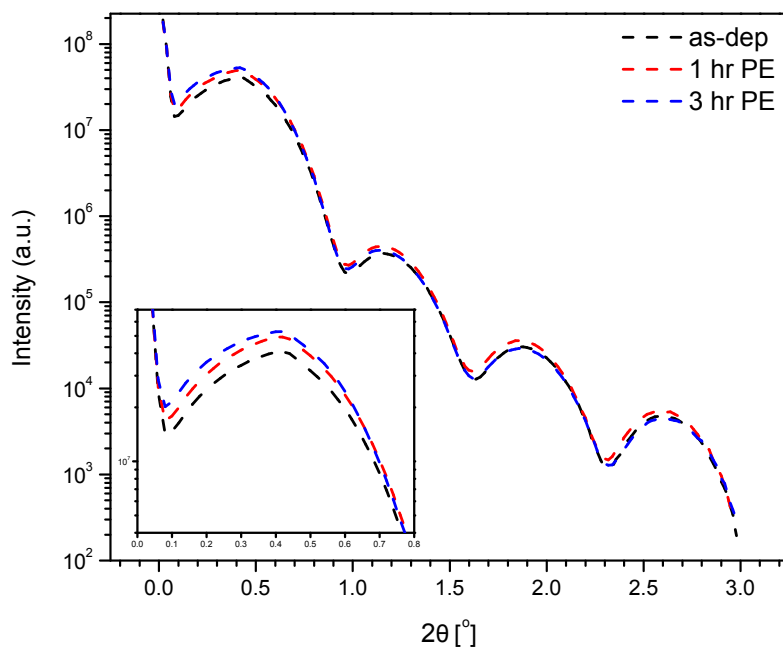
Figure 4.28.
XRR plot of PEALD BTO as-deposited, 1 hr and 3 hr PE post-treated. Inset displays zoomed in view to show the first intensity fall-off that is used to evaluate the film density. No big differences are observed.

> **5**
> # Work Function (WF) Tuning of Al-doped TiN Electrode

Now that high–k BTO was shown to be a feasible candidate to be used as a dielectric film for DRAM by facilitating PEALD and by further enhancing the crystallization of the film by plasma, we can look into electrode materials in more detail and how we can improve the electronic properties of a metal–insulator–metal (MIM) structure. In specific, how to tackle the issue with leakage currents through a thin dielectric film.

There are three main physical parameters that determine tunneling through a dielectric layer for direct tunneling and Fowlder-Nordheim (FN) tunneling: The thickness of the layer, its effective electron mass and the barrier height.

Whereas the first two properties are determined by the dielectric that is used, the barrier height can be maximized via two independent properties: a) The electron affinity of the dielectric layer and b) The work function (WF) of the bottom electrode. The big advantage of tuning b) is the fact that it qualitatively improves the leakage behavior for any dielectric used. Therefore, tuning the WF (i.e. tuning the position of the Fermi level with respect to the vacuum level) can reduce leakage currents independent of the dielectric that is employed. It should be noted that a higher WF value corresponds to a lower position of the Fermi level with regard to the vacuum level. Figure 4.29 illustrates how increasing the WF (lowering the Fermi level position) increases the barrier height to the dielectric (in this case: ZrO_2 on TiN).
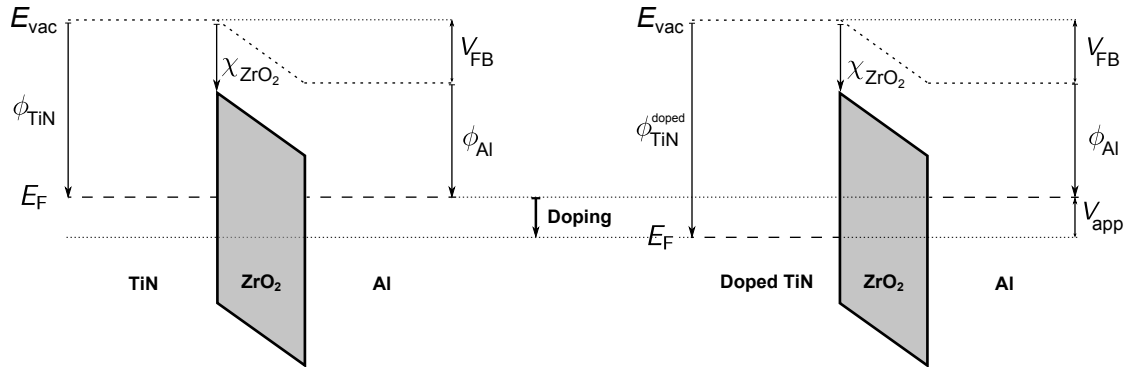
Figure 4.29.
Schematic band diagram is depicted to illustrate the effect of a change in WF on the barrier height for electron tunneling.

5.1

Introduction

Titanium nitride (TiN) is a commonly used electrode material in next generation DRAMs and is also a common commercial material for CMOS and memory fabrication. This is because TiN can provide highly conductive films which can be etched without detrimental etch residues. Further, TiN by ALD can provide conformal films with excellent thickness control and low roughness. The conductivity of TiN is highly dependent on the amount of incorporated oxygen present in the layer with more oxygen lowering the conductivity.[109]

In literature there is a wide variety of reports on the WF of TiN. DC reactive sputtering deposition of TiN yields a work function between 4.2 eV and 4.5 eV.[110] It has been shown that in reactive sputtering of TiN its WF can be tuned between 4.14 eV and 4.82 eV depending on the reactive gas mixture ratio of N_2 and Ar.[111] For TiN deposited by CVD a work function of 5.27 eV and for physical vapor deposition (PVD) a WF of 4.83 eV was reported.[112]

In this section, the effect of Zr-doping on the WF of PEALD TiN is reported. To verify the effect of the increase in WF on the decrease in leakage currents, PEALD ZrO_2 is used as a dielectric for an MIM test structure. The measured reduction of the leakage current agrees well with the trend of reduced FN-tunneling currents with increased electrode WF, corroborated by the FN-tunneling simulations. TEM and SAD reveal the crystalline structure of both PEALD TiN and ZrO_2.

5.2

Experimental Methods

5.2.1 Material Fabrication

TiN and ZrO_2 were deposited by PEALD in a Fiji ALD reactor (Cambridge Nanotech/Ultratech) that is equipped with a remote ICP generator. The base pressure of this ALD reactor is 200 mTorr while there is a constant flow of Ar at 60 sccm in the precursor manifold line. Tetrakis(dimethylamido)titanium (TDMA–Ti) and N_2 plasma were used as precursors for the deposition of TiN. For the deposition of ZrO_2 TDMA–Zr and O_2 were used as precursors. The titanium and zirconium precursor were maintained at 75 °C and were pulsed for 0.3 s per cycle followed by a 60 s long exposure (i.e. valve separating chamber and pump closed). After the first precursor exposure the chamber is purged for 60 s to remove the remaining (unreacted) precursor and the by-product resulting from the reacted ligands. As co-reactant a nitrogen (for TiN) and a oxygen (for ZrO_2) plasma were used generated by a remote ICP generator at a power of 300 W. A constant flow of Ar with 200 sccm is provided through the plasma line while during the plasma step (20 s) there is an additional N_2 or O_2 flow of 50 sccm. After the plasma exposure the chamber is purged for another 10 s. Substrate temperatures were 150 °C and 250 °C for ZrO_2 and TiN, respectively.

5.2.2 Material Characterization

Cross-sectional TEM samples were prepared as described in section 1.2.2. HRTEM and SAD patterns were used to characterize the structure of the TiN and ZrO_2 films by an FEI Tecnai G2 F20 X–TWIN FEG (200 kV) and an FEI Titan ETEM (300 kV).

WFs were measured by UPS with a model AC–2 photo-electron spectrometer at atmospheric pressure, using a deuterium UV source in air. Fowler's hypothesis for metals was used in determining the WF of the TiN thin films. Straight lines were fitted to plots of quantum yield to the half power versus photon energy then extrapolated to the x–axis to give the photo threshold.[57]

For the electrical measurement, $TiN/ZrO_2/Pt$ metal–insulator–metal capacitors were fabricated on top of ~150 nm thick thermally grown SiO_2 on Si wafers as a substrate and a DC-sputtered Pt (200 nm) film as the top electrode. The current density–voltage (J–V) curves (0 to +2 V) were measured by a Keithley SourceMeter (2636A).

5.3

Results and Discussion

The investigated electrode material was chosen to be TiN deposited by PEALD. Figure 4.30(a) shows a cross-sectional view of PEALD TiN on thermally grown SiO_2 indicating that the deposited structure is very smooth and uniform and has a thickness of about 31 nm. Furthermore, in Figure 4.30(b) and (c) a HRTEM micrograph and a SAD pattern are shown to confirm the crystalline structure of the TiN film. Both, lattice spacing determined in HRTEM and diffraction ring spacing in the SAD pattern is in good agreement with the cubic Fm3m structure of TiN. The WF of as-deposited un-doped PEALD TiN was 4.85 eV, measured by UPS. The film's sheet resistance was 20 $\mu\Omega\cdot$cm.
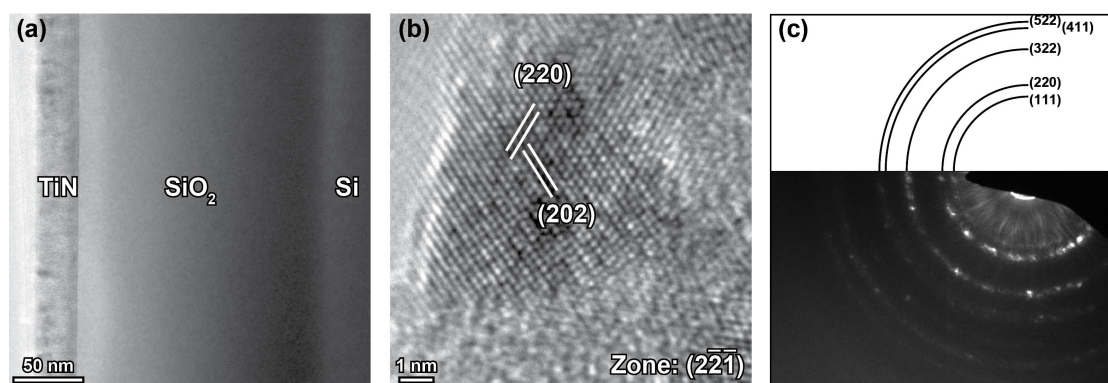
Figure 4.30.
TEM micrographs showing 31 nm thick PEALD TiN in cross-section. (a) Low magnification of TiN layer on thick thermally grown SiO_2. (b) HRTEM revealing the cubic Fm3m structure confirmed by SAD pattern depicted in (c).

To investiagte the effect of Zr-doping on the WF of TiN, 4 different cycle ratios between Ti and Zr were chosen, respectively: 10 : 1, 5 : 1, 1 : 1 and 1 : 2. The measured WFs of these films (including the un-doped case) are plotted in Figure 4.31. It should be noted that the Zr content was calculated by using the cycle ratios but will need to be determined by XPS in future work. Interestingly, the WF peaks at a Ti–to–Zr cycle ratio of 5 : 1 (5.07 eV) and falls off with increasing Zr content in the film. The resistivities of the samples with a Ti–to–Zr cycle ratio of 10 : 1, 5 : 1, 1 : 1 and 1 : 2 were measured as 100 $\mu\Omega$·cm, 100 $\mu\Omega$·cm, 100 $\mu\Omega$·cm and 75 $\mu\Omega$·cm, respectively.
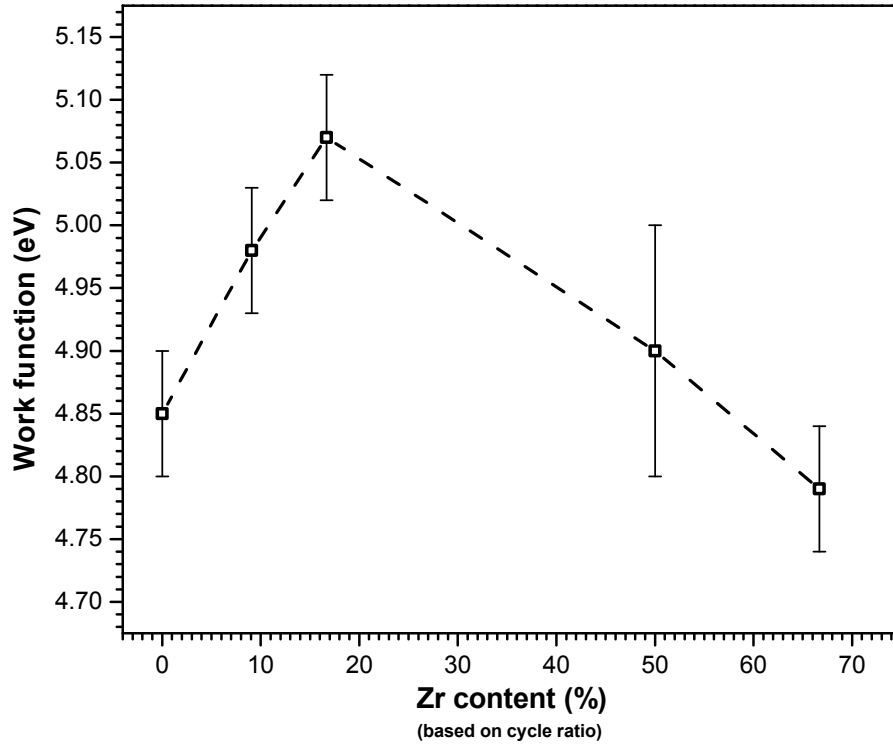
Figure 4.31.

Measured WF (by UPS) as a function of Zr doping content is shown. Zr content is calculated from the ratios between number of Zr and Ti PEALD cycles.

In the next step, to test the reduction of leakage currents through a dielectric by increasing the WF of the bottom electrode, a TiN — PEALD ZrO_2 — Pt MIM structure was fabricated. Cross-sectional TEM of PEALD ZrO_2 layer on Si wafers with sputtered Pt top electrode is displayed in Figure 4.32(a). The deposited ZrO_2 layer has a thickness between 4–5 nm. The inverse filtered Fourier transform (IFFT) in Figure 4.32(b) reveals atomic plane spacings that are consistent with the monoclinic phase of ZrO_2 with plane orientations of (111) type.
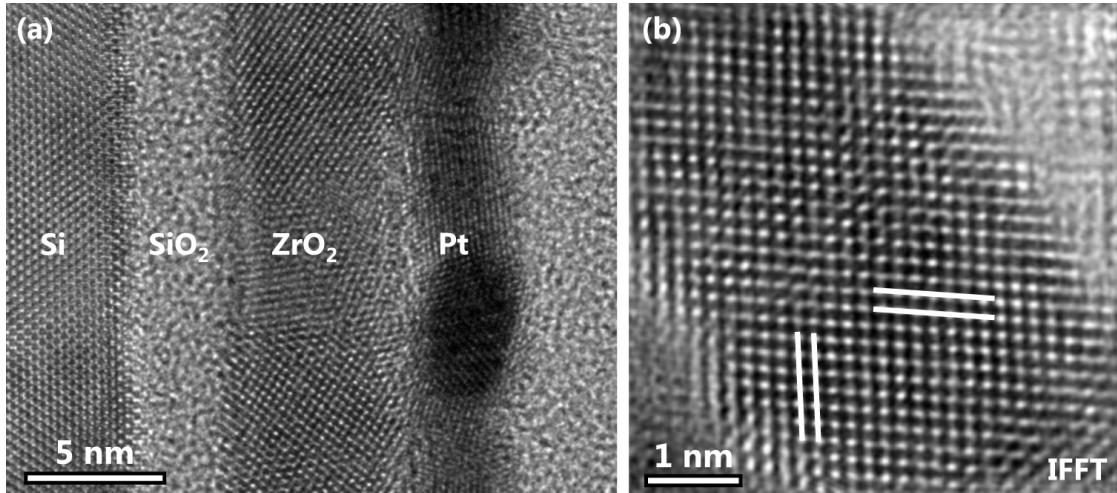
Figure 4.32.
(a) Cross-sectional TEM of PEALD ZrO_2 on a Si wafer with sputtered Pt top electrode is shown. (b) IFFT shows atomic resolution of monoclinic ZrO_2 with measured spacings in agreement with (111) type planes.

To investigate to what extend the WF of the metal TiN bottom electrode can affect the leakage current behavior in an MIM structure, an FN-tunneling simulation was performed. For the electron effective mass m_{eff} of TiN, $1.1 \cdot m_0$ was used.[113] The following MIM structure was calculated: TiN of varying WF as bottom electrode; a 4 nm thick ZrO_2 layer as dielectric (electron affinity $= 2.99$ eV and $m_{eff} = 0.5 \cdot m_0$)[114, 115] and Pt (WF $= 5.5$ eV) as top electrode. The resulting FN-tunneling current densities at a fixed bias (1.6 V) are plotted as a function of the TiN WF in Figure 4.33(b) showing decreasing leakage currents with an increasing WF. Experimental confirmation of this trend was obtained by comparing the measured leakage current densities for a 4–5 nm thick ZrO_2 layer on top of un-doped TiN to the one measured on top of Zr-doped TiN (Ti:Zr cycle ratio = 5:1). The measured current densities are plotted as a function of applied voltage in Figure 4.33(a).

The calculated trend was also observed experimentally and showed that the doping of TiN by Zr not only increased the WF of the bottom electrode but also resulted in a reduction in leakage currents through the ZrO_2 film. For comparison, the leakage currents at 1.6 V for the doped and un-doped cases (as taken from data in Figure 4.32(a)) are added to the plot in Figure 4.32(b) to show the qualitative agreement with the calculated trend.
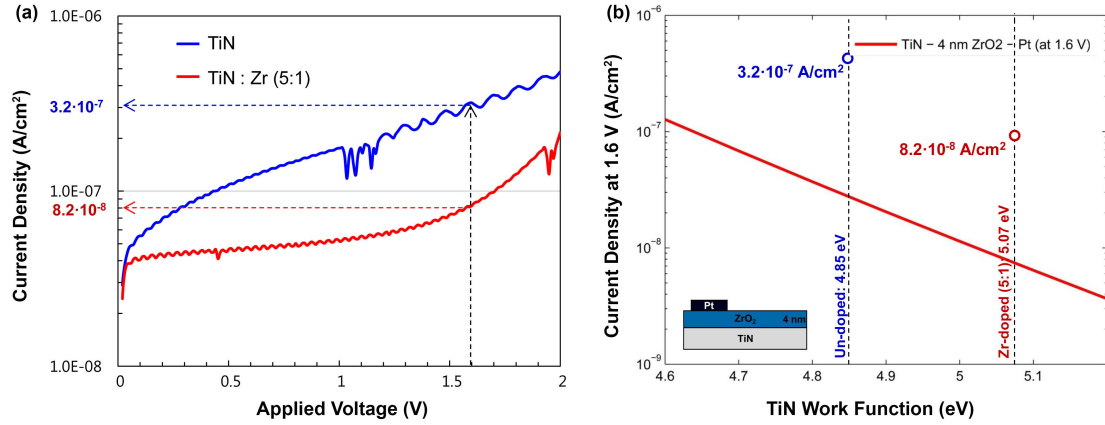
Figure 4.33.

(a) Measured leakage current density is plotted as a function of applied voltage for a 4 nm thick PEALD ZrO_2 layer on top of TiN (blue curve) and on top of 5:1 Zr-doped TiN (red curve). (b) Leakage currents (at 1.6 V) are calculated as a function of changing WF of the bottom electrode for a TiN — 4 nm ZrO_2 — Pt stack.

5.4

Conclusion

We have shown that Zr-doping added during PEALD of TiN makes tuning of the WF possible and shows the maximum WF value at a Ti–to–Zr cycle ratio of 5 : 1. While XPS data is still necessary to verify the actual Zr content in the TiN film, we confirmed that the increase in WF resulted in a reduction in leakage currents through a dielectric film (ZrO_2) as expected from our FN-tunneling simulations. We believe that WF tuning of TiN has implications on virtually all dielectrics that may be used for MIM components for DRAMs.

<div style="border:1px solid">

6

PEALD of Al-doped BaTiO$_3$

</div>

In the previous sections we have established titanium based dielectrics are able to cover high ARs and we have developed high–k dielectric BTO by PEALD. Also, we showed that Zr-doping increases the WF of a TiN metal electrode to reduce leakage currents through dielectric films. While crystallized BTO (by plasma post-treatment) shows a very low EOT and high dielectric constant, the leakage currents still tend to be an issue. In this last section, Al-doping into the BTO film will be explored to reduce the leakage currents while keeping most of its high dielectric constant.

6.1

Introduction

BTO films with higher Ti content than Ba showed larger dielectric constants presumably due to higher crystallinity inside of the thin film achieved under certain plasma exposure and power (cf. section 4). The Ti-rich BTO film, however suffers from higher leakage currents due to existence of grain boundaries formed during the crystallization process. Previously, Sn_2O_3 doping of BTO (> 0.4 wt%) showed an anomalous increase in electrical resistivity, making BTO a highly insulating dielectric.[116] Furthermore, Al_2O_3 (same oxidation number as Sn_2O_3) proved its effectiveness to reduce leakage currents when it was used as a dopant in TiO_2,[72] ZrO_2 and HfO_2.[117]

In this study, we demonstrate PEALD of Al-doped BTO and report the effect of Al-doping of Ti-rich BTO films with regard to crystallization and modulation of its electronic structure. We show that Al-doping of BTO considerably reduces leakage currents with a minimal sacrifice of dielectric constant compared to un-doped BTO.

6.2

Experimental Methods

6.2.1 Material Fabrication

The detailed description of PEALD conditions for BTO fabrication in a commercial PEALD station (Oxford Instruments, FlexAL) were reported in section 3.2.1. The atomic percentage of Al in the BTO films was controlled by varying the Al_2O_3 and BTO deposition cycle ratio ([number of Al cycles]/[number of Al cycles + number of BTO cycles]). Ba–to–Ti pulse ratio was 1:5 in one super-cycle. The BTO films were deposited by 15 super-cycles resulting in a physical thickness of about 5 nm. At this deposition condition, Ti-rich BTO films ([Ti]/([Ba]+[Ti])= $60 \sim 67$ at%) were deposited. For Al-doped BTO films, additional Al_2O_3 PEALD cycles composed of TMA pulsing/purging

and the followed O$_2$ plasma pulsing/purging were carried out within the BTO PEALD cycles. Samples labeled as x TMA BTO (where $x = 0, 3, 5$ and 8) had x number of Al cycles incorporated evenly into the 15 BTO super-cycles.

To enhance the crystallinity of Al-doped BTO films and reduce lattice damage/defects,[18] an O$_2$ plasma-treatment for 3 hr (plasma power = 400 W, plasma pressure = 5 mTorr) was applied after the deposition of the BTO films in an O$_2$ atmosphere (Praxair, purity grade 4.8). The post O$_2$ plasma treatment is advantageous over rapid thermal annealing (RTA) because the process temperature can be lowered below 500 °C. Although this post-processing time appears to be long from a industrial manufacturing standpoint, it might be mitigated by higher plasma powers. As bottom electrodes, 20 nm Zr-doped TiN (Zr:TiN) on thermally-grown SiO$_2$ (200 nm) on p–Si prepared by another commercial PEALD station (Fiji, Cambridge Nanotech/Ultratech) with a cycle ratio of TiN : Zr = 5:1 was adopted. The zirconium doping into TiN is beneficial in terms of higher resistance against oxygen diffusion.[118] Also, as explained in section 5, Zr-doped TiN shows the highest WF at a doping ratio of Ti–to–Zr of 5:1, that being beneficial for reducing leakage currents. After the fabrication of Zr:TiN/Al-doped BTO samples, rectangular-shaped Pt top electrodes (area: 0.75 mm × 0.75 mm; thickness: 200 nm) were patterned by DC sputtering for electrical measurements.

6.2.2 Material Characterization

Cross-sectional TEM samples were prepared as described in section 1.2.2. Since the physical thickness of 5 nm is too thin to carry out GIXRD to confirm crystallinity, HRTEM was used to characterize the thickness and crystallization of the deposited Al-doped BTO films by an FEI Titan ETEM (300 kV).

An atomic force microscope (AFM, JEOL 5200) was used to characterize roughness. The composition analyses were conducted by X-ray photo-electron spectroscopy (XPS, PHI VersaProbe Scanning XPS Microscope) with Al (Kα) radiation (1486 eV). Angle-resolved XPS (ARXPS) measurements were carried out to obtain high resolution compositional depth profiles and the samples were rotated to 75° from its original surface plane to achieve a grazing angle.

The valence band offsets ($E_\text{vac} - E_\text{v}$), determined by the difference between the vacuum-level energy and the valence band maximum were measured by UPS with a model AC–2 photo-electron spectrometer at atmospheric pressure, using a deuterium UV source in air. Fowler's hypothesis for semi-conductors was used in determining the valence band offsets of thin films. Straight lines were fitted to plots of quantum yield to the half power versus photon energy then extrapolated to the x–axis to give the photo threshold.[57]

Optical band gap measurements were performed by an UV–vis spectrometer (Perkin-Elmer Lambda 1050). The capacitance–frequency (C–f) and current–voltage (J–V) characteristics were measured using a LCR meter (Agilent, model no. E4980A) and a Keithley 2636A Source-meter, respectively. The leakage currents were measured between -1.8 and $+1.8$ V bias and the dielectric constants were measured at a frequency of 1 kHz.

6.3

Results and Discussion

Figure 4.34(a) shows ARXPS depth profile analysis for un-doped BTO (15 super-cycles for BTO, Ba–to–Ti pulse ratio = 1 : 5). Atomic signals stemming from BTO appear from 0 to 0.6 min sputtering with Ar^+ ions confirming a Ti-rich cation composition of $[Ti]/([Ba]+[Ti]) = 60 \sim 66$ at%. Note that atomic signals with no sputtering (0 min) were affected by carbon at the surface. For Al-doped BTO films, the overall $[Al]/([Al]+[Ba]+[Ti])$ atomic ratios of the BTO samples with x TMA cycles ($x = 0$, 3, 5 and 8) were measured to be 8, 12 and 22 at%, respectively. Hence, the Al content is linearly increased with the number of TMA cycle (Figure 4.34(b)). After a 3 hr O_2 post plasma treatment all Al-doped BTO films showed higher oxygen concentration, especially near the surface, reaching $\sim$60 at% throughout the film.
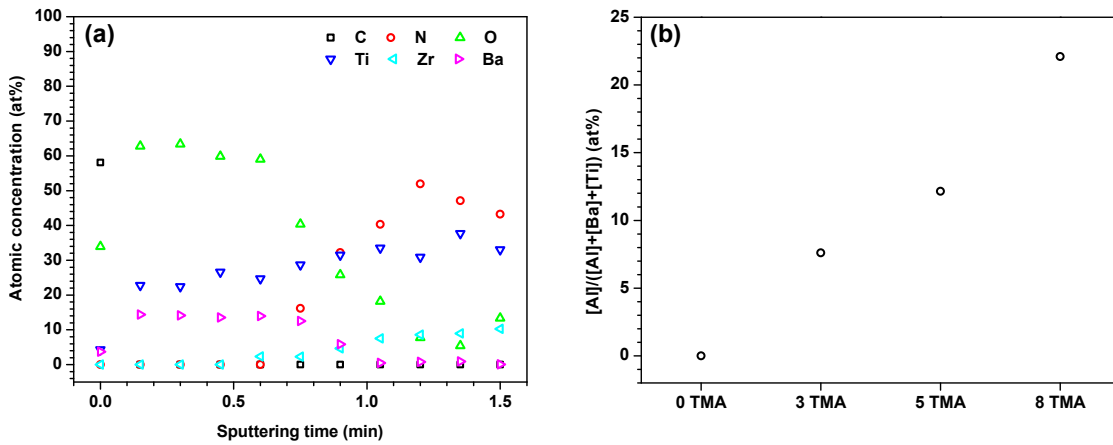
Figure 4.34.

(a) XPS depth profile of un-doped BTO film measured by ARXPS and (b) $[Al]/([Al]+[Ba]+[Ti])$ atomic concentration ratios of the different Al-doped BTO films measured by XPS.

The effect of Al-doping on crystallization of BTO by a post-plasma treatment is presented by cross-sectional HRTEM images in Figure 4.35. The HRTEM micrograph of the as-deposited BTO film without Al-doping (cf. Figure 4.35(a)) shows only very few small crystallites whereas the same sample post-treated by an O_2 plasma (cf. Figure 4.35(b)) resulted in a large number of crystallites in the film. The inset in Figure 4.35(b) shows lattice spacings of 0.20 nm in agreement with (100) directions of cubic (a 0.394–0.403 nm), tetragonal (a 0.394–0.399 nm, c 0.399–0.404 nm), or rhombohedral (a 0.400 nm, θ 89.5°) BTO.[102] The HRTEM micrographs of 3, 5 and 8 TMA samples with a 3 hr post-plasma treatment are shown in Figure 4.35(c)–(e), respectively.
TEM reveals that the un-doped (Ti-rich) BTO film can be crystallized by an O_2 plasma post-treatment (just like shown in section 4), whereas with increasing number of TMA doping cycles within the BTO film the effect of crystallization appears to be reduced.
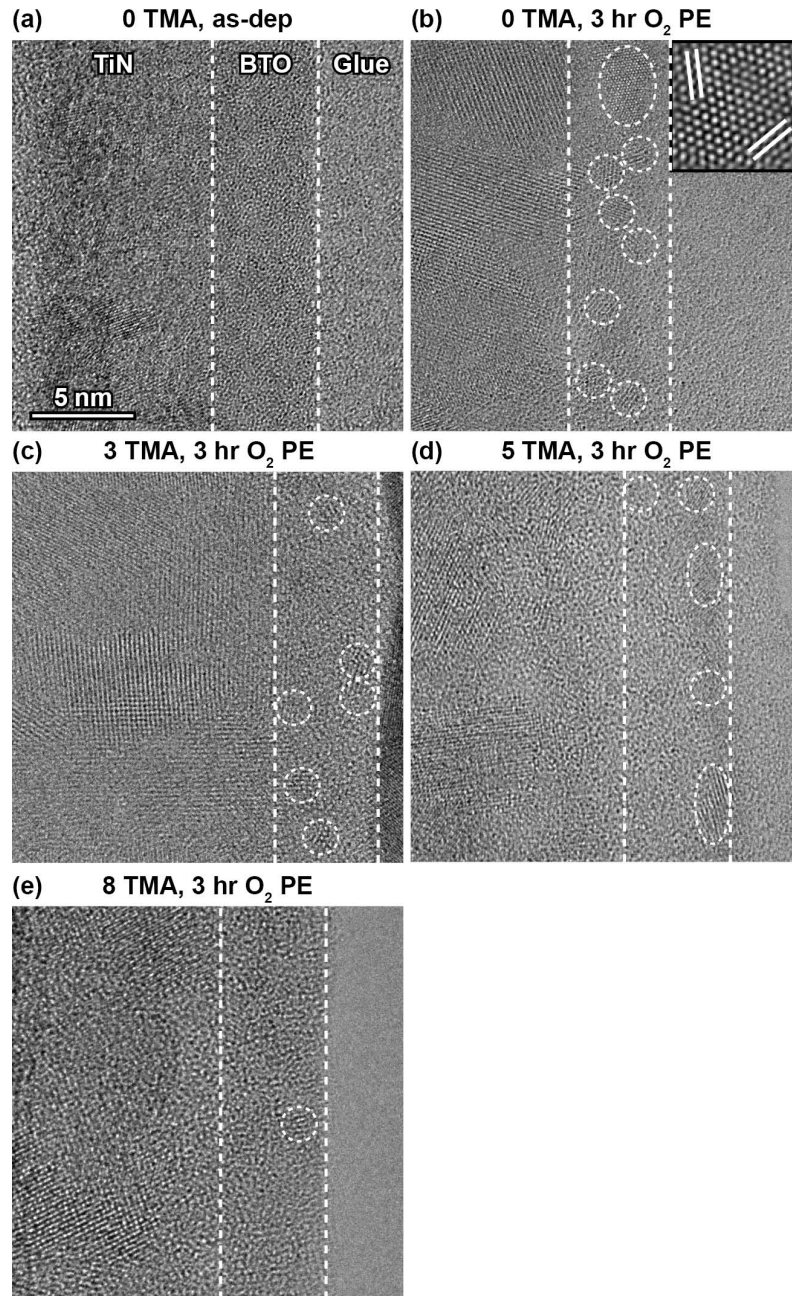
Figure 4.35.

HRTEM of un-doped and Al-doped BTO films (x cycles of TMA in 15 super-cycles of BTO) with and without a 3 hr O$_2$ plasma treatment: (a) as-deposited BTO with 0 TMA (inset show IFFT with atomic resolution revealing atomic spacings of 0.20 nm), (b)–(e) 3 hr O$_2$ plasma post-treated BTO with 0, 3, 5 and 8 TMA, respectively. Dashed lines are added to emphasize interfaces and crystallites.

The variations in the dielectric constants ϵ of the un-doped and Al-doped BTO films with various Al doping ratios are shown in the Figure 4.36(a). The ϵ values of as-deposited BTO films were $\sim$11 regardless of the Al content. After being post-treated with an O_2 plasma, the dielectric constants were significantly increased to as high as 44. After the 3 hr O_2 plasma post-treatment, the BTO samples with 0 TMA and 3 TMA Al-doping show almost the same dielectric constant. Whereas, for BTO films with an even higher Al content (5 and 8 TMA) lower permittivity values were observed with an increasing number of TMA cycles. The leakage current densities as a function of applied bias of un-doped and Al-doped BTO are shown in Figure 4.36(b) (J–V plots). Current densities under positive bias (w.r.t. the top Pt electrode) correspond to electrons being injected from the bottom metal Zr:TiN electrode (WF = 5.0 eV) into the dielectric film. In the case of the as-deposited samples, un-doped BTO films showed a relatively high J at 1.6 V ($10^{-4} \sim 10^{-2}$ A·cm^{-2}). Interestingly, leakage currents remain constant and start to increase at a bias larger than 0.5 V. For the samples with an O_2 plasma treatment, the behavior of J–V was changed (Figure 4.36(b), closed symbols): leakage currents were significantly decreased ($\lesssim 10^{-6}$ A·cm^{-2} at 1.6 V) and Al-doping further decreased the leakage current below $2 \cdot 10^{-7}$ A·cm^{-2} at 1.6 V.

The dielectric constant of as-deposited BTO with various Al doping concentrations is similar to the previously reported permittivity value (15) of amorphous BTO as well as the permittivity value (7.7) of amorphous Al_2O_3.[14, 119] The large increase of the permittivity after the O_2 plasma post-treatment can be explained by the formation of 1–3 nm sized crystalline BTO grains, confirmed by TEM as seen in Figure 4.35. The trend of lower permittivity values with increasing Al-content is consistent with the previously reported ϵ values of Al-doped TiO_2 as a function of Al contents. The higher Al doping concentration (> 20 at% with respect to total cations) resulted in lower bulk permitivity values due to the lower polarization of Ti–O–Al and the formation of a $\sim$1 nm thick interfacial Al_2O_3 oxide layer.[72] The leakage current behavior of as-deposited, un-doped BTO samples appears to correspond neither to Schottky emission nor to Pool-Frenkel (PF) emission, but is well explained by Fowler-Nordheim (FN) tunneling (i.e. $\ln(J/E^2)$ decreases linearly with increasing $1/E$).
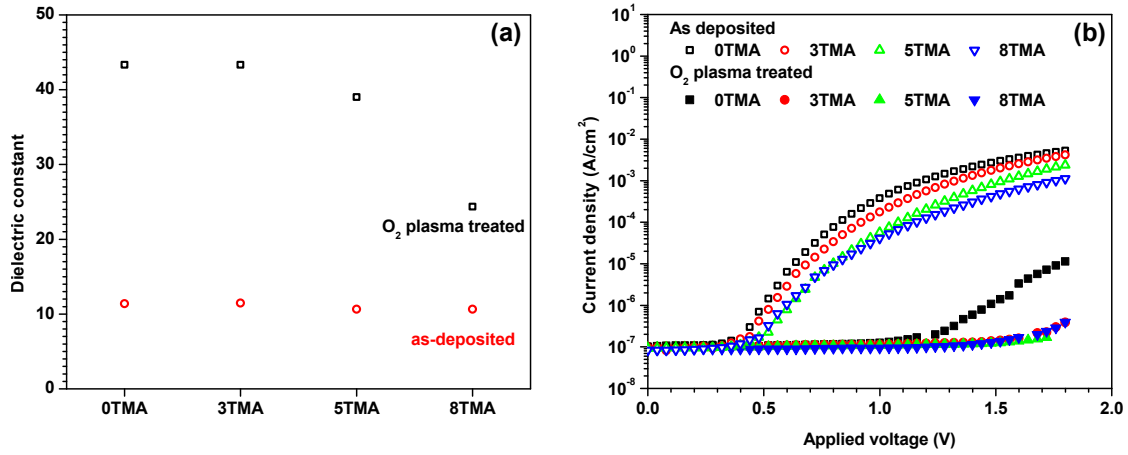
Figure 4.36.

Electrical properties of un-doped and Al-doped BTO (x cycles of TMA in 15 super-cycles of BTO) : (a) dielectric constant at 1 kHz and (b) the applied current density–voltage curves.

To elucidate the reasons for the remarkable improvements in the leakage current properties of Al-doped BTO, leakage current mechanisms of the Zr:TiN/un-doped BTO and Zr:TiN/Al-doped BTO samples were investigated. Since the barrier height is a crucial factor to determine the leakage current mechanism and to understand the underlying reasons for the decrease of leakage currents by Al-doping, measurements of the valence band offset ($E_{\mathrm{vac}} - E_{\mathrm{V}}$) and band gap ($E_{\mathrm{g}}$) were carried out. Higher conduction band offset $E_{\mathrm{vac}} - E_{\mathrm{C}}$ (equivalent to $E_{\mathrm{vac}} - E_{\mathrm{V}} - E_{\mathrm{g}}$) results in a higher barrier height leading to a reduced leakage current.

The $E_{\mathrm{vac}} - E_{\mathrm{V}}$ values (as measured by UPS) for the BTO samples with x TMA cycles ($x = 0, 3, 5, 8$) were 5.43, 5.35, 5.31 and 5.24 eV, respectively. For O$_2$ post-plasma treated samples, the valence band offsets are further decreased to 5.32, 5.27, 5.22 and 5.12 eV (as shown in Figure 4.37(a)) for the Al-doped BTO samples with x TMA cycles ($x = 0, 3, 5, 8$) that had Al atomic ratios of 0, 8, 12 and 22 at%, respectively. Bandgap values as plotted in Figure 4.37(b) are increased by $0.4 \sim 0.5$ eV with 3 cycles of TMA Al-doping. Plasma treatment and additional doping of Al have no clear effect on futher changing the band gap.

The UPS measurements showed that the valence band offset can be decreased by ~ 0.3 eV with Al-doping and O$_2$ plasma treatment. Not only the decrease of the valence band offset increases the barrier height but also the observed increase of the band gap by Al-doping contributes. These two observations offer an explanation for the decrease of the measured leakage currents of Al-doped BTO with a plasma post-treatment.
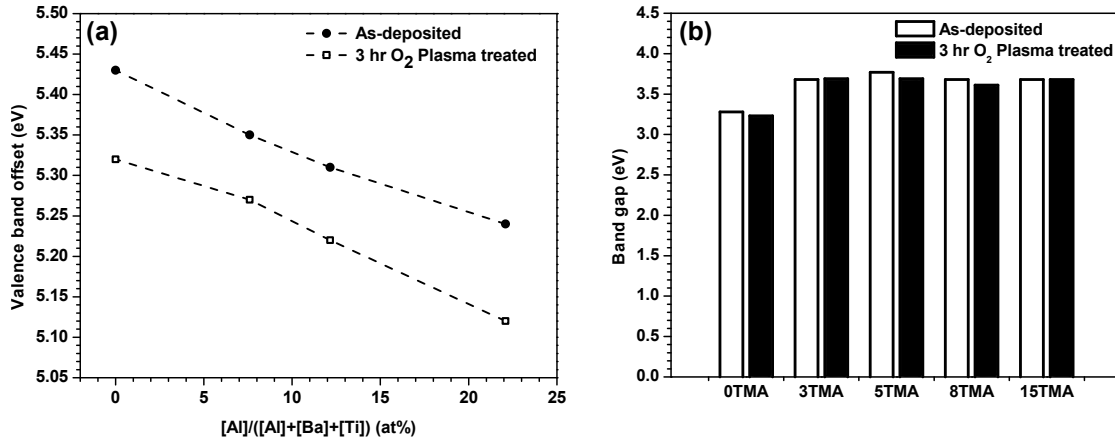
Figure 4.37.

(a) Valence band offset ($E_{\text{vac}} - E_{\text{V}}$, measured by UPS) values depending on aluminum doping concentration in the film (full circles: as-deposited, open rectangles: 3 hr O_2 plasma treated), (b) band gap E_{g} depending on the number of Al cycles.

6.4

Conclusion

In conclusion, it was demonstrated that by Al-doping of PEALD BTO films with an O_2 plasma post-treatment, leakage currents can be significantly reduced compared to the un-doped case while keeping the dielectric constant high. A leakage current of less than $2 \cdot 10^{-7}$ A·cm^{-2} at 1.6 V was achieved as well as a dielectric constant as high as 44 at a physical thickness of 5 nm, giving an EOT of ~5 Å. When the Al-doping concentration is increased more than 3 TMA cycles the effective dielectric constant of the doped and plasma treated BTO film was reduced. The achieved electrical performance for a high–k dielectric film of around 5 nm in thickness and a deposition/processing temperature of 250 °C is to this date the best that has been reported in literature.

Conclusion and Summary

Contents

1 ──
Conclusion and Summary

In summary, the need for high–k dielectrics was motivated by the rapid down-scaling of DRAM devices, and the promising candidate BaTiO$_3$, that is a perovskite structure, was successfully deposited by the key enabling technique PEALD. The physics of dielectrics and the different tunneling mechanisms were discussed and showed pathways of enhancing the dielectric constant by keeping the dead layer capacitance in mind and reducing leakage currents by increasing the effective barrier height for tunneling. ALD and PEALD were reviewed in detail as well as all characterization techniques that were employed to characterize thin high–k dielectric films such as XRD, GIXRD, XPS, XRR, TEM, HRTEM, SAD, spectroscopic ellipsometry and UPS. By means of these deposition and characterization techniques we were able to show the conformal coverage of TiO$_2$ on high AR trench-like substrates by PEALD by increasing the in-cycle plasma exposure time. Additionally, crystallization of TiO$_2$ by extended plasma times during PEALD opened up an avenue for tuning morphological properties. Laying this groundwork for TiO$_2$ we moved on to the more complex ternary structure BaTiO$_3$ and showed that its deposition by PEALD is possible (previously not established). Also in this case we studied the effect of plasma on the crystallization behavior and found that it is possible (although more challenging than in the case of TiO$_2$) to form small crystallites in the amorphous matrix. While this technique provides a pathway for increasing the dielectric constant, the reduction of leakage currents through the BTO film was still an issue. To tackle this issue, we employed two strategies: 1) Doping of the metal TiN electrode to increase the WF (hence increase the effective barrier height) and 2) Doping of BTO by Al to reduce the electron affinity of the dielectric (hence also increasing the effective barrier height). Combining these two strategies with the plasma effect of crystallization achieved a structure with a high dielectric constant (low EOT, high capacitance) and low leakage currents.

To compare our achieved results with the previous electrical performance metrics, both are listed in Table 5.1. This shows that indeed the results are the best in terms of the key metrics achieved to date and additionally this was done at a much lower processing temperature of 250 °C. In addition, Figure 5.1 marks the EOT value from this work in the DRAM down-scaling plot that was depicted in the introduction of this thesis. An EOT of 5 Å is in line with the predicted values for the projected trend time-line necessary for next generation of DRAMs.
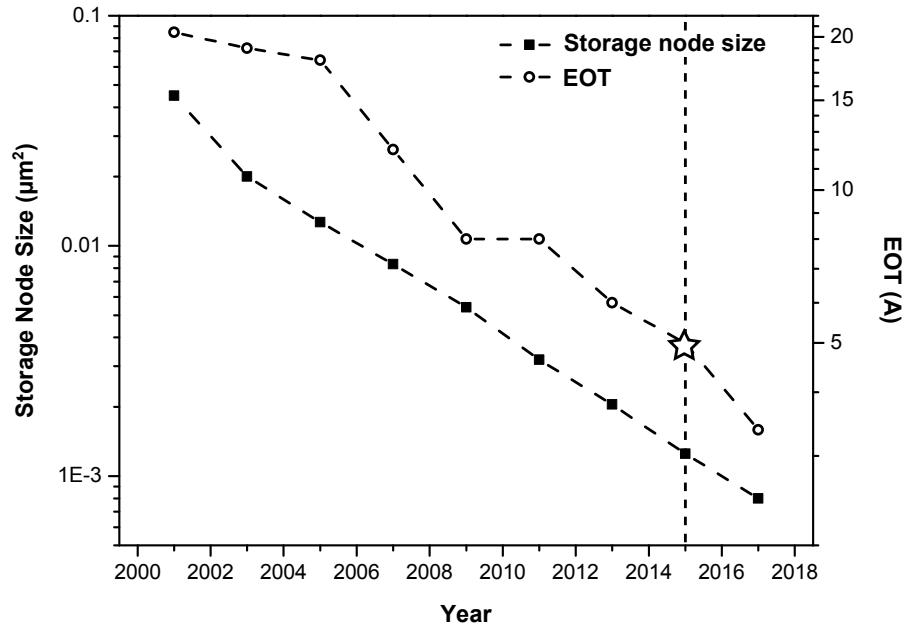
Figure 5.1.

Storage node size and EOT are plotted logarithmically between year 2000 and 2017. Values are projected past 2013.[3–6] EOT value achieved in this work and current year are emphasized.

Ref.	1st Author	Method	Material	Thickness (nm)	k	EOT (Å)	Leakage (A/cm^2) at 1 V	Temp. (°C)
[15]	Vehkamäki	ALD	STO	400	180	87 *	$5.0 \cdot 10^{-4}$	500
			BTO	–	165	–	–	500
[19]	Wang	ALD	STO,BTO	90	400	8.0	–	620
[13]	Tohma	CVD	BTO	520	96	211 *	$1.0 \cdot 10^{-5}$ **	700
[20]	Chen	PLD	BST	150	1370	6.9 *	$1.0 \cdot 10^{-6}$ **	780
[14]	Vehkamäki	ALD	BTO	32	73	18	$1.0 \cdot 10^{-7}$	600
[21]	Lee	ALD	STO	20	108	7.2	$3.0 \cdot 10^{-7}$ **	700
[22]	Lee	ALD	STO	21 *	146	5.7	$6.0 \cdot 10^{-8}$ **	650
[23]	Popovici	ALD	STO	10	181	5.6	$2.0 \cdot 10^{-6}$ **	600
[24]	Liu	PLD	BST	580	700	32 *	$4.4 \cdot 10^{-9}$	500
[25]	Aslam	PEALD	STO	30	78 *	15 **	$1.0 \cdot 10^{-5}$ **	650
[26]	Lee	ALD	STO	14.2	129 *	4.3	$1.0 \cdot 10^{-7}$ **	650
Schindler, Kim		**PEALD**	**Al:BTO**	**5**	**44**	**5**	$\mathbf{< 2.0 \cdot 10^{-7}}$	**250**

Table 5.1.

List of relevant publications on dielectric properties of titanates reported in literature. Last line states key parameters of this thesis' work.

2

Future Work

There are two main research topics that are currently being explored and are not yet fully finalized.

2.1

O$_2$ Reactivity of TDMA-Type Precursors

During experiments with TDMA–Ti precursors for depositing TiO$_2$ by PEALD on high AR substrates, we noticed that there is a non-negligible reaction of this precursor with O$_2$ alone (no plasma turned on). To our knowledge, this phenomenon has not yet been fully explored and may be of interest to the ALD community.

Figure 5.2 shows results on TiO$_2$ deposited using TDMA–Ti and O$_2$ alone as precursors. The effect of O$_2$ duration per cycle, substrate temperature and number of cycles are plotted in (a)–(c), respectively.

These results indicate that the effect seems to level off with increasing O$_2$ durations and is thermally activated (exponential increase of GPC with temperature). The plot in Figure 5.2(c) also suggests that there is substrate inhibited growth where a threshold of 50–100 cycles need to be applied for growth to occur.

Additionally, we carried out XPS, TEM, XRD and XRR to gain further inside into the deposited films. XPS indicates that the films grown by pure oxygen have no carbon or nitrogen contamination indicating that the ligands are stripped of in a clean fashion by oxygen alone. Further evaluation of XRR, TEM and XRD data is required to gain insight into the effect of O$_2$ co-reactant on crystallinity and density.

A peer-reviewed publication on this topic is in preparation: *Molecular Oxygen Reactions with Tetrakisdimethylamido-metal Precursors for Atomic Layer Deposition*, P. Schindler, J Provine, J. Torgersen, K. Kim, H. P. Karnthaler and F. B. Prinz
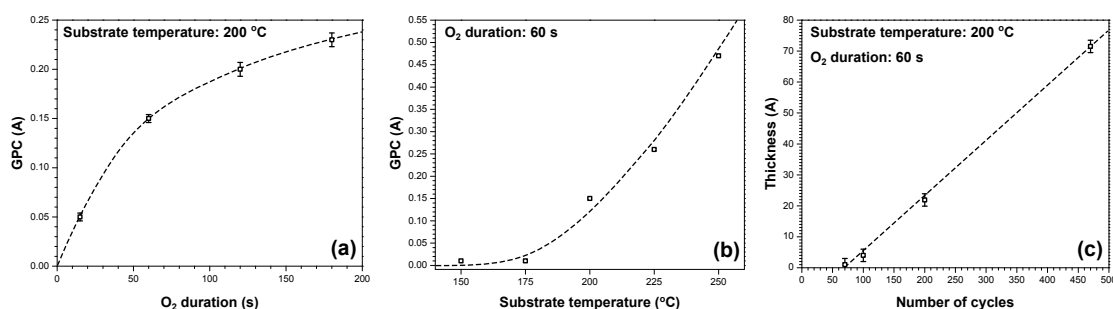
Figure 5.2.

(a) GPC of TiO$_2$ deposited at 200 °C substrate temperature as a function of O$_2$ duration per cycle. (b) GPC of TiO$_2$ deposited at a fixed O$_2$ duration per cycle of 60 s as a function of substrate temperature. (c) Thickness of TiO$_2$ (substrate temperature 200°C, O$_2$ duration 60 s) as a function of cycle number.

2.2 _____

Novel Pyrrole Based Precursors for ALD of BaTiO$_3$

As shown for PEALD of BaTiO$_3$, the reaction with the commercial precursor seems to be at the edge of ALD behavior and has some CVD component. This is reflected in the inferior step coverage of high AR substrates seen in Figure 4.19.

For this purpose, a novel pyrrole based precursor (py-Ba) was used to grow barium oxide (BaO) and BTO films by thermal ALD using TTIP as TiO$_2$ precursor and H$_2$O as a co-reactant. We achieved self-limiting growth of both BaO and BTO films at the lowest substrate temperature reported so far (195 °C). The growth rates are 0.3 Å/cycle (BaO) and 0.2 Å/cycle (BTO) allowing exact control of film thickness and composition. The as-deposited 7 nm thick films are partially crystallized by a post-deposition plasma treatment and show dielectric constants as high as 94 and leakage current densities below $1 \cdot 10^{-8}$ A/cm^2. ALD of BaO and BTO using the novel py-Ba precursor is promising for a variety of future high–k thin film applications.

In future work, the step coverage of this novel precursor needs to be tested to verify its ability for conformal coverage, that being a huge advantage over commercially available precursors.

Another peer-reviewed paper on this research was submitted:
Atomic Layer Deposition of Barium Oxide and High-k Barium Titanate Thin Films Using Novel Pyrrole Based Precursor, S. Acharya*, J. Torgersen*, S. Walch, Y. Kim, P. Schindler, S. Xu, T. Usui, C. Schildknecht and F. B. Prinz

122

Bibliography

[1] H. Iwai and H. Wong. Nano-CMOS technology for next fifteen years. In *IEEE Region 10 Annual International Conference, Proceedings/TENCON*, 2007.

[2] H. Wong and H. Iwai. On the scaling issues and high-k replacement of ultrathin gate dielectrics for nanoscale MOS transistors. *Microelectronic Engineering*, 83(10):1867–1904, 2006.

[3] B. Doering, P. Gargini, and I. Steff. International technology roadmap for semiconductors. Technical report, ITRS, 2011.

[4] B. Doering, P. Gargini, and J. Matisoo. International technology roadmap for semiconductors. Technical report, ITRS, 2001.

[5] P. Apte, B. Doering, and P. Gargini. International technology roadmap for semiconductors. Technical report, ITRS, 2005.

[6] T. Usui. *Exploring the limits of materials for energy and charge storage.* PhD Thesis, Stanford University, 2013.

[7] D. R. Lide, editor. *CRC Handbook of Chemistry and Physics, 89th Edition.* CRC Press, 89 edition, 2008.

[8] H. Shin, M. R. De Guire, and A. H. Heuer. Electrical properties of TiO_2 thin films formed on self-assembled organic monolayers on silicon. *Journal of Applied Physics*, 83(6), 1998.

[9] J. Yota, H. Shen, and R. Ramanathan. Characterization of atomic layer deposition HfO_2, Al_2O_3, and plasma-enhanced chemical vapor deposition Si_3N_4 as metal–insulator–metal capacitor dielectric for GaAs HBT technology. *Journal of Vacuum Science & Technology A: Vacuum, Surfaces, and Films*, 31(1):01A134, 2013.

[10] T. Usui, C. Donnelly, M. Logar, R. Sinclair, J. Schoonman, and F. B. Prinz. Approaching the limits of dielectric breakdown for SiO_2 films deposited by plasma-enhanced atomic layer deposition. *Acta Materialia*, 61(20):7660–7670, December 2013.

[11] V. Miikkulainen, M. Leskelä, M. Ritala, and R. L. Puurunen. Crystallinity of inorganic films grown by atomic layer deposition: Overview and general trends. *Journal of Applied Physics*, 113(2):021301, 2013.

[12] J.W. McPherson, J.-Y. Kim, A. Shanware, and H. Mogul. Thermochemical description of dielectric breakdown in high dielectric constant materials. *Applied Physics Letters*, 82(13):2121–2123, 2003.

[13] T. Tohma, H. Masumoto, and T. Goto. Microstructure and Dielectric Properties of Barium Titanate Film Prepared by MOCVD. *Materials Transactions*, 43(11):2880–2884, 2002.

[14] M. Vehkamäki, T. Hatanpää, M. Ritala, M. Leskelä, S. Väyrynen, and E. Rauhala. Atomic Layer Deposition of BaTiO$_3$ Thin Films – Effect of Barium Hydroxide Formation. *Chemical Vapor Deposition*, 13(5):239–246, May 2007.

[15] M. Vehkamäki and T. Hatanpää. Growth of SrTiO$_3$ and BaTiO$_3$ thin films by atomic layer deposition. *Electrochemical and Solid-State Letters*, 2(10):504–506, 1999.

[16] D. M. King, X. Du, A. S. Cavanagh, and A. W. Weimer. Quantum confinement in amorphous TiO$_2$ films studied via atomic layer deposition. *Nanotechnology*, 19(44):445401, November 2008.

[17] S. Wada, T. Hoshina, and H. Yasuno. Size dependence of dielectric properties for nm-sized barium titanate crystallites and its origin. *Journal of the Korean Physical Society*, 46(1):303–307, 2005.

[18] J. An, T. Usui, M. Logar, J. Park, D. Thian, S. Kim, K. Kim, and F. B. Prinz. Plasma Processing for Crystallization and Densification of Atomic Layer Deposition BaTiO$_3$ Thin Films. *ACS Applied Materials & Interfaces*, 6:10656–10660, 2014.

[19] Z. Wang, T. Yasuda, S. Hatatani, and S. Oda. Enhanced Dielectric Properties in SrTiO$_3$ / BaTiO$_3$ Strained Superlattice Structures Prepared by Atomic-Layer Metalorganic Chemical Vapor Deposition. *Japanese journal of applied physics*, 38(12):6817–6820, 1999.

[20] B. Chen, H. Yang, L. Zhao, J. Miao, B. Xu, X. G. Qiu, B. R. Zhao, X. Y. Qi, and X. F. Duan. Thickness and dielectric constant of dead layer in Pt/(Ba$_{0.7}$Sr$_{0.3}$)TiO$_3$/YBa$_2$Cu$_3$O$_{7-x}$ capacitor. *Applied Physics Letters*, 84(4):583, 2004.

[21] S. W. Lee, O. S. Kwon, J. H. Han, and C. S. Hwang. Enhanced electrical properties of SrTiO$_3$ thin films grown by atomic layer deposition at high temperature for dynamic random access memory applications. *Applied Physics Letters*, 92(22):21–24, 2008.

[22] S. W. Lee, J. H. Han, S. Han, W. Lee, J. H. Jang, M. Seo, S. K. Kim, C. Dussarrat, J. Gatineau, Y.-S. Min, and C. S. Hwang. Atomic Layer Deposition of SrTiO$_3$ Thin Films with Highly Enhanced Growth Rate for Ultrahigh Density Capacitors. *Chemistry of Materials*, 23:2227–2236, 2011.

[23] M. Popovici, S. Van Elshocht, N. Menou, P. Favia, H. Bender, E. Rosseel, J. Swerts, C. Adelmann, C. Vrancken, A. Moussa, H. Tielens, K. Tomida, M. Pawlak, B. Kaczer, G. Schoofs, W. Vandervorst, D. J. Wouters, and J. Kittl. Impact of thermal treatment upon morphology and crystallinity of strontium titanate films deposited by atomic layer deposition. *Journal of Vacuum Science & Technology B: Microelectronics and Nanometer Structures*, 29(1):01A304, 2011.

[24] S. Liu, B. Ma, M. Narayanan, S. Chao, R. Koritala, and U. Balachandran. Improved properties of barium strontium titanate thin films grown on copper foils by pulsed laser deposition using a self-buffered layer. *Journal of Physics D: Applied Physics*, 45(17):175304, 2012.

[25] N. Aslam, V. Longo, W. Keuning, F. Roozeboom, W. M. M. Kessels, R. Waser, and S. Hoffmann-Eifert. Influence of stoichiometry on the performance of MIM capacitors from plasma-assisted ALD Sr$_x$Ti$_y$O$_z$ films. *Physica Status Solidi (a)*, 211(2):389–396, February 2014.

[26] W. Lee, J. H. Han, W. Jeon, Y. W. Yoo, S. W. Lee, S. K. Kim, C. H. Ko, C. Lansalot-Matras, and C. S. Hwang. Atomic Layer Deposition of SrTiO$_3$ Films with Cyclopentadienyl-Based Precursors for Metal – Insulator – Metal Capacitors. *Chemistry of Materials*, 25(6):953–961, 2013.

[27] T. Usui, S. A. Mollinger, A. T. Iancu, R. M. Reis, and F. B. Prinz. High aspect ratio and high breakdown strength metal-oxide capacitors. *Applied Physics Letters*, 101(3):33905, 2012.

[28] J. Oh, T. Moon, T. Kim, C. Kim, J. H. Lee, S. Y. Lee, and B. Park. The dependence of dielectric properties on the thickness of $(Ba,Sr)TiO_3$ thin films. *Current Applied Physics*, 7(2):168–171, February 2007.

[29] M. Stengel and N. A. Spaldin. Origin of the dielectric dead layer in nanoscale capacitors. *Nature*, 443(7112):679–682, 2006.

[30] K. Natori, D. Otani, and N. Sano. Thickness dependence of the effective dielectric constant in a thin film capacitor. *Applied Physics Letters*, 73(5):632, 1998.

[31] R. Tsu and L. Esaki. Tunneling in a finite superlattice. *Applied Physics Letters*, 22(11):562–564, 1973.

[32] A. Gehring and S. Selberherr. Modeling of Tunneling Current and Gate Dielectric Reliability for Nonvolatile Memory Devices. *IEEE Transactions on Device and Materials Reliability*, 4(3):306–319, September 2004.

[33] B. Van Zeghbroeck. *Principles of Electronic Devices*. University of Colorado at Boulder, 2011.

[34] Y.-C. Yeo, T.-J. King, and C. Hu. Metal–dielectric band alignment and its implications for metal gate complementary metal–oxide–semiconductor technology. *Journal of Applied Physics*, 92(12):7266, 2002.

[35] M. L. Huang, Y. C. Chang, C. H. Chang, T. D. Lin, J. Kwo, T. B. Wu, and M. Hong. Energy-band parameters of atomic layer deposition Al_2O_3/InGaAs heterostructure. *Applied Physics Letters*, 89(1):012903, 2006.

[36] A. Bhardwaj. *The Composition Dependence of the Photochemical Reactivity of Strontium Barium Titanate*. ProQuest, 2009.

[37] C. N. Berglund and W. S. Baer. Electron transport in single-domain, ferroelectric barium titanate. *Physical Review*, 157(2):358–366, 1967.

[38] P. A. Tipler and R. A. Llewellyn. *Modern physics*. W. H. Freeman and Co., New York, 2012.

[39] W. J. Chang, M. P. Houng, and Y. H. Wang. Simulation of stress-induced leakage current in silicon dioxides: A modified trap-assisted tunneling model considering Gaussian-distributed traps and electron energy loss. *Journal of Applied Physics*, 89(11), 2001.

[40] M. Seo, S. Ho Rha, S. Keun Kim, J. Hwan Han, W. Lee, S. Han, and C. Seong Hwang. The mechanism for the suppression of leakage current in high dielectric TiO_2 thin films by adopting ultra-thin HfO_2 films for memory application. *Journal of Applied Physics*, 110(2):0–7, 2011.

[41] J. C. Shin, J. Park, C. S. Hwang, and H. J. Kim. Dielectric and electrical properties of sputter grown $(Ba,Sr)TiO_3$ thin films. *Journal of Applied Physics*, 86(1), 1999.

[42] F.-C. Chiu. Review Article A Review on Conduction Mechanisms in Dielectric Films. *Advances in Materials Science and Engineering*, page 18, 2014.

[43] D. J. DiMaria, E. Cartier, and D. Arnold. Impact ionization, trap creation, degradation, and breakdown in silicon dioxide films on silicon. *Journal of Applied Physics*, 73(7):3367, 1993.

[44] A. Gehring, T. Grasser, H. Kosina, and S. Selberherr. Simulation of hot-electron oxide tunneling current based on a non-Maxwellian electron energy distribution function. *Journal of Applied Physics*, 92(10):6019, 2002.

[45] S. M. George. Atomic layer deposition: An overview. *Chemical reviews*, 110(1):111–31, January 2010.

[46] R. L. Puurunen. Surface chemistry of atomic layer deposition: A case study for the trimethylaluminum/water process. *Journal of Applied Physics*, 97(12):1–52, 2005.

[47] S. E. Potts and W. M. M. Kessels. Energy-enhanced atomic layer deposition for more process and precursor versatility. *Coordination Chemistry Reviews*, 257(23-24):3254–3270, December 2013.

[48] T. Nam, J.-M. Kim, M.-K. Kim, H. Kim, and W.-H. Kim. Low-temperature Atomic Layer Deposition of TiO_2, Al_2O_3, and ZnO Thin Films. *Journal of the Korean Physical Society*, 59(21):452, August 2011.

[49] P. Banerjee, I. Perez, L. Henn-Lecordier, S. B. Lee, and G. W. Rubloff. Nanotubular metal–insulator–metal capacitor arrays for energy storage. *Nature nanotechnology*, 4(5):292–6, May 2009.

[50] U. Cvelbar, M. Mozetic, and A. Ricard. Characterization of oxygen plasma with a fiber optic catalytic probe and determination of recombination coefficients. *IEEE Transactions on Plasma Science*, 33(2):834–837, 2005.

[51] J. T. Gudmundsson. Recombination and detachment in oxygen discharges: the role of metastable oxygen molecules. *Journal of Physics D: Applied Physics*, 37(15):2073–2081, August 2004.

[52] M. Kariniemi, J. Niinistoö, M. Vehkamäki, M. Kemell, M. Ritala, M. Leskelä, and M. Putkonen. Conformality of remote plasma-enhanced atomic layer deposition processes: An experimental study. *Journal of Vacuum Science & Technology A: Vacuum, Surfaces, and Films*, 30(1):01A115, 2012.

[53] J. Dendooven, D. Deduytsche, J. Musschoot, R. L. Vanmeirhaeghe, and C. Detavernier. Conformality of Al_2O_3 and AlN Deposited by Plasma-Enhanced Atomic Layer Deposition. *Journal of The Electrochemical Society*, 157(4):G111, 2010.

[54] H. C. M. Knoops, E. Langereis, M. C. M. van de Sanden, and W. M. M. Kessels. Conformality of Plasma-Assisted ALD: Physical Processes and Modeling. *Journal of The Electrochemical Society*, 157(12):G241, 2010.

[55] R. Capan, N. B. Chaure, A. K. Hassan, and A. K. Ray. Optical dispersion in spun nanocrystalline titania thin films. *Semiconductor Science and Technology*, 19:198–202, 2004.

[56] M. G. Helander, M. T. Greiner, Z. B. Wang, and Z. H. Lu. Pitfalls in measuring work function using photoelectron spectroscopy. *Applied Surface Science*, 256(8):2602–2605, February 2010.

[57] F. Wooten and R. N. Stuart. Fowler's Hypothesis and the Determination of Photoemission Thresholds. *Physical Review*, 186(2):592–593, October 1969.

[58] P. Schindler. Quantum confined structures for high efficiency solar cells studied by transmission electron microscopy. Diploma thesis, University of Vienna, Vienna, 2011.

[59] M. von Heimendahl. *Einführung in die Elektronenmikroskopie.* Vieweg Friedr. + Sohn Ver, 12 1984.

[60] M. D. Graef. *Introduction to Conventional Transmission Electron Microscopy.* Cambridge University Press, 4 2003.

[61] B. Fultz and J. M. Howe. *Transmission Electron Microscopy and Diffractometry of Materials.* Springer, 3rd edition, 10 2007.

[62] D. B. Williams and C. B. Carter. *Transmission Electron Microscopy: A Textbook for Materials Science.* Springer, 2nd edition, 8 2009.

[63] L. Reimer and H. Kohl. *Transmission Electron Microscopy: Physics of Image Formation.* Springer, 5th edition, 11 2010.

[64] M. J. Kim and R. W. Carpenter. TEM specimen heating during ion beam thinning: Microstructural instability. *Ultramicroscopy*, 21(4):327–334, 1987.

[65] D. J. Barber. Radiation damage in ion-milled specimens: Characteristics, effects and methods of damage limitation. *Ultramicroscopy*, 52(1):101–125, 1993.

[66] T. Schuhrke, M. Mandl, J. Zweck, and H. Hoffmann. Investigation of surface amorphization of silicon wafers during ion-milling. *Ultramicroscopy*, 41(4):429–433, 1992.

[67] A. I. Kingon, J. P. Maria, and S. K. Streiffer. Alternative dielectrics to silicon dioxide for memory and logic devices. *Nature*, 406(August):1032–1038, 2000.

[68] E. Gerritsen, N. Emonet, C. Caillat, N. Jourdan, M. Piazza, D. Fraboulet, B. Boeck, A. Berthelot, S. Smith, and P. Mazoyer. Evolution of materials technology for stacked-capacitors in 65 nm embedded-DRAM. *Solid-State Electronics*, 49(11):1767–1775, November 2005.

[69] C. S. Hwang. $(Ba, Sr)TiO_3$ thin films for ultra large scale dynamic random access memory: A review on the process integration. *Materials Science and Engineering: B*, 56:178–190, 1998.

[70] S. K. Kim, S. W. Lee, J. H. Han, B. Lee, S. Han, and C. S. Hwang. Capacitors with an Equivalent Oxide Thickness of < 0.5 nm for Nanoscale Electronic Semiconductor Memory. *Advanced Functional Materials*, 20(18):2989–3003, September 2010.

[71] M. Popovici, M.-S. Kim, K. Tomida, J. Swerts, H. Tielens, A. Moussa, O. Richard, H. Bender, A. Franquet, T. Conard, L. Altimime, S. Van Elshocht, and J. A. Kittl. Improved EOT and leakage current for metal–insulator–metal capacitor stacks with rutile TiO_2. *Microelectronic Engineering*, 88(7):1517–1520, July 2011.

[72] S. K. Kim, G. J. Choi, S. Y. Lee, M. Seo, S. W. Lee, J. H. Han, H. S. Ahn, S. Han, and C. S. Hwang. Al-doped TiO_2 films with ultralow leakage currents for next generation DRAM capacitors. *Advanced Materials*, 20(8):1429–1435, 2008.

[73] M. Grätzel. Conversion of sunlight to electric power by nanocrystalline dye-sensitized solar cells. *Journal of Photochemistry and Photobiology A: Chemistry*, 164(1-3):3–14, June 2004.

[74] A. Rothschild, F. Edelman, Y. Komem, and F. Cosandey. Sensing behavior of TiO_2 thin films exposed to air at low temperatures. *Sensors and Actuators B: Chemical*, 67(3):282–289, September 2000.

127

[75] H.-F. Yu and F.-C. Hu. Preparation and characterization of transparent TiO_2 thin films coated on fused-silica substrates. *Journal of Sol-Gel Science and Technology*, 52(1):158–165, June 2009.

[76] K. M. Glassford and J. R. Chelikowsky. Structural and electronic properties of titanium dioxide. *Phys. Rev. B*, 46(3):1284–1298, July 1992.

[77] J. Y. Kim, H. S. Jung, J. H. No, J.-R. Kim, and K. S. Hong. Influence of anatase-rutile phase transformation on dielectric properties of sol-gel derived TiO_2 thin films. *Journal of Electroceramics*, 16(4):447–451, July 2006.

[78] M. Landmann, E. Rauls, and W. G. Schmidt. The electronic structure and optical response of rutile, anatase and brookite TiO_2. *Journal of Physics: Condensed Matter*, 24(19):195503, May 2012.

[79] W. Hu, L. Li, G. Li, C. Tang, and L. Sun. High-quality brookite TiO_2 flowers: Synthesis, characterization, and dielectric performance. *Crystal Growth and Design*, 9(8):3676–3682, 2009.

[80] S. D. Mo and W. Y. Ching. Electronic and optical properties of three phases of titanium dioxide: rutile, anatase, and brookite. *Physical Review B*, 51(19):23–32, 1995.

[81] D. M. King, X. Liang, and A. W. Weimer. Functionalization of fine particles using atomic and molecular layer deposition. *Powder Technology*, 221:13–25, May 2012.

[82] C.-M. Wang, D.-L. Kong, Q. Chen, and J.-M. Xue. Surface engineering of synthetic nanopores by atomic layer deposition and their applications. *Frontiers of Materials Science*, 7(4):335–349, October 2013.

[83] A. Strecker, U. Salzberger, and J. Mayer. Specimen preparation for transmission electron microscopy: reliable method for cross-sections and brittle materials. *Praktische Metallographie/Practical Metallography*, 30(10):482–495, 1993.

[84] F. Gao, S. Arpiainen, and R. L. Puurunen. Microscopic silicon-based lateral high-aspect-ratio structures for thin film conformality analysis. *Journal of Vacuum Science & Technology A: Vacuum, Surfaces, and Films*, 33(1):010601, 2015.

[85] R. G. Gordon, D. Hausmann, E. Kim, and J. Shepard. A Kinetic Model for Step Coverage by Atomic Layer Deposition in Narrow Holes or Trenches. *Chemical Vapor Deposition*, 9(2):73–78, March 2003.

[86] H. G. Francois-Saint-Cyr, F. A. Stevie, J. M. McKinley, K. Elshot, L. Chow, and K. A. Richardson. Diffusion of 18 elements implanted into thermally grown SiO_2. *Journal of Applied Physics*, 94(12):7433, 2003.

[87] G. Cartry, L. Magne, and G. Cernogora. Atomic oxygen recombination on fused silica: experimental evidence of the surface state influence. *Journal of Physics D: Applied Physics*, 32:53–56, 1999.

[88] Y. C. Kim and M. Boudart. Recombination of O, N, and H Atoms on Silica: Kinetics and Mechanism. *Langmuir*, 7(12):2999–3005, 1991.

[89] S. B. S. Heil, J. L. van Hemmen, M. C. M. van de Sanden, and W. M. M. Kessels. Reaction mechanisms during plasma-assisted atomic layer deposition of metal oxides: A case study for Al_2O_2. *Journal of Applied Physics*, 103(10):103302, 2008.

[90] Q. Xie, J. Musschoot, D. Deduytsche, R. L. Van Meirhaeghe, C. Detavernier, S. Van den Berghe, Y.-L. Jiang, G.-P. Ru, B.-Z. Li, and X.-P. Qu. Growth Kinetics and Crystallization Behavior of TiO_2 Films Prepared by Plasma Enhanced Atomic Layer Deposition. *Journal of The Electrochemical Society*, 155(9):H688–H692, 2008.

[91] J. C. Greaves and J. W. Linnett. Recombination of atoms at surfaces. Part 6: Recombination of oxygen atoms on silica from 20 °C to 600 °C. *Transactions of the Faraday Society*, 55(0):1355–1361, 1959.

[92] M. Reiners, K. Xu, N. Aslam, A. Devi, R. Waser, and S. Hoffmann-Eifert. Growth and Crystallization of TiO_2 Thin Films by Atomic Layer Deposition Using a Novel Amido Guanidinate Titanium Source and Tetrakis-dimethylamido-titanium. *Chemistry of Materials*, 25(15):2934–2943, 2013.

[93] A. Niskanen, K. Arstila, M. Leskelä, and M. Ritala. Radical Enhanced Atomic Layer Deposition of Titanium Dioxide. *Chemical Vapor Deposition*, 13(4):152–157, April 2007.

[94] J. Kim, S. Kim, H. Jeon, M.-H. Cho, K.-B. Chung, and C. Bae. Characteristics of HfO_2 thin films grown by plasma atomic layer deposition. *Applied Physics Letters*, 87(5):053108, 2005.

[95] N. Kosku, H. Murakami, S. Higashi, and S. Miyazaki. Influence of substrate dc bias on crystallinity of silicon films grown at a high rate from inductively-coupled plasma CVD. *Applied Surface Science*, 244(1-4):39–42, 2005.

[96] V. R. Rai and S. Agarwal. Surface Reaction Mechanisms during Plasma-Assisted Atomic Layer Deposition of Titanium Dioxide. *The Journal of Physical Chemistry C*, 113(30):12962–12965, 2009.

[97] N. Martin, C. Rousselot, D. Rondot, F. Palmino, and R. Mercier. Microstructure modification of amorphous titanium oxide thin films during annealing treatment. *Thin Solid Films*, 300(1-2):113–121, 1997.

[98] J. W. Lim, S. J. Yun, and J. H. Lee. Characteristics of TiO_2 Films Prepared by ALD With and Without Plasma. *Electrochemical and Solid-State Letters*, 7(11):F73, 2004.

[99] R. Schafranek, A. Giere, A. G. Balogh, T. Enz, Y. Zheng, P. Scheele, R. Jakoby, and A. Klein. Influence of sputter deposition parameters on the properties of tunable barium strontium titanate thin films for microwave applications. *Journal of the European Ceramic Society*, 29(8):1433–1442, 2009.

[100] H. B. Profijt, S. E. Potts, M. C. M. van de Sanden, and W. M. M. Kessels. Plasma-Assisted Atomic Layer Deposition: Basics, Opportunities, and Challenges. *Journal of Vacuum Science & Technology A: Vacuum, Surfaces, and Films*, 29(5):050801, 2011.

[101] J. A. Dean. *Lange's handbook of chemistry.* McGraw-Hill, New York,N.Y., 1999.

[102] J. J. Wang, F. Y. Meng, X. Q. Ma, M. X. Xu, and L. Q. Chen. Lattice, elastic, polarization, and electrostrictive properties of $BaTiO_3$ from first-principles. *Journal of Applied Physics*, 108(3), 2010.

[103] T. Takagi. Ion-surface interactions during thin film deposition. *Journal of Vacuum Science & Technology A: Vacuum, Surfaces, and Films*, 2(2):382, 1984.

[104] J. C. Olson, D. F. Stevison, and I. Bransky. The effect of temperature on properties of RF Sputtered $BaTiO_3$ films. *Ferroelectrics*, 37(1):685–686, October 1981.

[105] N. Okui. Relationship between crystallization temperature and melting temperature in crystalline materials. *Journal of Materials Science*, 25(3):1623–1631, 1990.

[106] R. R. Reddy, Y. Nazeer Ahammed, K. Rama Gopal, and D. V. Raghuram. Optical electronegativity and refractive index of materials. *Optical Materials*, 10(2):95–100, 1998.

[107] R. Hovhannisyan, H. Alexanyan, M. Hovhannisyan, B. Petrosyan, and V. Harutyuny. Phase Diagramm, Cristallization Behavior and Ferroelectric Properties of Stoichiometric Glass Ceramics in the BaO–TiO$_2$–B$_2$O$_3$ System. In Mickal Lallart, editor, *Ferroelectrics - Physical Effects*, chapter 3. InTech, May 2011.

[108] H. B. Profijt, S. E. Potts, M. C. M. van de Sanden, and W. M. M. Kessels. Plasma-Assisted Atomic Layer Deposition: Basics, Opportunities, and Challenges. *Journal of Vacuum Science & Technology A: Vacuum, Surfaces, and Films*, 29(5):050801, 2011.

[109] J. L. Keddie, J. Li, J. W. Mayer, and E. P. Giannelis. Effect of Nitridation Rate on the Composition and Conductivity of Titanium Nitride Films Prepared from Sol-Gel Titania. *Journal of the American Ceramic Society*, 74(11):2937–2940, 1991.

[110] L. P. B. Lima, J. A. Diniz, I. Doi, and J. Godoy Fo. Titanium nitride as electrode for MOS technology and Schottky diode: Alternative extraction method of titanium nitride work function. *Microelectronic Engineering*, 92:86–90, April 2012.

[111] Y. Liu, S. Kijima, E. Sugimata, M. Masahara, K. Endo, T. Matsukawa, K. Ishii, K. Sakamoto, T. Sekigawa, H. Yamauchi, Y. Takanashi, and E. Suzuki. Investigation of the TiN Gate Electrode With Tunable Work Function and Its Application for FinFET Fabrication. *IEEE Transactions On Nanotechnology*, 5(6):723–730, November 2006.

[112] G. S. Lujan and T. Schram. Impact of ALCVD and PVD titanium nitride deposition on metal gate capacitors. *Proceedings ESSDERC 2002*, pages 583–586, 2002.

[113] J. S. Chawla, X. Y. Zhang, and D. Gall. Effective electron mean free path in TiN(001). *Journal of Applied Physics*, 113(6):063704, 2013.

[114] S. Sayan, R. A. Bartynski, X. Zhao, E. P. Gusev, D. Vanderbilt, M. Croft, M. Banaszak Holl, and E. Garfunkel. Valence and conduction band offsets of a ZrO$_2$/SiO$_x$N$_y$/n-Si CMOS gate stack: A combined photoemission and inverse photoemission study. *Physica Status Solidi (B)*, 241(10):2246–2252, August 2004.

[115] G. Lucovsky and B. Rayner. Experimental determination of band offset energies between Zr silicate alloy dielectrics and crystalline Si substrates by XAS, XPS and AES and ab initio theory: A new approach to the compositional dependence of direct tunneling currents . In *IEDM 2002*, pages 617–620, 2002.

[116] W. Heywang. Resistivity Anomaly in Doped Barium Titanate. *Journal of the American Ceramic Society*, 47(10):484–490, 1964.

[117] Y. W. Yoo, W. Jeon, W. Lee, C. H. An, S. K. Kim, and C. S. Hwang. Structure and Electrical Properties of Al-Doped HfO$_2$ and ZrO$_2$ Films Grown via Atomic Layer Deposition on Mo Electrodes. *ACS Applied Materials & Interfaces*, 6(24):22474–22482, December 2014.

[118] R. A. Perez, H. Nakajima, and F. Dyment. Diffusion in a-Ti and Zr. *Materials Transactions*, 44(1):2–13, 2003.

[119] M. D. Groner, F. H. Fabreguette, J. W. Elam, and S. M. George. Low-Temperature Al$_2$O$_3$ Atomic Layer Deposition. *Chemistry of Materials*, 16(4):639–645, 2004.

Curriculum Vitae | Peter Schindler

Personal Information

Full name	Peter Schindler
Email	peter.schindler@stanford.edu
	peter.schindler@pschindler.net
Nationality	Austrian
Academic degree	Magister rerum naturalium (equivalent M.Sc.)

Education

07.2012 - present
Graduate studies in Physics (Dr. rer. nat./Ph.D.)
University of Vienna, in collaboration with Stanford University
Thesis topic: "Next generation high-k dielectrics for DRAM produced by atomic layer deposition studied by transmission electron microscopy"

10.2005 - 08.2011
Under/graduate studies in Physics (Mag. rer. nat./M.Sc.)
University of Vienna, Graduation with distinction
Thesis topic: "Quantum confined structures for high efficiency solar cells studied by transmission electron microscopy"

01.2010 - 07.2010
Exchange student (Erasmus program)
University of Swansea, UK

06.2005
High school graduation (Maturity examination)
GRG 3 Hagenmüllergasse, Vienna, Austria
Grade average 1.5 (equivalent GPA 3.5)

Research Experience

11.2012 - 04.2015
Research scholar at "Nano-Prototyping Lab (NPL)"
Stanford University, Department of Mechanical Engineering

07.2012 - 11.2012
Research student at "Materials Center Leoben (MCL)"
Austrian Competence Center for Excellent Technologies (COMET)

06.2009 - 09.2011
Diploma student at "Physics of Nanostructured Materials"
University of Vienna, Faculty of Physics

Conferences and Workshops

Poster presentation	18. International Microscopy Congress, 09.2014, Prague, Czech Republic
Oral presentation	Multinational Conference on Microscopy, 09.2011, Urbino, Italy
Oral presentation	First ASEM Workshop, 04.2011, Graz, Austria
Oral presentation	DPG Frühjahrstagung, 03.2011, Dresden, Germany
Poster presentation	Erwin Schödinger Symposium, 01.2011, Vienna, Austria
Poster presentation	ESTEEM Workshop for HAADF and EELS, 10.2009, Piran, Slovenia
Poster presentation	Microscopy Conference 2009, 08.2009, Graz, Austria

Conference Proceedings

ALD 2015, Portland, USA	"In-situ Observation of Ruthenium Growth Via a Combined Scanning Tunneling Microscope and Atomic Layer Deposition System", D. Thian, Y. Yemane, I. Petousis, **P. Schindler** and F.B. Prinz
ALD 2015, Portland, USA	"Molecular Oxygen Reactions with Tetrakisdimethylamido-metal Precursors for Atomic Layer Deposition", J. Provine, **P. Schindler** and F.B. Prinz
ALD 2015, Portland, USA	"Effect of Film Density on Wet Etch Rate in Low Temperature Plasma-enhanced Atomic Layer Deposited Silicon Nitride", J Provine, **P. Schindler** and Y. Kim
ALD 2015, Portland, USA	"High Quality ALD of Silicon Nitride Films via Microwave Plasma", K. Kim, J Provine, **P. Schindler**, S. Walch, Y. Kim and H. Kim
IMC 2014, Prague, CZ	"TEM Studies of High Aspect Ratio Surfaces Coated with Thin Dielectric Films by Atomic Layer Deposition", **P. Schindler**, M. Logar, T. Usui, J Provine, H. P. Karnthaler and F. B. Prinz
IMC 2014, Prague, CZ	"Nanostructured Shape Memory Alloys: Phase Transformations and Martensitic Interfaces Studied by TEM", T. Waitz, M. Peterlechner, C. Gammer, K. Tsuchiya, M. Chakif, C. Mangler and **P. Schindler**
MRS 2013, San Francisco, USA	"Ultrafine Grained Shape Memory Alloys: Martensitic Phase Transformations, Reversibility, Hysteresis", T. Waitz, C. Mangler, **P. Schindler**, E. Schafler, P. Müllner, V. Srivastava and R. D. James
MCM 2011, Urbino, IT	"TEM Studies of PbS Quantum Dots for High Efficiency Solar Cells", **P. Schindler**, N. P. Dasgupta, O. Trejo, C. Rentenberger, T. Waitz, F. B. Prinz and H. P. Karnthaler
DPG 2011, Dresden, GER	"TEM Studies of PbS-ZnS/ZnO Quantum Confinement Structures for Solar Cells", **P. Schindler**, N. P. Dasgupta, O. Trejo, C. Rentenberger, T. Waitz, F. B. Prinz and H. P. Karnthaler
MC 2009, Graz, AUT dx.doi.org/10.3217/978-3-85125-062-6-607	"TEM Studies of PbS-ZnS Quantum Wells for Solar Cells", **P. Schindler**, N. P. Dasgupta, C. Rentenberger, T. Waitz, F. B. Prinz and H. P. Karnthaler

Peer-Reviewed Publications

ACS Langmuir, 2015, 31 (18) pp 5057–5062 DOI: 10.1021/acs.langmuir.5b00216	"Enhanced Step Coverage of TiO_2 Deposited on High Aspect Ratio Surfaces by Plasma-Enhanced Atomic Layer Deposition", **P. Schindler**, M. Logar, J Provine and F. B. Prinz
J. Phys. Chem. C, 2014, 118 (43) pp 24827–24832 DOI: 10.1021/jp5073044	"Energy States of Ligand Capped Ag Nanoparticles: Relating Surface Plasmon Resonance to Work Function", A. L. Dadlani, **P. Schindler**, M. Logar, S. P. Walch, and F. B. Prinz
Acta Mater., submitted	"Plasma-Enhanced Atomic Layer Deposition of $BaTiO_3$", **P. Schindler***, Y. Kim*, D. Thian, J. An and F. B. Prinz
Small, submitted	"Deposition of Large Scale Quantum Dot Monolayer by Langmuir-Blodgett Ttechnique with Dilatational Rheology", S. Xu, A. L. Dadlani, S. Acharya, **P. Schindler** and F. B. Prinz
Chem. Mater., submitted	"Atomic Layer Deposition of Barium Oxide and high-k Barium Titanate Thin Films using Novel Pyrrole Based Precursor", S. Acharya*, J. Torgersen*, S. Walch, Y. Kim, **P. Schindler**, S. Xu, T. Usui, C. Schildknecht and F. B. Prinz
In preparation	"Plasma-Enhanced Atomic Layer Deposition of Al-Doped Barium Titanate", Y. Kim*, **P. Schindler***, S. Acharya, A. L. Dadlani, J Provine, J. An and F. B. Prinz
In preparation	"Molecular Oxygen Reactions with Tetrakisdimethylamido-metal Precursors for Atomic Layer Deposition", **P. Schindler,** J Provine, J. Torgersen, K. Kim, H. P. Karnthaler and F. B. Prinz

*contributed equally

(Provisional) Patents

05.2015, S15-195
Stanford University/
Samsung Electronics

"Optimal Composite Thin Films of Silicon Nitride and Aluminum Nitride for Low Wet Etch Rate in Hydrofluoric Acid and Low Leakage Current", F. B. Prinz, J Provine, Y. Kim, **P. Schindler**, H. Kim, S. Walch

08.2014, S14-191
Stanford University/
Samsung Electronics

"Control of Electronic Properties Including Work Function in Atomic Layer Deposited Tthin Films Containing Multiple Metal-Nitrides", F. B. Prinz, J Provine, **P. Schindler**, J. An, Y. Kim

02.2013, S13-280
Stanford University/
Samsung Electronics

"Extreme Ultraviolet Radiation (EUV) Assisted Atomic Layer Deposition", M. C. Langston, F. B. Prinz, **P. Schindler**, T. Usui, K. Kim, S. Kim, S. P. Walch, A. T. Iancu

02.2013, S13-143
Stanford University/
Samsung Electronics

"Crystallization of Metal Oxides by Plasma Exposure During Atomic Layer Deposition", F. B. Prinz, **P. Schindler**, T. Usui, J Provine, C. Donnelly, M. Logar, K. Kim, S. Kim

Language Skills

German	Fluent (Native)
English	Fluent
Spanish	Basic

Personal Interests

Arts/Creative	Photography, Web design
Music/Dancing	Drums, Salsa, Bachata
Sports	Basketball, Badmington